A parametric study in the force production of surging and pitching wings using a deconvolution Kalman filtering approach

R. Vester

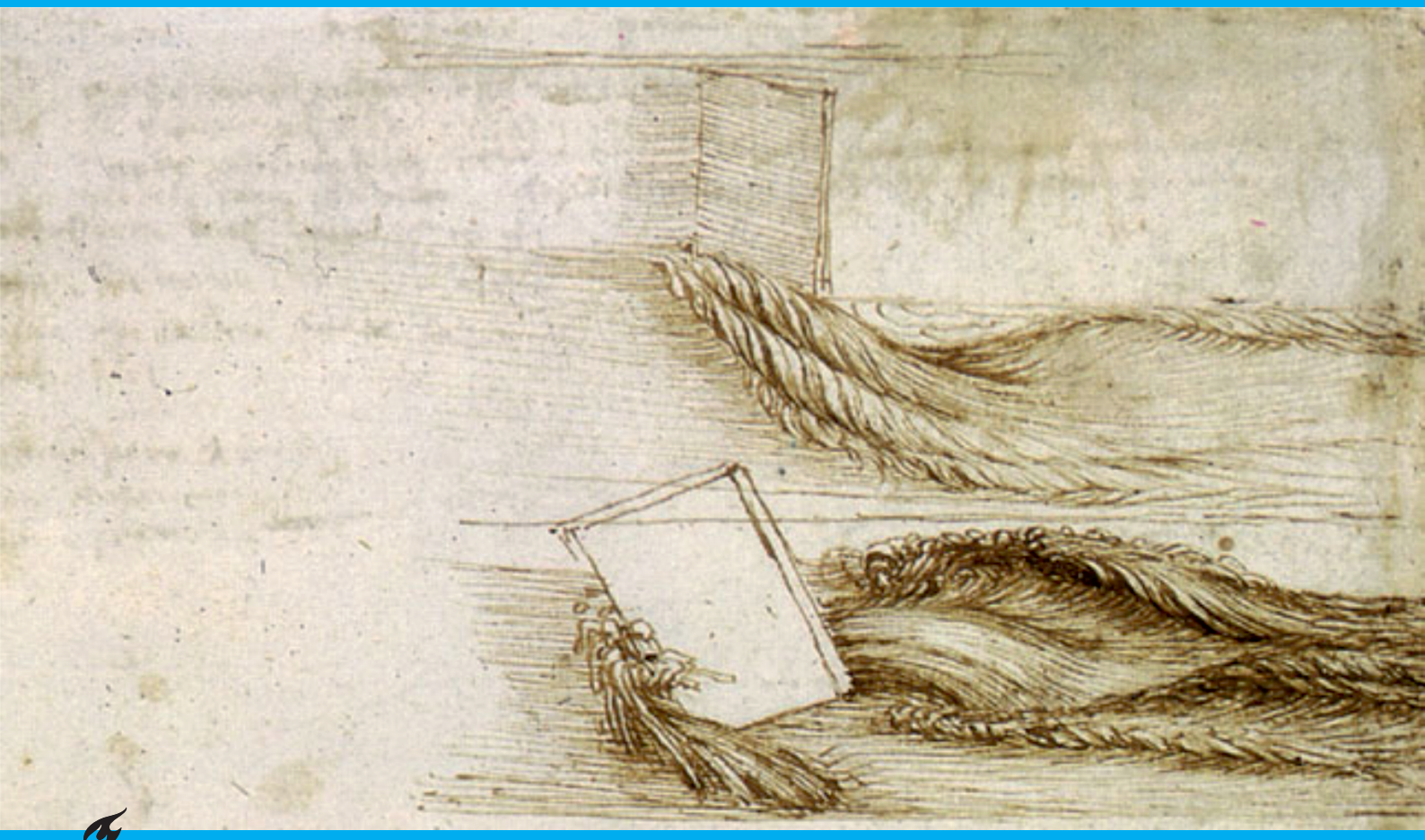

TU Delft

A parametric study in the force production of surging and pitching wings using a deconvolution Kalman filtering approach

by

R. Vester

to obtain the degree of Master of Science
at the Delft University of Technology,
to be defended publicly on Wednesday the 30th of August, 2017 at 09:30.

Student number: 1357301
Thesis committee: Bas v. Oudheusden, TU Delft, supervisor
Ir. C. de Wagter, TU Delft
Dr.ir. F.F.J. Schrijer, TU Delft

TU Delft

Preface

Flapping wing flight is a fascinating research subject, and in this report, a tiny part of this rather large field is investigated further. The author hopes that this will serve to advance the field by a tiny tiny fraction. This thesis has been a long time coming, and I would like to express my thanks to Bas van Oudheusden and Mustafa Perçin, for sticking with me all the time. I would doubly thank them as well for allowing me to publish my results. Special thanks go out to Richard Ahlfeld, who has helped me tremendously to overcome one of the more difficult issues. I'm also indebted to the graduation committee.

Furthermore, to my father and mother, my brother and my sisters, my amazing girlfriend, my jaarclub, and all others who have supported me during the at-times difficult process: I truly could not have done it without you.

R. Vester
Delft, August 2017

Summary

Mechanized flapping wing flight has the potential to be used on a large scale in the future, due to the relatively high flight efficiency at small sizes compared to rotary- and rigid wing flight. The potential of flapping-wing flight is demonstrated by insects and small birds, which use unsteady aerodynamic effects to create larger pressure differences between the top and bottom of the wing than is possible with steady aerodynamics as used by conventional aircraft. Currently, mechanical demonstrator flapping-wing flyers such as the DelFly range show promise and have garnered the interest of the public. But, to date no flapping wing flyer is under production that suits the needs of the market. To effectively use these unsteady aerodynamic effects, the wing motion and wing size need to be chosen with care. After millions of years of evolutionary optimization, flapping wing biological flyers are highly adapted to this form of flying. Therefore, how insects use these unsteady aerodynamics effects is under great scientific attention, with robotic flapping-wing apparatuses replicating insect wing motion to discover the links between wing motion, force production, and resulting flow structures. These robotic flappers are equipped with precise actuators to control wing motion and force sensors to measure the force on the wing. Sometimes, advanced flow measurement techniques are used to investigate the flow structures resulting from the flapping motion. Robotic flapping-wing measurement apparatuses have conflicting design parameters, as the size of the structure needs to be minimized to better simulate a real wing, but the structure needs to be stiff to not vibrate due to the forces on the wing during the experiment, which can obscure the force measurement. In the current state-of-the-art of such force measurements the temporal resolution is limited due to the need of severe digital filters to suppress the noise because of the vibration of the mechanical structure.

This report consists of a three-part investigation regarding such force measurements. One part is a parametric experimental investigation in the force production of revolving, or sweeping, wings accelerating from rest at a fixed angle of attack. In this investigation, the angle of attack is the varying parameter. Another part is a similar experimental investigation, but the wing is now revolving at constant velocity, and then rotates, or pitches, along the spanwise axis. The chordwise location of this spanwise axis and the rotational velocity are the varying parameters in these experiments. The final part of this report is an investigation on the use of the Deconvolution Kalman filter for the force measurements, where the aim is to be less dependent on the stiffness of the measurement structure, but instead to take the mechanical properties of the measurement structure into account when estimating the forces on the wing from the data obtained from the sensor. The measurements performed are used to assess the validity of the results obtained in this way.

The shortcomings of the current state-of-the-art in filtering are demonstrated, where it is shown with synthetic tests that conventional filtering setups are likely to introduce large errors, both in magnitude and in timing of the force production for the experiments under consideration, for the phases of the motions where the time rate of change of the force production is large. It is found that the Deconvolution Kalman filter is straightforward to set up for a synthetic experiment. For the measurement setup under consideration, obtaining a good mathematical representation of the mechanical behaviour of the measurement setup proved to be difficult. A satisfactory result is obtained, and the nature of the filter seems to be forgiving to minor errors in this process. The force measurements themselves show interesting results where the expected linear relation between force production and rotational velocity does not seem to hold true. The measurements also show small but meaningful differences in terms of normal force and center of pressure location, for experiments with different kinematics, but the same instantaneous motion parameters. Further interesting results are found where the center of pressure location is plotted over time, which reveals large differences over time, and between the two different types of motion under consideration. In general, the wing root seems to produce relatively less force than would be expected from a blade-element estimation.

Contents

List of Symbols

Abbreviations

AR	Wing aspect ratio
COP	Center of Pressure
DC	Direct Current
DK	Deconvolution Kalman
PEM	Prediction Error Minimization
PSD	Power Spectral Density
SD	Standard deviation
SNR	Signal to Noise Ratio

Symbols

α	Wing pitch or angle of attack
$\dot{\alpha}$	Wing pitch angular velocity
$\ddot{\alpha}$	Wing pitch angular acceleration
$\dot{\phi}$	Wing revolving angular velocity
$\ddot{\phi}$	Revolving angular acceleration
b	Wing span
c	Wing chord
c_M	Pitching moment coefficient
c_N	Normal force coefficient
c_T	Tangential force coefficient
k	Reduced pitch rate
Q	Process noise covariance matrix
R	Measurement noise covariance matrix
Re	Reynolds number
Ro	Rossby number
r	Radial position
S	Wing surface area
t^*	Convective time
x_0	Pitch axis in mm from leading edge
$\hat{x}_0$	Pitch axis in fractions of chord from leading edge

1

Introduction

For a long period in human history, moving wings were considered to be the only feasible mechanism for heavier-than-air propulsive flight. It took until the 19th century to change this. Only when George Cayley inscribed his silver coin with the basics of fixed-wing flight, the aeronautic society transformed from tinkers to scientists. With the advent of fixed-wing gliders and aircraft, fixed-wing flight has been the main scientific focus, with rotary-wing flight following suit in the 20th century. But flapping-wing flight has always been subject to human curiosity.

Recently, the advent of Micro Aerial Vehicles (MAV's) and successful demonstrators such as the DelFly, have rekindled scientific interest in flapping flight. In general, MAV's are small, remote controlled flyers that need to be able to fly and maneuver in populated areas. The flight goals usually include hovering and low-speed flight. This leads to the need to decouple lift from airspeed. The result is a current marketplace that is filled with rotary-wing MAV's. Rotary-wing flight is well-understood and with current electronic control capabilities can be cost-effective. However, rotary- and fixed wings operate in the steady-flow regime, as the flow over the wing is constant in time. In Figure 1.1, it is shown that the maximum lift coefficient attainable in steady-flow drops off steeply for lower Reynolds numbers, which is a measure of length- and speed scales in which a flyer operates. For example, a very small flyer with slow moving wings, such as a fruit fly, operates at a Reynolds number of around 1×10^2, and a Reynolds number of 1×10^7 is the Reynolds number of the wing of a passenger jet. Insects operate in the Reynolds number range from 1×10^2 to 1×10^4. In Figure 1.1, it is shown that there is a drop in maximum attainable steady-state lift below a Reynolds number of 1×10^5. To compensate, insects and other small biological flyers usually operate in the unsteady flow regime, in which the flow over the wing is not constant in time. This allows the biological flyer to use short-lived aerodynamic effects to increase the attained lift. A schematic, illustrative comparison between steady and unsteady aerodynamics is shown in Figure 1.2.

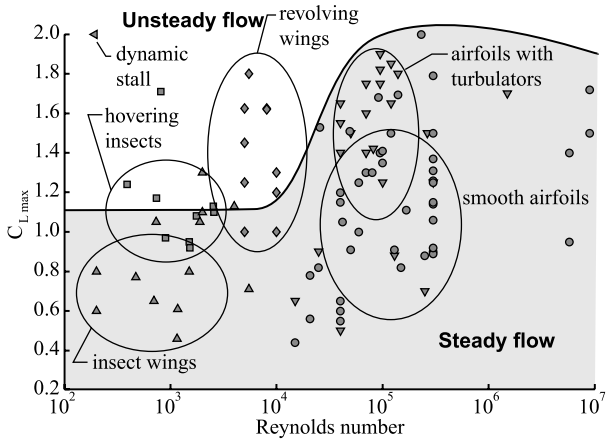

Figure 1.1: Maximum lift coefficient vs. Reynolds number, from [29]

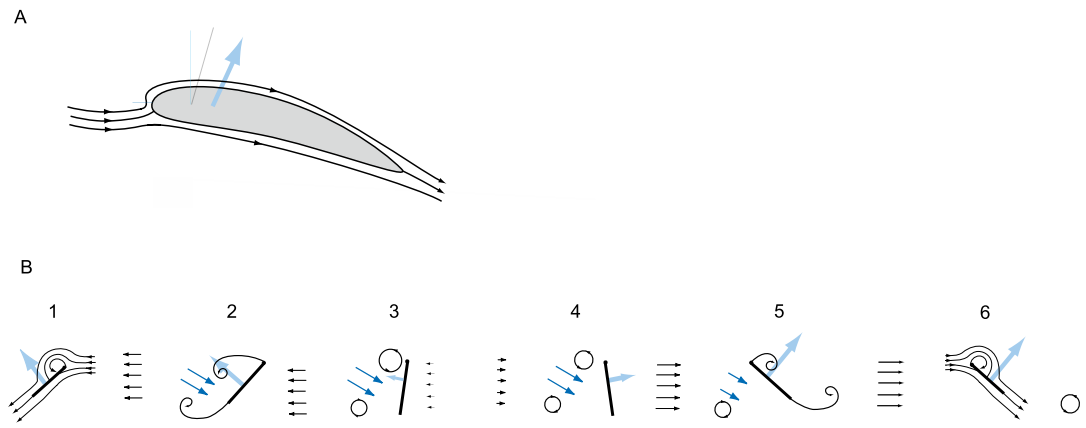

Figure 1.2: Schematic comparison of (A) an airfoil in steady aerodynamic conditions and (B) the unsteady stroke reversal phase of flapping wing motion (B), adapted from [56]

A logical first step in creating successful flapping wing MAV's is to learn as much as possible from the wings and wing movement of natural flyers. The flight patterns of insects and small birds have evolved over many millions of years to employ and exploit unsteady aerodynamic lift generating mechanisms in the most efficient way possible. To adequately understand natural flapping-wing flight, aerodynamicists should be able to distinguish: (1) what the flyer does with its wings, (2) if that offers a flight performance benefit, and if so, (3) which aerodynamic mechanism is responsible for the performance increase. To meet this challenge, current aerodynamic research frequently utilizes robotic flapper mechanisms. These robotic flappers can perform a flapping wing motion, are equipped with force sensors, and the test setup can be equipped with flow visualisation equipment. This way, points 2 and 3 can be researched simultaneously for a given motion. If all motions are understood, and if it is understood how the flow structures associated with these motions interact with each other, it will be possible to design an efficient mechanical flapping wing MAV, without having to rely on merely replicating insect wing movement, or having to rely on cumbersome trial and error methods.

In this thesis, the investigation focuses on the force data acquisition of robotic flappers. As will be demonstrated, it is difficult to accurately measure the force production with the current state-of-the-art for a flapping type of motion. The difficulty stems from the fact that the measurement setup needs to be designed for a minimal influence on the flow field, and has to contain numerous force sensors and actuators. This often results in a structure consisting of long, thin supports, with numerous interfaces and degrees of freedom. It is very difficult to keep all the vibrational modes of such a structure at a suitably high frequency in order to avoid interference with the force measurements. This will be demonstrated in the literature review.

The investigation is threefold. One part of the investigation is a parametric investigation on a revolving wing that accelerates from rest at a fixed pitch angle, where each consecutive experiment has the wing mounted at a different angle. The forces on the wing due to this kind of motion are relatively well understood, and these measurements are in part used to validate the Deconvolution Kalman filter.

One part is a similar parametric investigation on a flapping motion that replicates the wing rotation performed by an insect. This is a more complex motion, of which the force generation is less well investigated, and is more difficult to investigate as the motion kinematics are more impulsive, which leads to a more impulsive loading of the support structure.

The third part of the investigation deals with the Deconvolution Kalman filter in an effort to improve the filtering of the measured forces. In the study of Ahlfeld [1] this filter was implemented for a similar problem, which showed promising results and was reported to be implemented with some ease. This filter is applied for the measurement setup at hand, and compared to the current state-of-the-art. The process to implement this filter is also demonstrated in detail. The Deconvolution Kalman filter is investigated for validity, adaptability for the different motion kinematics, and in terms of influence on the signal to noise ratio.

This thesis is set up as follows: First, the literature review (Chapter 2) discusses the state-of-the-art

in flapping wing research. The described complex kinematics of flapping wings are discussed, and the current state-of-the-art is shown in terms of typical test setups and processing methods. This study mainly focuses on force generation, but research in flow visualization is also described briefly, both to show the state-of-the-art, and to help the reader better understand the described unsteady lift generating effects. Lastly, the current progress in force estimation models is shown. In Chapter 3 the experimental setup that is used in this study is discussed, including the kinematics used in this investigation. The improved filtering is discussed in detail in Chapter 4. The results of the measurements are shown and discussed in Chapter 5. Chapter 6, the final chapter, presents the conclusions from the previous chapters, and contains recommendations for future work.

2

Literature Review

2.1. Advantages of flapping wing flight for small scale flyers

For small length-, and velocity scales, it is very challenging to design an efficient flyer [34]. This leads, for fixed- or rotary wing MAV's, to short flight endurance and limits to how small a flyer can be made. In contrast, flapping-wing aerodynamics is different from rotary-wing or fixed-wing flight in that unsteady aerodynamic effects can be exploited to generate more lift for a given power requirement. Dickinson et al. discussed these unsteady aerodynamic mechanisms in [19]. In nature, flapping wing flight is the only form of small-scale flight, a testament to the efficiency of this flight strategy. At larger scales, the aerodynamic advantages of flapping wings decrease, and the physical drawbacks of accelerating and decelerating large wings become dominant. This can be seen in nature in the flight strategy of larger birds. Large birds flap very little and glide through air for large amounts of time, where the considered aerodynamics are more similar to those of airplanes than those of insects, as discussed by Denny [17].

2.2. Kinematics of flapping wing flight

A logical first step in investigating flapping wing flight is to observe and learn from the wings and wing movement of natural flyers. The flight patterns of insects and small birds have evolved over many millions of years to employ and exploit unsteady aerodynamic lift generation mechanisms. This has resulted in highly complex wing motion kinematics, which change depending on flight phase of the flyer.

2.2.1. Reference frames

To get a grip on the kinematics of insect wings, it makes sense to lay the groundwork from which those movements are defined first. To do so, a generic insect is drawn in Figure 2.1, with the body parts named and defined. To describe the position of these body parts in relation to each other, reference frames are needed: an insect body-bound reference frame, and a wing-bound reference frame. These are shown in Figure 2.2 The insect body reference frame has its origin at the center of gravity of the insect body, with the axes the principal axes of inertia of the body of the insect, denoted with the $_b$-suffix in Figure 2.2. As the insect moves its wings around the wing root, it makes sense to define a new reference frame around the wing root to simplify the motion of the wing itself [60]. This wing-root reference frame has its origin at the wing root, and the relevant axes have the $_r$ suffix in Figure 2.2. The Z_r-axis is perpendicular to the stroke plane. This stroke plane is defined by the points in space of the wing tip at the extremities of the motion and the wing root. The X_r-axis is the intersection of the body X,Z plane with the stroke plane. with the body length axis of the insect. The Y_r-axis follows from the X_r- and Z_r-axes. The last coordinate system needed is the wing-coordinate system, with axes Y_w, X_w, and Z_w. The Y_w axis is from the root to the tip of the wing, the X_w axis is from the leading edge to the trailing edge, and the Z_w axis is perpendicular to both Y_w and X_w. It follows that the origin lies along the root-to-tip line and on the wing surface. The spanwise position is not defined from the definition of the axis. In this thesis, the origin is placed at the tip of the wing for reasons of convenience.

The flyer body also moves around in space, which has a large influence on the forces on the insect. However, for convenience and tractability of the problem, the flyer body is chosen to be stationary.

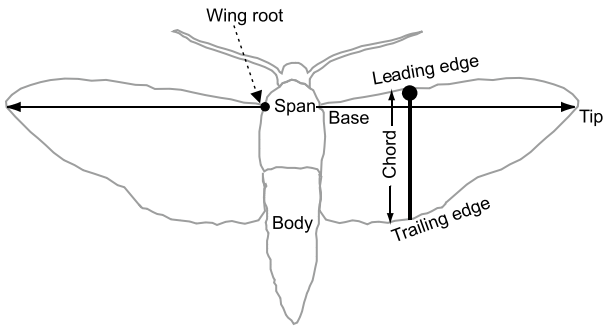

Figure 2.1: General insect body with nomenclature, adapted from [56]

2.2.2. Wing position

The position of the wing can now be defined in relation to the body, assuming a rigid insect body using the set of angles as defined in [60]. In reality, there are nine Euler angles to be defined as there are three reference frames (assuming a rigid body, no displacements are possible between the reference frames), however those are not usually considered relevant in the literature of an insect in steady motion. For a flyer performing flight maneuvers, all these angles need to be named and defined as the flyer moves its body and stroke plane in response to its surroundings [24]. Again, this is outside the scope of this discussion, as in general only hovering flight is discussed in literature [20]. As long as the body posture is constant and the body does not move around in space, only five angles need to be defined. The angle between the stroke plane and the body length (X_b) axis is the stroke plane angle β (Figure 2.2B). This angle defines the the wing root reference frame with respect to the body reference frame. Rotations of the wing-root reference frame in the X_b, Y_b- or Y_b, Z_b plane are assumed to be zero and frequently not mentioned [60]. The Euler angles between the wing-coordinate system and the wing-root coordinate system are all used in literature. The angle between the Y_w and Y_r axes is the stroke angle ϕ (Figure 2.2A), the difference between the maximum and minimum stroke angle is the stroke amplitude Φ. A change in stroke angle is effected by sweeping the wing. The angle between the Y_r, X_r plane and Y_w is the elevation angle θ, also described as heaving angle in [36] (Figure 2.2B). Changes in the elevation angle are usually described as 'plunging motion'. The last angle is the angle between X_w and the Y_r, X_r plane (stroke plane). This is the pitch angle α, which coincides with the angle of attack for a hovering insect (Figure 2.2C). Pitching the wing is used to describe a change in α. For classical thin-airfoil theory, the angle of attack is not the same as the geometrical angle of attack as the flow around the wing induces a change in angle of attack and the tip vortex decreases the angle of attack near the tip. In flapping-wing literature, it has been acknowledged that a similar angle of attack is very difficult to define as the flows are highly unsteady and frequently detached [56]. Also, for natural flyers, the wing is usually designed to flex under flight, and flexibility effects change the real angle of attack over spanwise and chordwise positions. Wing flexibility is not further explored in this thesis.

2.2.3. Insect wing motion

As the reference frames and relevant angles are defined, and the wing can be located in relation to the insect body, the motion itself can be explored. General insect wing motion is shown in Figure 2.3, for *Drosophila Melanogaster*, or a fruit fly. The motion shown is representative, but in general, an insect changes its wing motion based on flight objective. [36, 57]. The wing motion of an insect consists of two phases: the upstroke, and the downstroke. The upstroke is roughly the phase of the the stroke where the wing is swept from the front of the insect (ventral side) towards the rear of the insect (dorsal side). At the end of the upstroke, the stroke reverses, and the downstroke starts. During the downstroke, the wing is swept back from the dorsal side to the ventral side, at which point the stroke is reversed and the upstroke phase starts again. Reversing the stroke at the ventral side is called supination, stroke reversal at the dorsal side is called pronation. Between these phases, the wing is pitched, with the bulk of the rotation happening over a short timespan at or around the pronation and supination phase. The timing of the wing pitching, and the elevation angle during rotation are changed depending on flight goal [36]. During the upstroke and downstroke, the wing is plunged up and down, generally out of phase with the upstroke and downstroke (as illustrated in Figure 2.3). Deviations from the general motion are discussed at length by Zanker [68] where a tethered fruit fly was observed using strobe photography.

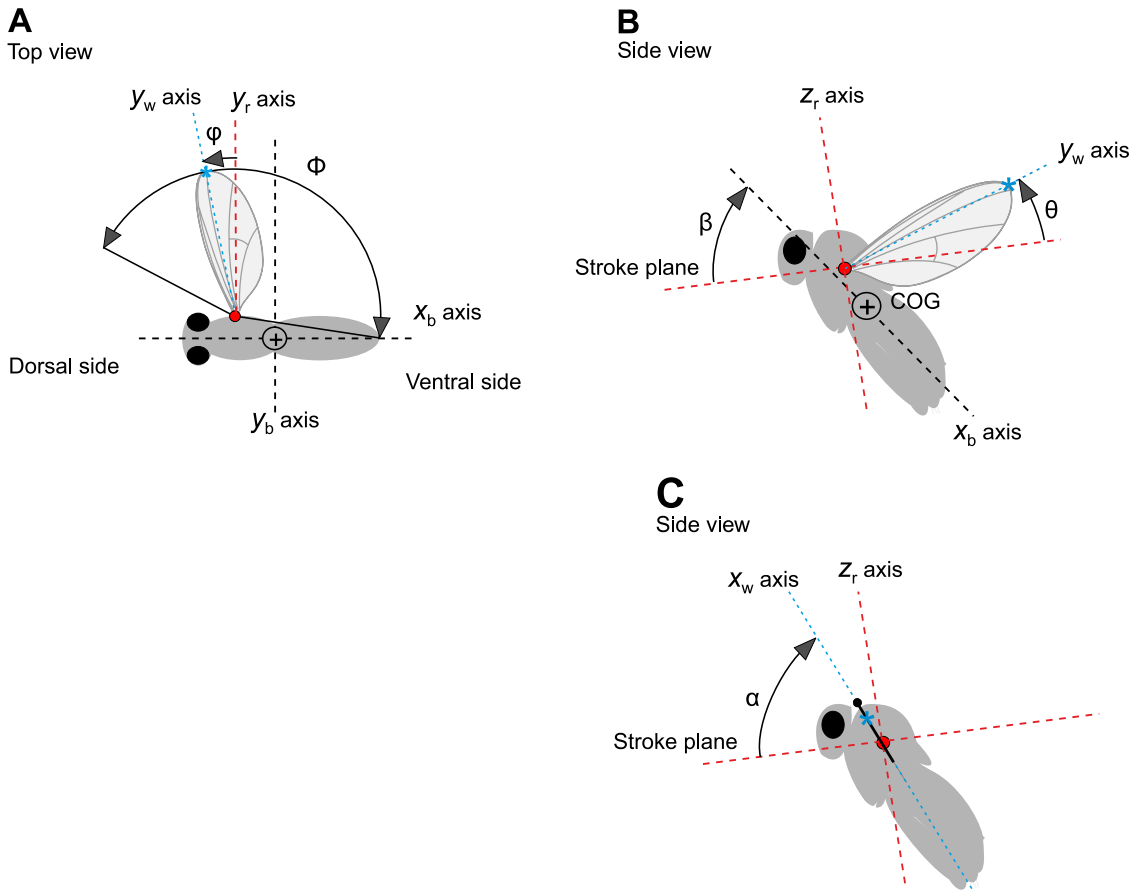

Figure 2.2: Relevant angles and of the insect body and wings, adapted from [37]

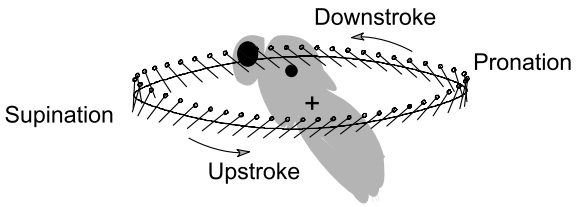

Figure 2.3: Typical insect wing motion, adapted from [37] and [56].

2.2.4. Experimental approximation of insect wing motion

For experimental use, the wing motion itself is frequently simplified. The wing motion can be observed to consist of mainly the up- and downstroke (changes in ϕ), with a wing rotation (changes in α) in between. The plunging motion (changes in θ) is then small compared to the other motions. To limit the complexity of the experimental setup, the motion is frequently approximated to consist of just stroking and pitching motions [5–8, 12, 18, 19, 29, 30, 41, 49, 58, 69]. In flapping wing experiments, these are usually termed 'revolving' and 'pitching' motions. An acceleration component in the revolving motion ($\ddot{\phi}$) is frequently described as 'surging'. [49].

2.3. Scaling parameters

There are numerous biological flyers, with very different wing sizes and flapping strategies. This leads to the difficulty on how to adequately interpret the conclusions drawn from the observed flows and forces of one flyer to the observed flows and forces of another flyer. To this end, scaling factors have been invented. A general introduction on scaling factors used in steady aerodynamics can be found in reference textbooks such as [2]. In this report, it is assumed the reader is familiar with concepts

such as air density (ρ), dynamic viscosity (μ), dynamic pressure ($q_\infty = \frac{1}{2}\rho_\infty U_\infty^2$), Reynolds number ($Re = \frac{\rho_\infty U_\infty l}{\mu_\infty}$), and force coefficients (force/q_∞).

In the introduction of this chapter, the mentioned inefficiency of small flyers compared to larger flyers is related to the Reynolds number. The length scales and speeds involved for MAV's, insects, and small birds are much smaller, which leads to a lower Re. For steady aerodynamics, this results in lower attainable c_L/c_D ratios, and therefore less efficient wings [47]. In general, for steady aerodynamics, the Reynolds number is the most used scaling parameter.

The state of the art in scaling for flapping wings is the investigation by Lentink and Dickinson [40], where the following scaling parameters were found to be relevant for flapping wing flight:
(1) The Reynolds number of the time-averaged air speed U at the radius of gyration (R_g) of the wing. R_g is defined in Formula 2.1, where r is the radial position, R the wing radius, $c(r)$ the wing chord depending on radial position, and S the wing surface area.
(2) The angular acceleration number C_{ang} (Equation 2.2), which is the rotational acceleration of the flow divided by the convective flow acceleration. Ω is the angular velocity of the wing.
(3) The Rossby number Ro (Equation 2.3), which is the Coriolis acceleration divided by the convective acceleration.
(4) The centripetal acceleration number C_{cen}, which is the centripetal acceleration divided by the convective acceleration, and reduces to the Rossby number for hovering flapping wing flight as discussed in this report.

In other literature, more scaling parameters are in use [60] [58], which relate more to wing motion and wing shape than fluid-dynamic accelerations. These are the reduced flapping frequency k, the aspect ratio of the wing AR, and the Strouhal number St. The reduced flapping frequency is shown in Equation 2.4, in which f is the flapping frequency in Hz, and Φ the total wing sweep angle as mentioned earlier. The reduced frequency compares the spatial wavelength of the flow disturbance to the chord length; providing a measure of unsteadiness. The reduced frequency is also used for measurements that isolate pitching motion, where $k = \frac{\dot{\alpha}c}{2U}$. [25, 49]. The aspect ratio AR is the ratio between the square of the span (R), divided by the wing surface area S (Equation 2.5). For square wings, this is the same as the span divided by the chord. Note that the span for flapping wing flight usually denotes the span of a single wing. The Strouhal number (Equation 2.6) also provides a measure of unsteadiness, but is more useful for forward flight which is not discussed in this thesis. V_{inf} is the speed of forward flight if the insect is not stationary. Furthermore, scaling parameters for flexible wings exist, but as wing flexibility is outside the scope of this thesis, these are not discussed.

Finally, for experiments concerning flapping wings, the time is usually non-dimensionalized as well. This is a topic where little consensus in literature has been achieved. Some papers use time in seconds such as [58, 69], others use the amount of chords travelled from the start of the motion, with either the wing tip, radius of gyration, or 75% chord as reference [60], some use fractions of the total up- or downstroke [64]. Wing sweep angle (ϕ) is also used [5]. In this thesis, the convective time t^* (Equation 2.7) will be predominantly used, as in [49]. In Equation 2.7, t is the elapsed time in seconds, U the reference velocity at the reference span position and c the chord length.

$$R_g = \sqrt{\frac{1}{S}\int_0^R r^2 c(r)dr} \tag{2.1}$$

$$C_{ang} = \frac{U^2}{\dot{\Omega}Rc} \tag{2.2}$$

$$Ro = \frac{U^2}{\Omega^2 Rc} = R/c \tag{2.3}$$

$$k = \frac{\pi f c}{U} \tag{2.4}$$

$$AR = \frac{R^2}{S} \tag{2.5}$$

$$St = \frac{AR\Phi}{2U_\infty} \tag{2.6}$$

$$t^* = U \times \frac{t}{c} \tag{2.7}$$

2.4. Unsteady force generation mechanisms

As discussed in the introduction, it is very challenging to design wings for steady airflow that still generate acceptable lift at low Re. However, unsteady aerodynamic mechanisms can be exploited to generate more lift. Most notably, insects and small birds have adapted themselves to become proficient at utilizing unsteady aerodynamic mechanisms to stay aloft. These mechanisms have been listed and discussed in review papers [36, 56, 60], and the convention of the review paper of Shyy et al. [60] is followed in this thesis. The unsteady mechanisms discussed are :

- A pronounced Leading Edge Vortex (LEV) which stays attached during the motion instead of convecting away
- Rotational forces generated as the wing pitches
- Wake Capture which indicates that the insect utilizes the wake of the previous stroke to increase the force production for the following stroke
- Clap and Fling, which happens at the pronation and supination phases where the insect wings meet and the wing-wing interaction is used to increase generated lift
- Tip Vortex (TV) which can increase generated forces by interacting with the LEV
- Added mass (although not strictly an unsteady aerodynamic effect as will be explained later)

2.4.1. Leading Edge Vortex

A wing that either starts to translate at an angle of attack that is too high for the flow to stay attached, or dynamically attains this angle of attack while translating, will generate a vortex on the upper side of the leading edge of the wing. The presence of this Leading-Edge Vortex (LEV) allows the wing to generate high amounts of lift as the LEV adds circulation to the wing as the flow around the vortex core reattaches to the wing, and the wing, together with the LEV, satisfies the *Kutta condition*, which states that at the trailing edge, the flow coming from the top of the wing moves parallel to the flow coming from the bottom of the wing [36]. As the flow curves over the attached vortex and reattaches before the wing trailing edge, it is accelerated, giving rise to a force normal to the wing surface. As time progresses, the LEV grows until the flow cannot satisfy the Kutta condition anymore. The vortex then detaches and is convected away with the rest of the flow. The wing is still at an angle of attack larger than that stall angle, thus at the leading edge, the flow is still separated, and the wing loses a large portion of the generated lift. This phenomenon is called 'dynamic stall' and is very important to helicopter flight, as the angle of attack for the rotor blades changes constantly as the helicopter moves forward and the rotor blades rotate. The constant generation and shedding of LEV's leads to a complex loading on the rotor. This dynamic stall is therefore considered at length in textbooks such as [39]. As stated, the LEV convects away for translating wings. However, in flapping wing flight, this LEV stays attached. This was first observed by Ellington et al. [23], where the attached LEV was also identified as a main factor for the lift generated by a flapping wing, which is higher than what steady aerodynamic theory would predict. In Figure 2.5, the spanwise vorticity of a revolving and flapping insect wing is visualized for a single downstroke. Amongst other features, the LEV is prominently visible as the region of blue vorticity near the leading edge of the wing for much of the downstroke. The LEV begins to form at $\hat{t}$=0.02, as the small blue dot at the top of the leading edge, and grows steadily until around $\hat{t}$=0.12. During this growth, another opposite vortex grows at the trailing edge, called the Translational Starting Vortex (TSV) by Birch et al. This TSV convects away, but the LEV stays attached. and persists up until $\hat{t}$=0.43, where it ceases to be identifiable due to the wing rotation. The differences in sustained generated lift and drag coefficients between a revolving wing and a translating wing are illustrated in Figure 2.4. It is observed that although the lift increases proportionally with the drag, the overall force generation is

greatly increased. In the paper by Ellington [23], a similarity between the LEV for a flapping wing and the LEV for delta wings was observed. Delta wings at high angles of attack also feature LEVs that stay attached due the component of the flow in line with the axial direction of the vortex, which stabilizes the LEV by convecting away generated vorticity, which keeps the size of the LEV such that the flow can reattach.[65] [36]. In [23], an axial flow in the vortex core was observed, which was hypothesised to have a similar stabilizing effect to the spanwise of delta wings. This axial flow was not observed to be large enough to stabilize the LEV by Birch and Dickinson [6]. In [6], chordwise wing fences were installed on a dynamically scaled wing of a fruit fly, which would impede the axial flow through the core of the LEV. However, the LEV did not detach. A different hypothesis as to why the LEV stays attached was given in which the downwash induced by the tip vortex and wake vorticity is the main factor in stabilizing the LEV. In [6], a fruit fly wing was modelled, with a Reynolds number of 160. In [23], a hawkmoth was investigated, which flies at a Reynolds number of around 6000 [60]. However, Birch and Dickinson stated that as the spanwise axial flow was found to be not essential for LEV attachement at Reynolds numbers of around 200, it would also be not essential at Reynolds number of over 2000. The dissimilarity in LEV core axial flow at different Reynolds numbers was also observed computationally by Aono et al. [3], where it was stated that the mechanism for LEV stability would be the same for both the lower- and higher Reynolds number cases. It was offered that the accelerations due to the sweeping of the wing, as discussed in Section 2.3, could be the source of LEV-stabilizing spanwise flow components outside the LEV core. Lentink et al. [41] related the angular accelerations due to wing revolving motion, most notably the Rossby number, to LEV stability as well. This stabilizing effect was observed to be independent of Reynolds number, and therefore also valid for large birds as well as insects. Clearly this has been the subject of intense research, with the latest development in understanding why the LEV stays attached by Lentink et al. [41], where the centripetal- and Coriolis accelerations, as quantified by the Rossby number, are proposed as the main contributors in stabilizing the LEV. The downwash due to wake vorticity was described as incorrect since this hypothesis would also hold true for a translating wing, but a translating wing shows no prolonged attachment of the LEV. As shown in [51] and [62], the LEV does not stay coherent and attached indefinitely as it was found that the LEV seems to burst and lose coherence after around 4 chord lengths of travel. It was found that the force enhancement effect does not decrease after the LEV has lost coherence. As well as using flow visualization on live insects, as in [9, 23, 35], experiments on the LEV attachment are performed using dynamically scaled robotic flappers, for either describing the characteristics of the LEV [6, 15, 16, 22, 28, 29, 32, 41, 48, 62], or parametric studies investigating the influence of the aspect ratio [14], Reynolds number [8, 30, 41], Rossby number [41], Incident flow [13, 20], pitching motion, [12, 49], and α. [32, 41, 51]. Of these parametric studies, [28–30, 41, 49, 51, 62] also include force measurements of the wing. Numerical simulations are also employed to investigate the leading edge vortex developments. However, the agreement between numerical investigations and mechanical experiments is not perfect [28], with the numerical method having difficulties locating the vortices in time and space. Qualitatively, the agreement between experiment and numerical is considered good. Numerical investigations are ideally suited for parametric studies. In [11], the effects of α, stroke pattern, Rossby number and Reynolds number are investigated. In [43], the wing planform shape, aspect ratio and wing corrugation are numerically investigated.

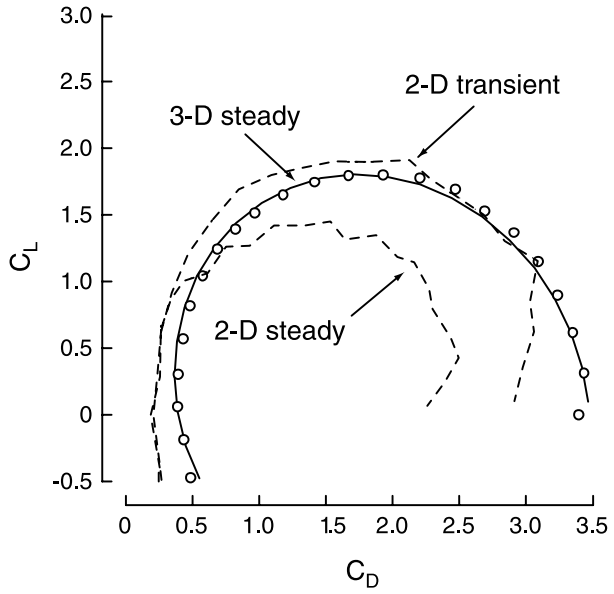

Figure 2.4: Lift-drag polars of translating (2D) and revolving (3D) wings at comparable Reynolds number, adapted from [18].

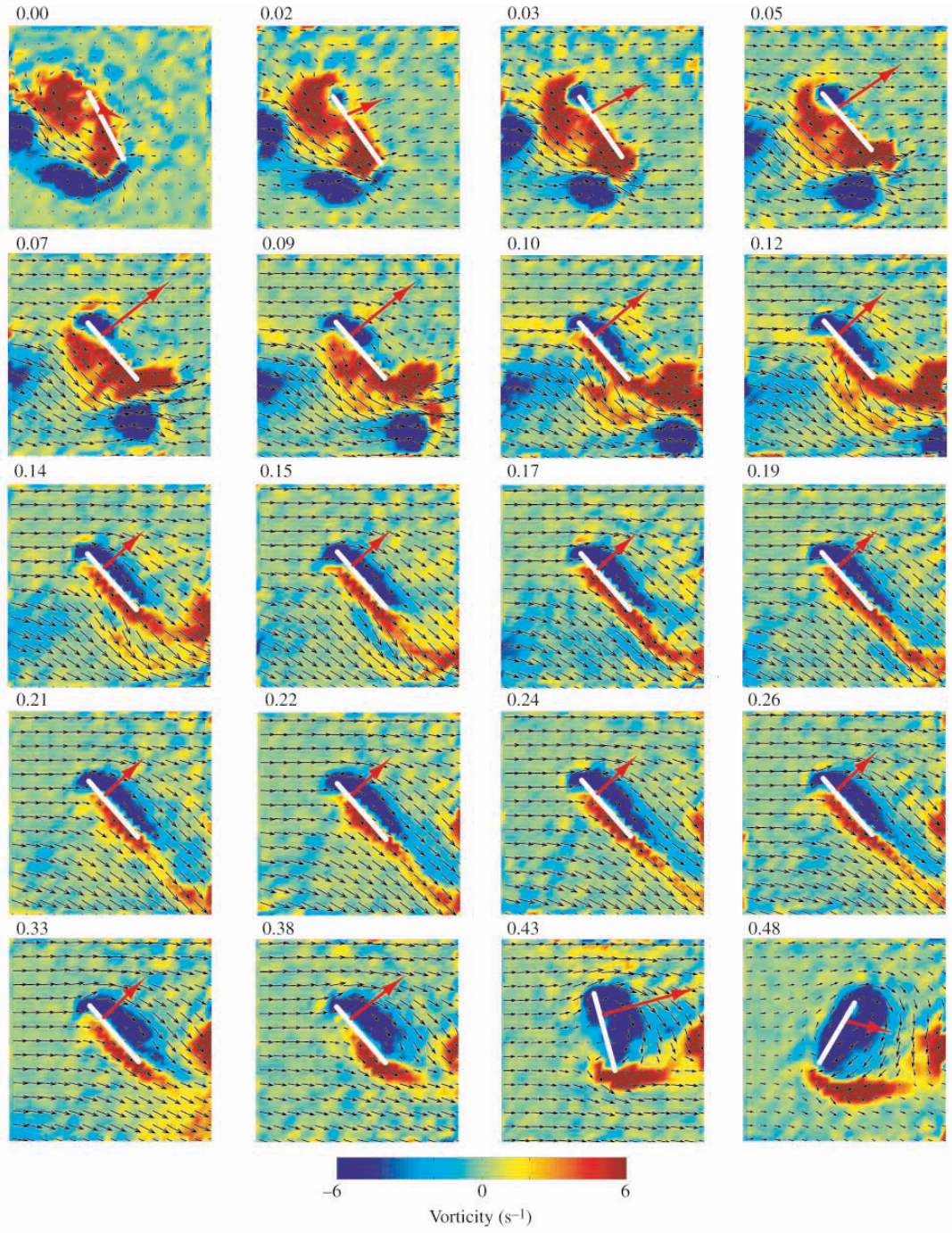

Figure 2.5: Spanwise vorticity at 65% of the span during the fourth downstroke of a scaled flapping fruit-fly wing, obtained using DPIV by Birch et al. [7], numbers in the top-left corner of each image denoting time in fractions of the complete down-upstroke motion ($\hat{t}$), where 0 is the start of the downstroke, and 0.48 is the start of the upstroke. Re=160, Ro=2.9 ([41]). Red arrow denotes captured force vector. Note that the kinematics are such that during the downstroke, the wing rotates before reaching the end of the stroke.

2.4.2. Rotational Forces

As the wing undergoes a pitching motion, the rotation of the wing generates circulation and therefore lift. This force augmentation mechanism was not under great scientific attention for flapping wing investigations, but was first mentioned by Dickinson et al. [19] and researched more in [58]. The effect is qualitatively similar to the Magnus effect, but the mechanism is quite different, as the rotational forces add lift as the flow tries to establish the Kutta condition. In contrast, the Magnus effect does not rely on the Kutta condition as it only applies to blunt bodies. According to Sane [56] this effect is the same as the effects described by Kramer [33] in the early 1930s, but more focussed on high-Reynolds number, attached flow for flutter phenomena. However, Lehmann [36] states that the Kramer effect is a separate effect that may or may not be of influence for the force generation of insect wings. To estimate the magnitude of the rotational forces, Sane and Dickinson used the Kutta condition, assumed that it was valid at the angles of attack of insect flight and used the blade-element method. This method suggests that the lift generated depends on the distance of the pitching axis from the three-quarter chord point [56]. This effect generates substantial force augmentation for insect flight, but only for the duration of the pitching motion, leading to high transient force peaks [19]. This can also be observed in Figure 2.5, for $\hat{t}$=0.38 to 0.48, in which the wing rotates, increases the magnitude of the LEV, which is then balanced by an increase of vorticity at the trailing edge called the Rotational Starting Vortex (RSV) by Birch et al. [7]. During this generation of vorticity, a high force peak is generated. In [49], the forces generated when the wing is rotated are shown to match predictions of the quasi-steady model of [19], and the flow over the wing underlying the force generation are visualized and quantified using tomographic particle image velocimetry (PIV). For a translating wing, these rotational forces are parametrically investigated for pitching rate by Grandlund et al. [25] for pitching axis location and pitch rate. It was found that for these translating plates and for higher pitching rates, the pitching motion induced different effects at different pitching rates. The observed forces that can be related to rotational forces as opposed to those related to inertial effects are concluded to be more prominent for higher pitch rates and their magnitude is proportional to the distance of the pitching axis location from the three-quarter chord point. Again, this is in agreement with the assertions of the quasi-steady model of [19]. For lower pitching rates, this quasi-steady model was not found to be sufficient, and a time-based scaling of the pitch-rate induced effects, based on the pitch-axis location was proposed. Yu et al. [66] performed a parametric investigation based on planform shape of the wing for a translating-pitching plate. It was found that in general, a tapered plate had a higher generated lift coefficient. It was also found that, all wing planforms share the same trend in force generation development during the experiment. To the author's knowledge, there are no similar parametric studies for revolving wings.

2.4.3. Wake Capture

As the wing decelerates before the reversal of stroke (either pronation or supination), the vortical structures around the wing are shed into the wake. When the wing accelerates again, the previously shed wake is encountered. Using this shed wake to increase lift is termed 'wake capture'. This effect is visualized for butterflies in [61], where it was reported that butterflies can choose to move their wings through the shed vortex, and that sometimes the flight goals of the insect are such that the effect is beneficial, but sometimes not. In [61], it was reported that wake capture is a way to increase efficiency of the flight mechanism. This is in agreement with the statements in [18], where it was found that moving the wing through the wake greatly enhanced lift for a robotic flapper, but that the effect was highly sensitive to changes in kinematics. Time-wise, the force augmentation by wake capture effects are close to those of the rotational forces as wing rotation and wake capture happens around the supination and pronation phases. Dickinson et al. [19] used Particle Image Velocimetry (PIV) and force measurements on a robotic flapper to demonstrate that these two effects are separate from each other, where the wake capture was described as greatly improving the overall efficiency of force generation. The robotic flapper used had only one wing. Generally, flapping-wing flyers have two wings, and the presence of this second wing is hypothesised to diminish the effectiveness of the wake capture mechanism in [36], however as the wake capture effect is very dependent on specific kinematics, and the effect was expected to be small, no hard claims were made if the presence of the second wing would enhance or decrease the effectiveness or efficiency of the wake capture mechanism. The wake capture mechanism can be described as a collection of associated effects as shown by way of PIV experiments in [7] (adapted in Figure 2.5) and [16]. In Figure 2.5, the wing-wake interaction process can be observed from $\hat{t}$=0 to 0.09. At $\hat{t}$=0, the large red region is the shed LEV from the upstroke,

the leftmost dark blue region is the shed RSV. Between these vortices, a jet of fluid is accelerated and directed at the lower side of the wing, resulting in a force peak. This generation of the new LEV starts, and at the end of the downstroke, a similar (with reversed vorticity) flow structure is visible with an LEV and RSV about to be shed, which will result in a new jet during the start of the upstroke.

The early part of the wake capture, where the 'fluid jet' directs fluid to the underside of the wing is not considered part of wake capture by Jardin et al. [28], where it is called 'dipole jet'. This produces a high transient lift peak. Jardin et al. [28] describe the interaction after the 'dipole jet' phase as enhancing the lift as the wake interaction allows the new LEV to form more closely to the wing. It was again noted that this interaction is highly dependent on exact kinematics and wing flexibility. In [28], little wake capture lift enhancement was found from shed vortex interaction, whereas Perçin et al. [50] observed that the wake capture effect is only present for the case of flexible wings for the experimental configuration and motion kinematics they considered in the study.

2.4.4. Clap and Fling

The insect wing can interact with its own shed wake, but also with the other wing. As the insect wing revolves, it meets the other insect wing at the end of the upstroke. Sane [56] describes it as such (see Figure 2.6): As the leading edges of the wings approach each other (A), the trailing edges follow (B), which pushes out the air between the between them (C), giving a net rise in force. This is the 'clap' phase. Following the 'clap' phase, the 'fling' phase starts, where the leading edges start to move apart with the trailing edges stationary (D). This motion creates a low pressure region between the wings, which sucks in air from above, adding circulation to the wing (E+F). The 'clap' phase was found to be detrimental to the total force production by Lehmann et al. [38], but the 'fling' phase created a larger LEV, augmenting the generated force for the entire downstroke. Later investigations by Lehmann et al. [37] found that the effectiveness of the clap and fling mechanism is highly dependant on kinematics. For biological flyers, this dependency on kinematics means that if the clap and fling effects align with the flight goal the, mechanism is utilized by the flyer. Some insects use the clap and fling just for lift-off, or just for maneuvers. The clap and fling motion is sometimes called 'clap and peel' for flexible wings as the wings are pulled apart in a peeling motion. Wing flexibility is another factor influencing the highly complex clap and fling motion. Miller et al. [46] found that flexible wings were much more efficient at utilizing the mechanism.

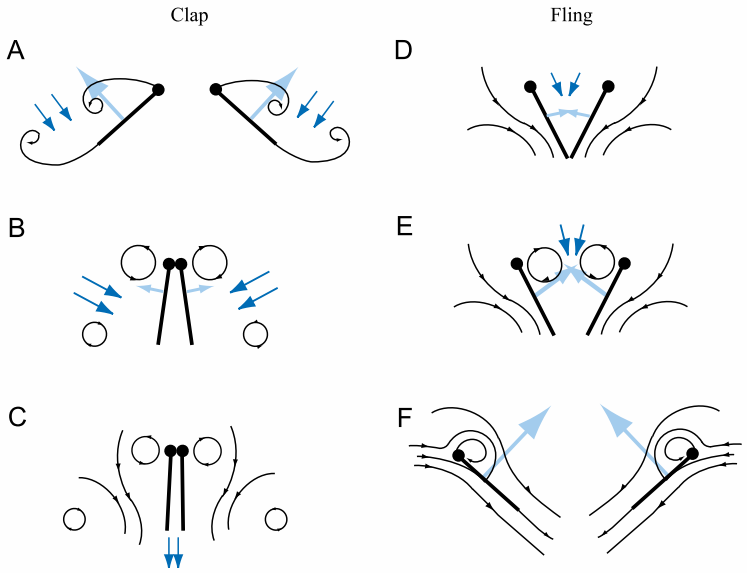

Figure 2.6: Clap- and Fling motion schematic. The wing chord is shown with the same convention as in Figure 2.1. The light blue arrows are the generated force, dark blue arrows the induced flows, black lines with arrows the flow lines. Adapted from [56].

2.4.5. Tip Vortex

For steady translating flight, the Tip Vortex (TV) is usually associated with loss of lift and increased drag. However, for translating low-aspect ratio wings at $Re = 1 \times 10^3$ suppressing the tip vortex leads to a decrease in normal force generation as found by Ringuette et al. [54]. A similar kinematic was numerically investigated by Shyy et al. [59] where it was found that the tip vortex could, depending on kinematics, help 'anchor' the shed vortex from the leading edge. A similar statement for revolving wings was made in the paper by Birch et al. [6], where it was hypothesized that the downwash from the tip vortex limits the effective anglef of attack, and therefore the growth of the LEV, keeping it attached. The review paper by Shyy [60] therefore includes the tip vortex as an unsteady lift-enhancing mechanism. However, the described 'anchoring' effect for the LEV was dismissed by Lentink et al. in [41] as described in section 2.4.1. Numerical simulations suggested that the TV could, depending on wing kinematics, enhance the force production. [60]. Papers discussed in Chapter 2.4.1 don't consider the TV as separate unsteady lift generating mechanism, but for all the cited measurements, the TV is a prominent flow feature. Aono et al. [3] considered the TV a part of a 'ring-shaped' vortex consisting of the LEV, TV and Trailing Edge Vortex (TEV), which forms around the wing, see Figure 2.7. The vortex called TEV by Aono et al. is called TSV by Birch et al. [7].

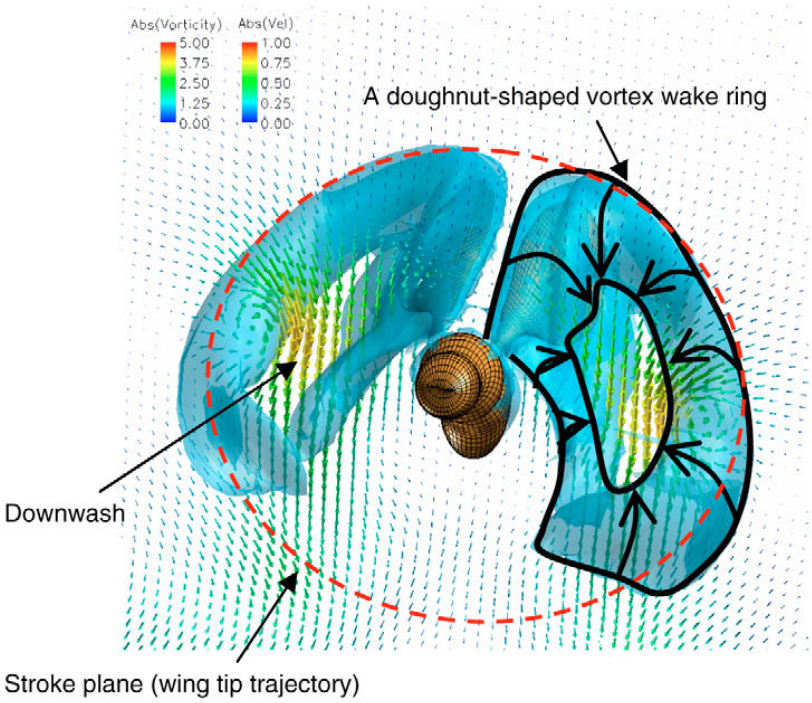

Figure 2.7: Ring-shaped vortex structure comprising the LEV, TV, and detached TEV, adapted from [3].

2.4.6. Added mass

The last force augmentation mechanism described is the only non-circulatory effect, meaning the force augmentation is not related to flow around the wing. This effect is termed 'added mass', as when a wing accelerates, fluid is accelerated by the wing, and in accordance with Newton's third law, this gives an opposite reaction force on the wing. This effect is not under a great research focus, although both the review papers of Lehmann [36] and Sane [56] discuss the added mass force and call for more research on added mass force generation. On the other hand, in [20], the added mass was found to be small, and in agreement with simple estimates.

2.5. Modeling and measurements of flapping wings

2.5.1. Quasi steady modeling

The listed fluid-dynamic effects in the previous section not only complicate force measurements, but also complicate the design of flapping wing measurement apparatuses and experiments on flapping wings, as it is difficult to predict beforehand what forces will be generated, at what points in time. Also for future MAV design, quick estimation tools are needed. To this end, a revised quasi-steady model is suggested by Sane et al. [58]. This quasi-steady model consists of three components: a "steady" force corresponding to that generated by the instantaneous motion velocity and angle of attack, a rotational force due to pitching rotation, and the contributions due to acceleration (added mass). This is expressed in Equations 2.8 to 2.11. Here, $\dot{\phi}$ and $\ddot{\phi}$ are the wing revolving velocity and acceleration, while α, $\dot{\alpha}$, and $\ddot{\alpha}$ are the pitch angle, velocity, and acceleration, $V_{0.75}$ is the tangential velocity at the reference three-quarter span position, c_N is the normal force coefficient, r is the spanwise distance from the revolving axis, c is the wing chord length, b is the wing span length. The "steady" force contribution of the revolving motion is given in Equation 2.9. The value of c_N is obtained from the measurements at conditions where a steady generated force value has been attained with the wing revolving at a constant angle of attack and a constant velocity. Therefore, this force contribution does take into account the an attached LEV or tip vortex effects (should those be generated). The rotational forces are described by

$F_{rotation}$. $F_{rotation}$ was obtained by assuming the Kutta condition also holds for large angles of attack. This leads to the notion that the lift generated by wing rotational velocity is zero if the wing rotation axis ($\hat{x}_0$) is at the 75% chord point. This approach has been discussed by Sane et al. [58], Dickinson et al.[19], and Granlund et al. [25]. The added mass effects are described by $F_{addedmass}$, based on blade-element theory and fluid accelerated with the wing. As can be observed, effects relating to the reversal of the stroke are not accounted for in this model (wake capture and clap-and-fling). However, the model can be used to estimate the relative magnitude of these effects. In [49], the model was found to offer adequate performance for the phase in the motion where the added mass forces were dominant, but the magnitude of the rotational force was overestimated, and the 'steady' part of the generated force shows a time lag. Quantitatively, the quasi-steady model described the generated force history in [49], but it must be noted that the kinematics were chosen such that no wake capture or clap-and-fling related forces would arise.

$$F_N = F_{steady} + F_{addedmass} + F_{rotational} \tag{2.8}$$

$$F_{steady} = c_N(\alpha)\frac{1}{2}\rho(V_{0.75})^2 bc \tag{2.9}$$

$$F_{addedmass} = \rho\frac{\pi}{4}c^2\ddot{\phi}\sin\alpha \int_{r_{root}}^{r_{tip}} r\,dr + \rho\ddot{\alpha}\frac{\pi}{8}c^3 b \tag{2.10}$$

$$F_{rotation} = \rho\pi c^2\dot{\phi}\dot{\alpha}(0.75 - \hat{x_0}) \int_{r_{root}}^{r_{tip}} r\,dr \tag{2.11}$$

2.5.2. Typical measurements with flapping wings

The earliest experiments intended to gain insight into the aerodynamics of flapping wing flight relied on filming or photographing free-flying or tethered insects, bats, and small birds. Sometimes, smoke was introduced in the airstream to visualize the flow. These experiments were generally focussed on kinematics and flow phenomena [23, 24, 68], but also recently filming insects has produced new insights [61]. However, living creatures are difficult to work with as their flight goals, and their associated kinematics can change between strokes. Also, the forces they produce are very small. For most current measurements, robotic flapping-wing mechanisms are used to investigate generated forces. Exactly replicating an insect wing, flapping it at the same frequency of an insect, and also measuring the produced force with a high degree of accuracy is very difficult. To overcome this problem, the flapping mechanisms usually use a much larger wing, and are situated in an a water- or oil tank. Reynolds scaling is then used to obtain a dynamically scaled flow as the biological flyer that was the inspiration. [6, 18, 19, 58, 69]. Such a setup allows direct force measurements, but also flow visualization as in [8, 12, 41], frequently this is combined such as in [5, 7, 29, 30, 49].

A robotic flapping mechanism allows the researcher to focus on a specific unsteady flow mechanism, such as LEV attachment or rotational forces. For a focus on LEV attachment, the kinematics are simplified in order to exclude the generation of other unsteady force generation mechanisms other than the LEV, which could interfere with the measurements of the LEV [20]. The kinematics are simplified by having only one wing, keeping α constant and only considering an upstroke without a plunging motion. This motion then starts with the wing at rest and at a certain α. The wing accelerates with a certain rotational acceleration ($\ddot{\phi}$) until a certain rotational velocity ($\dot{\phi}$) is reached. When a given ϕ is reached, the wing is stopped. This is termed a revolving-surging kinematic. This way, the wing does not move in its own wake, does not encounter the other wing and does not rotate, excluding the clap-and-fling, wake capture and rotational force effects. It is not possible to exclude added mass forces, or the influence of the TV on the flow field. The added mass force is generated by accelerations, and the TV is a feature that arises due to the finite span of the wing and the fact that the wing generates a net force.

Until recently, wing rotation effects were obtained from a kinematic simplification that also omitted the sweeping motion of the wing. The conclusions reached in [59] are based on a translating wing, as are the findings of Granlund et al. [25] and Yu et al. [67]. However, this simplification foregoes full dynamic similarity, as the Rossby number is infinite for a translating wing. A more valid and modern way to research the rotational forces on a flapping wing would be to pitch a rotating wing, as in [49].

This kinematic involves acceleration of the wing in similar fashion of the revolving-surging motion, with the exception that the wing is rotated from the starting α (usually zero) to a given α. The advantage of this kinematic is that the difference between the revolving-surging and revolving-pitching kinematics are attributable to the pitching of the wing, which allows the researcher to investigate the rotational forces more directly.

2.5.3. Data processing

Typical force measurements are done with a force sensor located at the root of the wing, and the reported values are in lift- and drag coefficients (c_L and c_D), with the reference velocity the obtained revolving velocity at the radius of gyration (as discussed in Chapter 2.3). Usually, the measurement is repeated multiple times for ensemble averaging the raw data. The ensemble averaged data is then filtered with either low-pass or moving-average filters to remove the electrical noise, generated by the sensor, the amplification system, and influence of mechanical vibrations [5, 8, 30, 44, 49, 58, 69]. This is explained clearly in [5] and [29], where the raw data is shown together with the filtering steps (Figure 2.8. Observing the picture it is clear that for the shown kinematics and used experimental setup, it is difficult to determine which part of the measured signal is due to fluid-dynamic forces and which part is due to noise or mechanical vibrations. Especially in the paper by Jones et al. [29], there are no changes in shape of the obtained forces for sinusoidal, linear, and exponential acceleration profiles, which is something that one would expect based on added-mass force estimates. This may indicate that the filtering frequency to remove noise was lower than the frequency components associated to fluid dynamic forces. On the other hand, spurious force peaks due to assumed test rig vibrations as a result of the impulsive start of the motion have been observed by Perçin et al. [49]. This could indicate the filtering frequency was too high. It therefore seems that it is indeed difficult to adequately filter out mechanical resonances on typical force measurement setups for revolving wings, undergoing impulsive motion. It might even be that when using only low-pass and moving-average filters, it might be impossible to obtain a suitable cut-off frequency that filters out the mechanical resonance and leaves the desired fluid-dynamic signal intact.

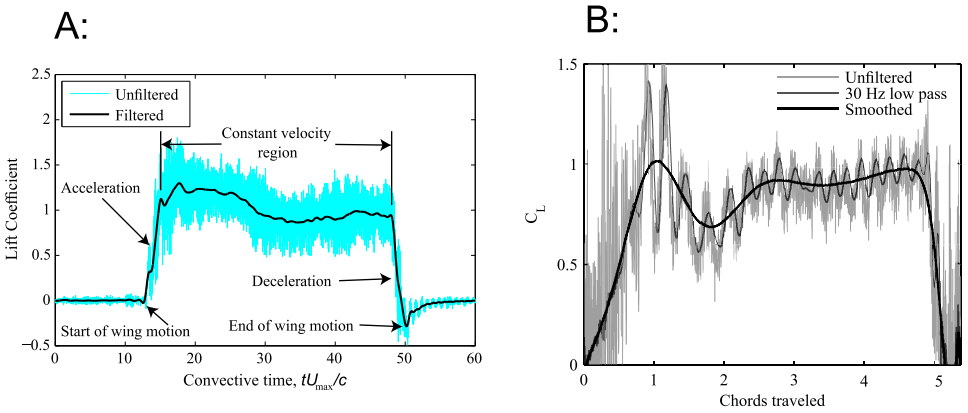

Figure 2.8: Filtered and unfiltered measured lift coefficients from [5] (A) and [29] (B).

To investigate the possibility of finding a suitable cut-off frequency, a linear simulation is performed. First, a synthetic force history corrupted by mechanical resonance was created. The uncorrupted force was obtained from the kinematics for the revolving-surging motion as described in [49], and the quasi-steady force model by Sane et al. [58], as was also used by Perçin et al. [49].

In the same paper by Perçin et al., the resonance frequency of the mechanical system was found to be 16.6 Hz. To get a representative response, a second order state-space model is constructed with a resonance frequency 16.6 Hz. The response of this system is shown by its Bode plot in Figure 2.9. The system is not intended to be physically representative for the actual experimental setup described, but merely represents a general spring-mass-damper system with a similar resonance frequency. By linear simulation of this state-space model using the quasi-steady force estimate as the input, a synthetic force history is obtained. This synthetic force history is taken to be representative of current measurement setups. To investigate the influence of filtering, the response is filtered using low-pass filters with decreasing cut-off frequencies, and moving average filter with increasing spans. The obtained filtered

force histories, together with the baseline quasi-steady force estimate, are shown in Figures 2.10 A and B respectively. Clearly, there is a significant drop in oscillatory behaviour with lower cut-off frequency or larger span filters. However, around the phases in the motion where there are peaks or valleys in the generated force, the lower cut-off frequencies or larger spans succeed in capturing the general shape of the motion, but the impulsive behaviour is lost, and the timing itself gets spread out, where the force generation appears to start earlier and stop later. Higher frequencies and shorter spans leave the oscillatory mechanical behaviour intact, obscuring the fluid dynamic force peaks. It can be concluded that a better filtering method is required for force measurements on revolving flapping wings undergoing impulse motion.

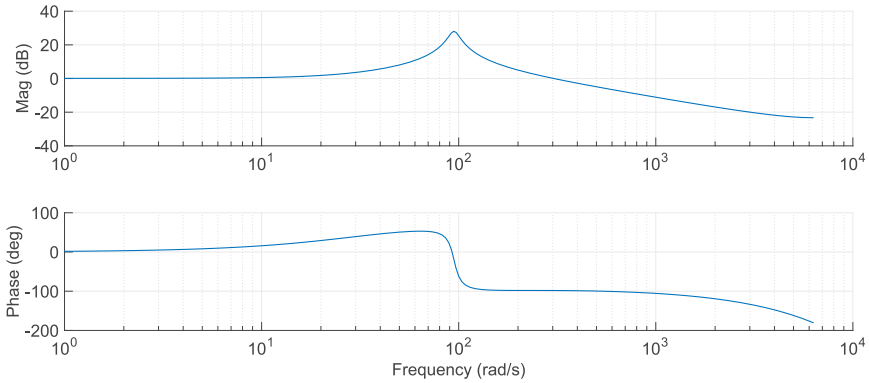

Figure 2.9: Bode plot of system used for testing conventional filtering methods

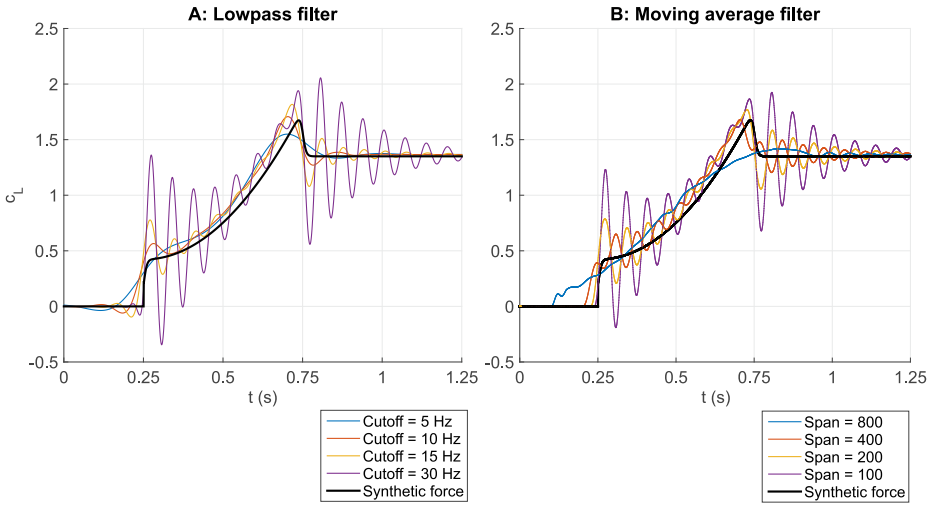

Figure 2.10: Filter performance of various Chebyshev Type II filters with shown cut-off (-80dB) frequencies, and various moving average filters with given spans. In this figure, the synthetic force would be the desired result.

2.6. Deconvolution filtering

In search of a better filter, similar problems involving vibrations of test structures interfering with force measurements were found in rocket test stands and force balances of hypersonic testing facilities. [1, 45]. To filter out these undesired interferences, so-called deconvolution filters were used. An introduction on deconvolution filtering is given in [53]. Deconvolution is the inverse process of convolution, where the response of a system, when subjected to an input, is obtained. This system can be a linear or non-linear set of equations. The process of deconvolution then gives the input, using the known sys-

tem and the response. If the measurement setup can be described by a linear system, and knowledge of the response of the linear system is available, the input to the system can be calculated from the output. Although the description is short, this is not a trivial process.

Types of deconvolution for the same problem were investigated in [1], with a similarly good introduction in [53]. The general convolution- and deconvolution, in frequency domain, is shown in Equation 2.12, where $Y(j\omega)$ is the output signal, $H(j\omega)$ the system, and $X(j\omega)$ the input signal. Usually the deconvolution process is done in the frequency domain as convolution and deconvolution are multiplication and division operations in the frequency domain while the deconvolution has no mathematical operator in the time domain.

$$\begin{gathered} \textit{Convolution} \\ Y(j\omega) = X(j\omega) \cdot H(j\omega) \\ \textit{Deconvolution} \\ X(j\omega) = Y(j\omega)/H(j\omega) \end{gathered} \tag{2.12}$$

However, in the real world, the convolution and deconvolution processes are contaminated with measurement and modelling errors.

$$\begin{gathered} Y_m(j\omega) = Y(j\omega) + Y_e(j\omega) \\ H_m(j\omega) = H(j\omega) + H_e(j\omega) \\ \textit{With:} \\ Y_m(j\omega),\, H_m(j\omega) = \textit{measured components} \\ Y_e(j\omega),\, H_e(j\omega) = \textit{error components} \end{gathered} \tag{2.13}$$

$$X(j\omega) = \frac{Y_m(j\omega) - Y_e(j\omega)}{H_m(j\omega) - H_e(j\omega)} \tag{2.14}$$

Filling in the deconvolution equation as such, it is obvious that problems appear for frequency regions where the magnitude of the measured signal is as large as the error in the system identification. This is a problem very difficult to circumvent, because it is unlikely that $H_e(j\omega)$ is smaller than $H_m(j\omega)$, where $H_m(j\omega)$ is small. This division leads to large errors for small changes in the signal. A solution to this problem is usually a bandpass filter which dampens the fluctuations for regions where the real signal $H(j\omega)$ is expected to be small. However, this usually requires experience and knowledge with the problem to be solved, which may not be available.

In [1], different types deconvolution filters were investigated. The filter types were Infinite Impulse Response (IIR) filter and the Finite Impulse Response (FIR) filter, and the Kalman filter. In this sense, the filter type is the mathematical representation of the test rig. An Infinite Impulse Response filter is a mathematical model that takes a linear combination of the previous input- and output samples to create a new output. The IIR filter thus incorporates a feedback loop which requires care in designing the filter as the feedback loop can create unstable behaviour. The response of even a stable IIR filter to an impulse input does not damp out to zero, from which the name is derived. In contrast, the response of an FIR filter does. The output of an FIR filter is a weighted sum of the last input samples, meaning there is no feedback loop, and instability is not an issue. The output of an FIR filter will damp out to zero after an arbitrary amount of time. In general, any FIR filter can be approximated by an IIR filter, and vice versa. IIR and FIR filter design was demonstrated in [1]. The process was described as ”time-consuming and require a secure foundation in DSP”. The advantages and disadvantages of both the IIR- and FIR filter design were described as ”rather well balanced”, with the application determining which filter was preferable.

The rocket test stand in [1] is modeled as an Auto Regressive Moving Average (ARMA) process. This model type is described as appropriate as the complete system output is a function of a series of random shocks (MA part) and the behaviour of the model itself (AR part). This model was therefore considered appropriate for the thrust stand under consideration. This reasoning also holds for a typical flapping wing test setup, although the involved frequencies are much lower (in the order of 10 Hz compared to mentioned impulse widths of 10 ms, or 100 Hz. As the ARMA model can be described in a similar way to the IIR filter, the IIR filter was deemed the most suitable for the thrust stand problem.

A third filter type was discussed, the Kalman filter. This filter also uses feedback and IIR coefficients, but works by calculating an optimal estimation by taking into account measurement and process noise statistics. This makes the Kalman filter inherently stable. The Kalman filter is also simple to implement. The downside is that the mentioned statistics need to be provided by the user. However, obtaining these covariance matrices was later shown to be possible using a heuristic process.

The Kalman filter for deconvolution was used as explained in Bora et al. [10]. First, it was checked if the model simulating the transient response of the thrust stand matched the real performance. For this, the simulated response was subtracted from the real response. The noise in the resulting signal should then ideally by white Gaussian. After investigation, this was found to be not the case as the thrust stand was too complex to model using a transfer function. This would lead to the Kalman filter not showing optimal results. However, it was found that the other deconvolution filters offered worse performance than deconvolution using the Kalman Filter. The performance differences were found at the flanks of amplitude rises and in the magnitude of the steady-state error. The observed downsides were a higher computational effort and the need to provide process statistics by way of covariance matrices. It was found that a heuristic estimation of the covariance matrices usually offers acceptable performance. In absolute terms, the computational effort for a typical robotic flapper experiment is expected to be in the order of seconds, and the computations can be done off-line.

2.7. Conclusion

In this literature review, the current state of the art in flapping wing research is evaluated and discussed. It is found that there exists a possibility for exploration for revolving-pitching wing measurements, as current data on the forces generated by the pitching motion and the influence of kinematics on the generated force is limited. It is found that typical robotic flapper setups to investigate flapping wing flight have shortcomings as the fluid-dynamic forces on the test stand will induce vibrations in the test setup. These vibrations are picked up by the force sensors, which obscures the fluid-dynamic force of interest. The current filtering method is shown to be not able to adequately cope with this problem for impulsive changes in force generation, leading to potential loss of information, or even misinformation. As both the revolving-surging and revolving-pitching kinematic generate such impulsive forces, a better filtering method is needed to take into account the structure of the test setup. It is not adviseable to change the physical structure of the test setup, as changing the test setup to limit the vibrations can lead to loss of flow similarity over the wing. Computing the test stand response and subtracting that from the measured response can be performed using deconvolution. To perform this deconvolution, the Kalman filter for deconvolution (DK filter) is selected. In contrast to other deconvolution filters, there is access to detailed previous work on the use and implementation of the filter, wherein the DK filter was shown to work well for a similar problem, and it was considered easy to implement without a secure foundation in signal processing. It is therefore concluded that the DK filter is the best candidate to improve the measurement results for a typical robotic flapper.

The goal of this thesis is therefore twofold. 1) implement and validate the Kalman deconvolution filter for the revolving wing measurement setup. 2) perform a parametric investigation in terms of kinematics for a revolving-surging and revolving-pitching wing motion.

3

Experimental setup and methods

3.1. Experimental Setup

In this chapter the experimental setup, processing and experiments done are discussed.

3.1.1. Measurement Equipment

The experiments were done at Aerodynamics Laboratory of Delft University of Technology. The setup consisted of a plexiglass octogonal water tank, 60 cm in diameter and approx 60 cm high. In the water tank, a wing was suspended. A large part of this experimental setup was also used by Perçin and van Oudheusden in [49]. A photo of this setup is shown in Figure 3.1. The wing revolving motion was controlled with a geared servo motor above the water line, the wing pitching was controlled with a submersible servo motor in line with the pitching axis. This motor was mounted in an enclosure that also housed the force sensor. The wing rotation and wing pitching motors were controlled with a Maxon motor controller via an in-house code developed in LabVIEW. The motor above the waterline controlling the revolving rotation had a positional resolution of $24 \times 10^{-6} rad$ and could accelerate the wing at up to $48 rad/s^2$. The motor was equipped with a feedback loop and the accuracy of the wing position and velocity was $8 \times 10^{-3} rad$ and $2 \times 10^{-2} rad/s$ respectively. The pitching rotation could be controlled up to $17 \times 10^{-3} rad$. This motor did not offer position feedback. The forces on the wing in Fx, Fy, and Fz direction and moments in Tx, Ty, and Tz direction were measured using the water-submersible ATI Nano17\IP68 force sensor [4]. The force sensor was mounted at the root of the wing. The specifications of the sensor are shown in Table 3.1.

Table 3.1: ATI Nano 17 sensing range and typical resolution via [4]

Sensing range			Resolution	
Fx,Fy (N)	Fz (N)	Tx,Ty, Tz (Nmm)	Fx,Fy, Fz (N)	Tx,Ty,Tz (Nmm)
12	17	120	1/320	1/64

3.2. Wing geometry and motion kinematics

3.2.1. Wing geometry

The wing sizing process depended on multiple design factors as listed below:

- The wing aspect ratio should be in the range of related experiments and similar to that of actual insects [14, 60]
- The wing should be also mounted and moved in such a way that the Rossby number is in the range of insect flight as described in [40].
- The Reynolds number should be such that it is in the range of insect flight [60].

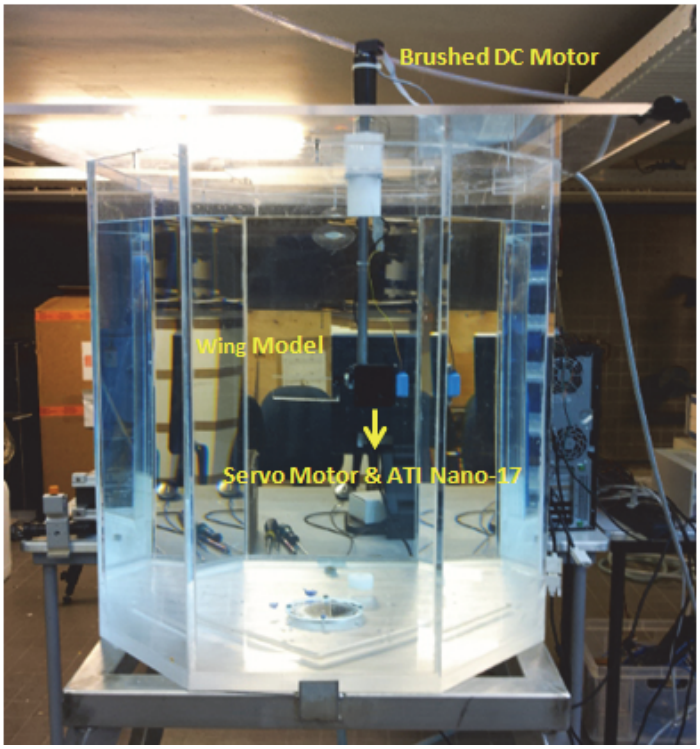

Figure 3.1: Photo of experimental setup, adapted from [52]

- The wing tip needs to stay at least 5 chord lengths away from the walls to minimize wall influence. [44].
- The wing planform shape should be rectangular so that the computation of wing parameters, such as the aspect ratio, span, and chord are as independent as possible of averaging convention.
- The wing forces should be high enough to have sufficient dynamic range at the given resolution of the force sensor. [4]. These forces were predicted using the quasi-steady model from [58].
- The working fluid in the water tank is restricted to pure water. This facilitates cleaning, and makes it feasible to empty the tank daily, which obviates the need for chemicals inhibiting algae growth.

Balancing these needs, using the invaluable experience with the setup of M. Perçin and B. van Oudheusden, the wing sizing as given in Figure 3.2 was determined as in Table 3.2. This wing is used for all the motions as discussed in the next section.

Table 3.2: Wing size from Figure 3.2

Parameter	size(mm)
Root Radius	27.7
Chord	50
Span	100
Wing thickness	3

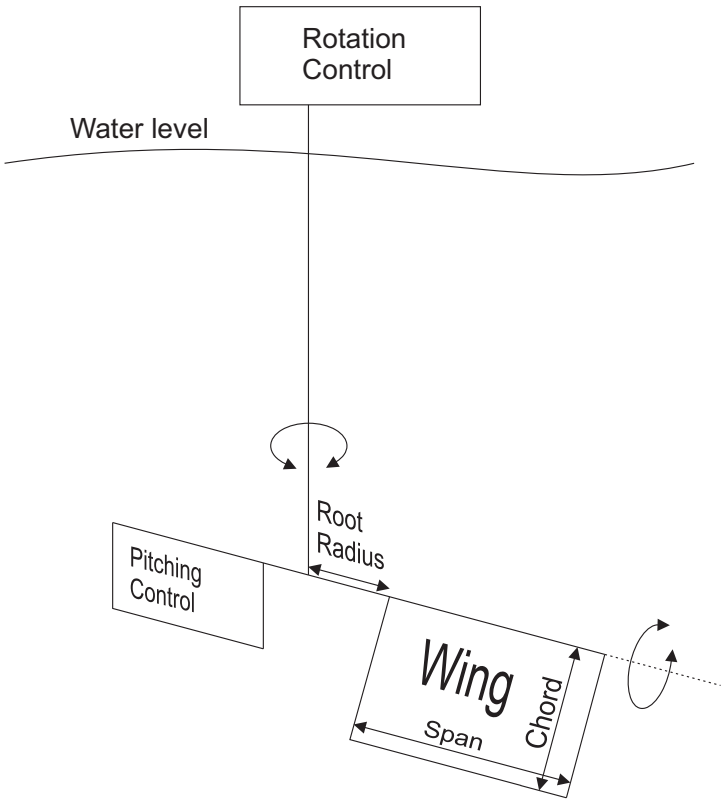

Figure 3.2: Sketch of experimental setup

3.2.2. Motion

As discussed in Chapter 2 revolving-surging and revolving-pitching motions are investigated in this report.
The varying parameter for the revolving-surging motion is the geometric angle of attack (α).
The data from the revolving-surging experiments is used for three goals. The first is the implementation and validation of the DK filter, the revolving-surging measurements are used as there is more previous work investigating this type of motion, to which the results in the current investigation can be compared to. Also, the expected unsteady force generation is less complex, as less of the unsteady force generation mechanisms (as discussed in Chapter 2.4) will be excited. The second goal is to obtain a value for F_{steady} in the quasi-steady model as discussed in Chapter 2.5.1, for the entire range of α, to be able to use the quasi-steady model for the revolving-pitching experiments. Lastly, the initial acceleration of the revolving-surging motion will excite structural vibrations in the test rig, which, as demonstrated in Chapter 2, can lead to erroneous results if filtered conventionally. Filtering this phase with the DK filter is expected to give more accurate force measurements.
The varying parameters for the revolving-pitching motion are the pitching rate ($\dot{\alpha}$) and the pitch axis location. At the start and end of the pitching motion, pitching accelerations are present which can lead to erroneous force measurements if filtered conventionally (as demonstrated in Chapter 2).

Surging kinematics

To satisfy the need for a value of F_{steady}, and to investigate the differences in force generation, the surging measurements are performed at a large range of angles of attack to form a complete polar.

The wing is accelerated to a Reynolds number of 1×10^4 at 75 % span, over one chord length of travel. Taking this Reynolds number at 75 % span ($Re_{0.75}$) as representative for the wing follows the convention of recent papers investigating revolving wing aerodynamics. [29], [44] [62]. This translates to a rotational acceleration of 3.89 rad/s^2 and a maximum rotational velocity of 1.95 rad/s, or 0.2 m/s at the 75% chord point. The wingtip-radius Rossby number was 2.45, the Rossby number at the radius of gyration was 1.66. [41]. After 13 chords travelled, or slightly more than one revolution, the revolving

motion was stopped.

The angles of attack tested are shown in Table 3.3.

Table 3.3: Revolving-surging experimental space

Angles of attack tested (°)												
8	13	18	23	28	38	45	49	59	70	80	90	110

Pitching kinematics

The pitching kinematics involve first accelerating the wing to a certain rotational velocity, and then rotating the wing to a certain angle of attack in a given time. As also shown in Chapter 2, there is little literature on measurements on revolving-pitching wings, but ample literature on translating pitching wings [25, 67]. Therefore, the experiment was designed to obtain information on a large range of pitching rates and pitching locations. The starting angle of attack was zero degrees, the final angle of attack was 45 degrees. Holes were drilled at the root along the chord of the wing to change the point where the wing was attached to the pitching motor, and hence what the pitching axis location was. The non-used holes were taped shut. For clarity, a sketch of the wing planform used is found in Figure 3.3)

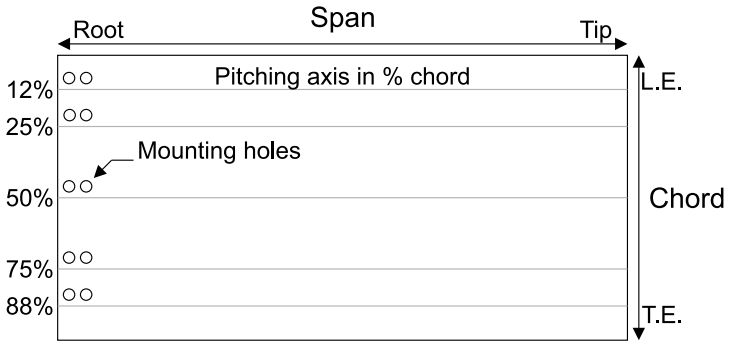

Figure 3.3: Sketch of wing planform, showing the mounting holes to scale, the locations of the tested values of x_0, the leading edge (L.E.) and trailing edge (T.E.)

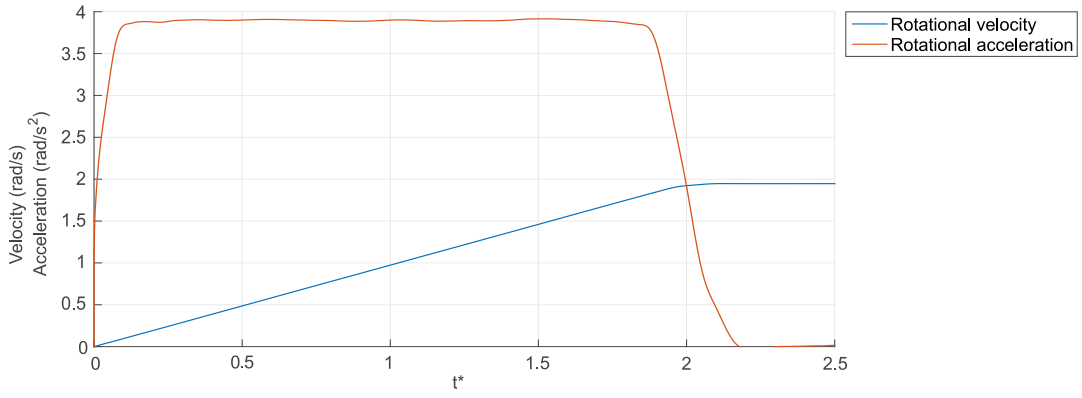

Figure 3.4: Surging kinematics in terms of rotational acceleration and velocity

The acceleration profiles were determined in terms of chord lengths at 75% span, much like the surging experiments. While at 0 degree angle of attack, the wing was accelerated to the same velocity as used in the surging experiments, $\dot{\phi}$ =1.95 rad/s, $V_{0.75}$ = 0.2 m/s. Note that $\dot{\phi}$ is equivalent to Ω for $\dot{\alpha}$ = 0 and $\dot{\theta}$ = 0.

The experimental space spanned was along the pitching location axis and the pitching rate. These are also the pitching-related variables in the quasi-steady theory from [58]. The rationale between choosing the pitching axis locations was influenced by the notion from the quasi-steady theory that the

pitching motion increases lift proportionally to the distance from the 75% chord axis. The other pitching axis locations were chosen at regular intervals from that chordwise position, with the mounting system such that the wing could not be mounted closer than 12% chord from either the leading or trailing edge. The tested values of $\hat{x}_0 = x_0/c$ were 0.12, 0.25, 0.5, 0.75, and 0.88.

The pitching rates were chosen in accordance to the observations in [60] from which the reduced pitching rates of the observed animals can be computed. These are shown in Table 3.5. Another source instrumental in determining the pitching rates to test was [25], where meaningful lift augmentation was found only for reduced pitch rates higher than k = 0.05. The pitch rates of π, $\pi/2$, $\pi/3$, and $\pi/4$ were chosen to be tested. The corresponding reduced pitch rate and chords travelled are given in Table 3.4. The velocities and rotational acceleration of all the different motions are shown in Figure 3.5.

In conclusion, 20 revolving-pitching experiments were performed, at five different pitching axis positions and four different pitching rates.

Table 3.4: Pitch rates in different formats

Pitch rate				
Pitch rate (rad/s)	π	$\pi/2$	$\pi/3$	$\pi/4$
Reduced pitch rate at 75% span (k)	0.39	0.20	0.13	0.10
Chords travelled at 75% span at $\dot{\phi}_{max}$	1	2	3	4

Table 3.5: Reduced pitching rates for animals, computed using data from Table 2 and the motion graphs from Fig. 2 from [60]

Animal	pitching angle (deg)	Main pitching phase length in % of total motion	mean chord (mm)	flap amplitude (rad)	75% of mean wing tip velocity	Reduced pitching rate k
Hawkmoth	45	29	18.30	2.00	3.78	0.34
Honeybee	64	35	3.00	1.59	5.54	0.40
Hummingbird	75	32	12.00	2.02	6.50	0.31

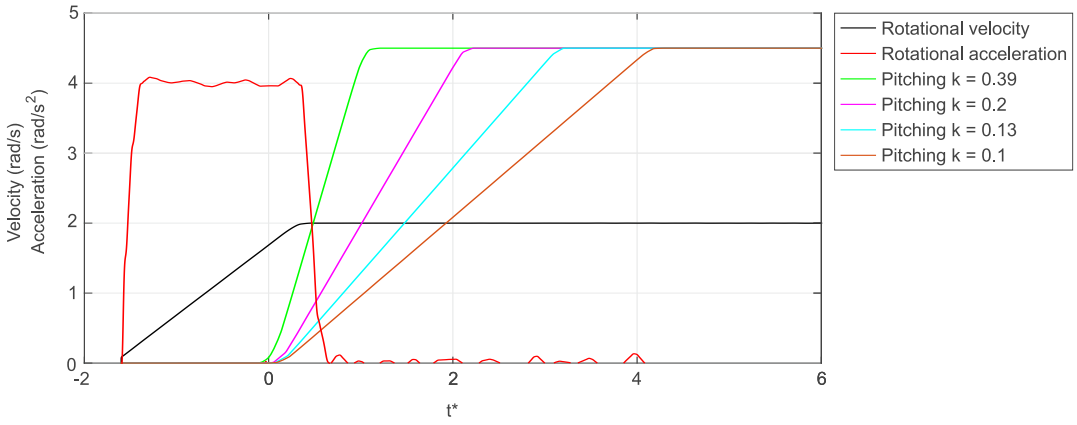

Figure 3.5: Pitching kinematics in terms of rotational acceleration, rotational velocity, and pitching velocity, for all 4 different pitching velocities

3.3. Data Processing

3.3.1. Force

The obtained force data consisted of the forces in X, Y and Z direction, and moments in Mx, My, and Mz direction, obtained at 2 kHz. To facilitate data processing, a static measurement before the real measurement was performed to obtain 'zero fluid-dynamic force' voltages, consisting only of gravitational and buoyancy forces. For the revolving-pitching measurements, a set of static measurements were performed to obtain a function which predicts the change in gravitational forces during the pitching motion.

The position data was obtained in terms of pitch angle, angular position and angular velocity. This data was obtained at 33 Hz .

Each experiment was repeated 20 times on the same day, with the 23, 28, and 45 degree surging experiments were repeated 20 times on two separate days. The results of these double experiments were averaged after processing.

The force data is filtered before ensemble averaging. The data is first denoised with a 50 Hz cut-off Chebyshev type II low-pass filter, and subsequently, the data is DK filtered. The denoising and DK filtering steps are explained in Chapter 4. The 50 Hz low-pass filtered data is checked for outliers, where an outlier was defined as a measurement run containing more than 1% of samples deviated more than 30% of the maximum value from the average value.

To accurately match the data and get rid of any lag in the data or any time shifts induced by the 50 Hz low-pass filtering, the 50 Hz filtered data is used to match the repetitions in time by matching up the deceleration peak from stopping the motion. The matched data is shown in Figure 3.6(A), together with a closer look at the matched data around 2 t*(B), where the acceleration part of the motion stops. The deceleration peak is seen prominently at 14 t*.

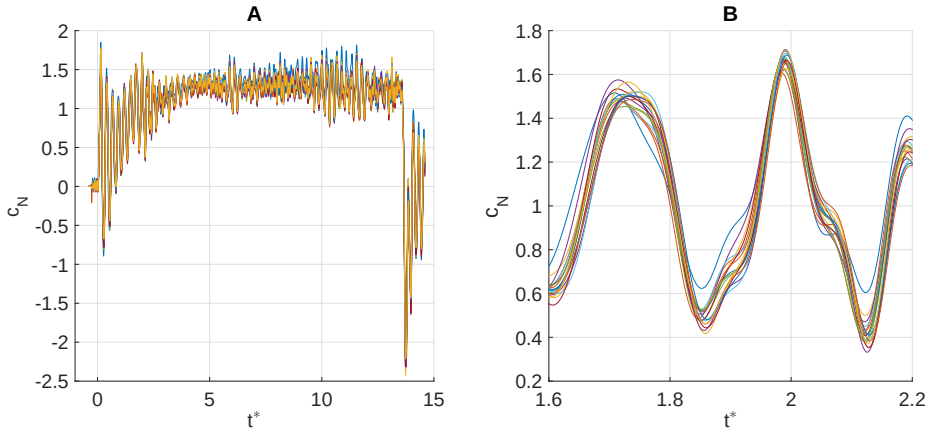

Figure 3.6: Coherence of force histories, all repetitions shown for the 45 degree revolving-surging experiment

The effectiveness of the averaging effect is shown by assuming the 20 measurements cover the entire range of possible physical values, and randomly generating a large amount of ensemble averaged measurements from this dataset. Of this large amount of datapoints, the 5th and 95th percentile in magnitude are plotted in Figure 3.8. This gives the assumed 2 standard deviations, or 95% confidence interval for the amount of repetitions shown. Figure 3.7 shows the width of the 95% confidence interval for terms of c_N, c_M, and c_T, of the DK filtered $45\,°\alpha$ revolving-surging experiment. The width of the confidence interval is given in percent of the maximum value. It is observed that there is little improvement obtained by going from 10 repetitions to 20.

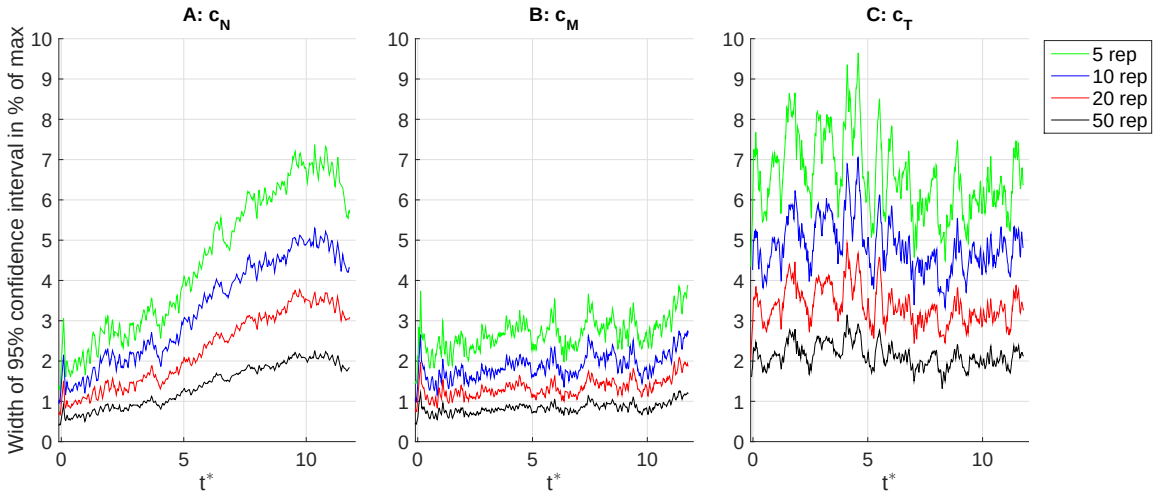

Figure 3.7: 95% confidence interval width for c_N (A), c_M (B) and c_T, (C), in percentage of the maximum value.

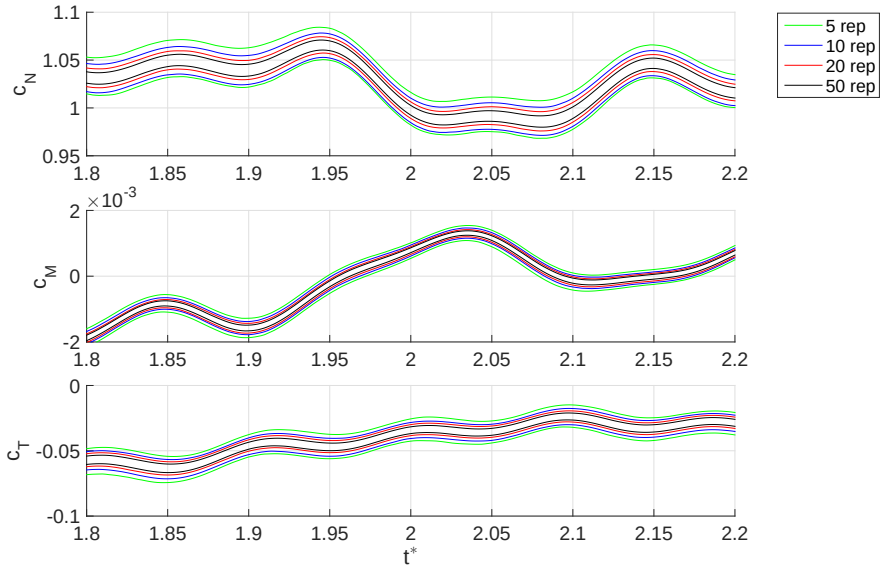

Figure 3.8: Visualized confidence interval

The Y and X force are nondimensionalized to c_N and c_T as discussed in chapter 2. The reference velocity is the terminal tangential velocity at 75% of the span. The pitching moment coefficient c_M was computed around the computed chordwise center of pressure at the constant-velocity part of the motion, as the canonical quarter chord point is only valid for thin airfoils at a low angles of attack. To convert to root-relative force coefficients as in [5], the coefficients obtained at 75% span need to be divided by 0.65. Note that the root-relative force coefficient is the same as normalizing the generated force at the radius of gyration reference position. Both methods end up at Equation 3.1

$$C_{\text{force}} = \frac{6 \times \text{force}}{\rho c \dot{\phi}^2 (r_{tip}^3 - r_{root}^3)} \tag{3.1}$$

3.3.2. Motion and force matching

Just as the force histories needed to be accurately matched to each other, the force histories need to be time-matched to the position data. The motion data acquisition frequency is 33 Hz, and the force data acquisition occurs at 2 kHz. Therefore, the time-resolution of the force data is much higher. To obtain accurate timing, the position data was interpolated and instead of looking at the position data to find the motion start, the first force peaks were used to find the start of the motion. For the revolving-surging experiments, the first force peak of interest was the moment on the force sensor caused by the tangential force, as the location of this moment peak is related to accelerating the wing from rest, and therefore the reaction of the fluid force in terms of moment is expected to coincide with any displacement of the wing. The non-ambiguity of the start point location determination is illustrated with the pitching moment for the 45 degree revolving surging experiment in Figure 3.9

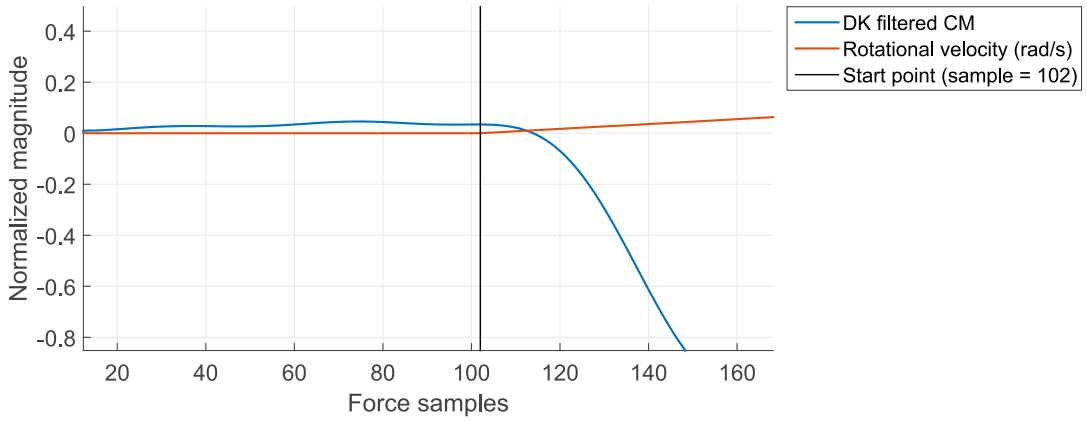

Figure 3.9: Determination of starting point of revolving-surging motion illustrated with the 45 degree angle of attack experiment

For the revolving-pitching experiments, the motion was matched to the force data on where the wing starts to pitch, as the control over the timing of the pitching motor was considered less accurate than that of the revolving motor, as the pitching motor control did not include feedback. As in the surging experiments the motion control sampling output was 33 Hz. However, this data only included the input to the pitching motor, and not the actual position. To deal with this timing problem, any lag between input to the pitching motor and actual pitching rotation was considered constant and the moment data was inspected for a prominent decrease in moment coefficient which indicates a pitch-up moment. This way, the motion data was matched to the force data. This is visualised in Figure 3.10.

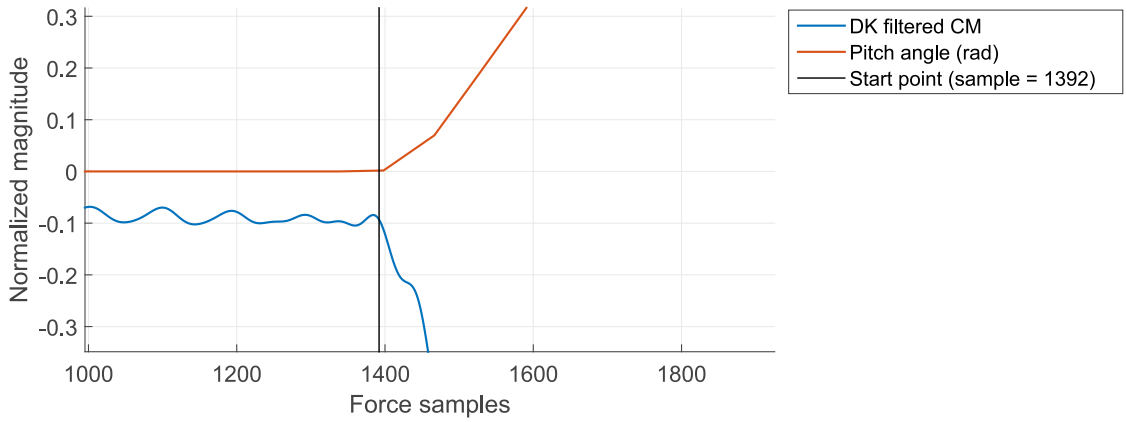

Figure 3.10: Determination of starting point of revolving-pitching motion illustrated with k = 0.39 and pitching axis location at half chord.

4

Kalman Deconvolution filter setup and implementation

4.1. Kalman deconvolution

The test setup is expected to induce vibrations in the measurements, as the setup is very similar to the one used in [49]. The force results of those measurements required a 15 Hz low-pass filter to remove most of the mechanical vibrations, which was demonstrated in Chapter 2 to have a chance of also interfering with the force signal. As discussed, to deal with this problem, the Deconvolution Kalman filter will be used and investigated in this thesis.

4.1.1. The Kalman Filter

The Kalman filter is the well-known optimal filter to remove Gaussian white noise with a zero mean. To explain the Kalman filter, the derivation is given here. The derivation and presentation structure is similar to the original paper [31] and [26].

The goal of the Kalman filter is to obtain an optimal estimation for the system state ***x**(k)* from a measured output ***y**(k)*, shown in Figure 4.1. This diagram consists of two parts, ”Process” and ”Measurement”. The Process part represents the physical process of interest and noise sources therein, the Measurement part represents the noise contribution of the measurement apparatus. This is explained in detail in the rest of the chapter.

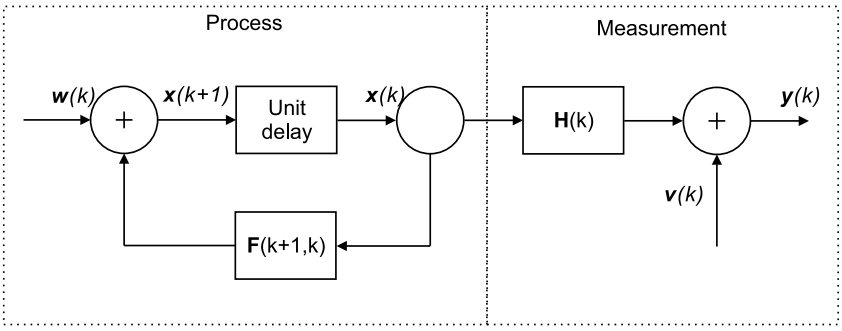

Figure 4.1: Process-measurement flow diagram

The process equation consists of updating the process state based on the previous state. This is performed by the transition matrix which represents the transition from the state at time k to the state at time $k+1$. $u(t)$ is a white gaussian random noise source, designated 'process noise'. The unit delay represents the recently computed state with added noise at $k+1$ becoming the state at time k and as such completes the loop. The shown process is only dependent on random inputs.

The process equation is shown in Equation 4.1, the process noise covariance matrix is given in Equation 4.2.

$$\mathbf{x}_{k+1} = \mathbf{F}_{k+1,k}\mathbf{x}_k + \mathbf{w}_k \tag{4.1}$$

$$E\left[\mathbf{w}_n\mathbf{w}_k^T\right] = \begin{cases}\mathbf{Q}_k & \text{for } n = k \\ \mathbf{0} & \text{for } n \neq k\end{cases} \tag{4.2}$$

Equation 4.3, the measurement equation is similar to the process equation, although it lacks the iterative loop. The output of the process equation is transformed by the measurement matrix $\mathbf{H}_k$ and the measurement noise $\mathbf{v}_k$ is added. The measurement noise is defined by the measurement noise covariance matrix, shown in Equation 4.4 and is is equal to the process noise covariance matrix, but controlled by the parameter $\mathbf{R}$ instead of $\mathbf{Q}$. As with the process noise, this noise is additive, has a zero-mean and is of white-Gaussian nature. The ability of the Kalman filter to remove noise in real-life depends in part on the validity of these assumptions.

$$\mathbf{x}_{k+1} = \mathbf{F}_{k+1,k}\mathbf{x}_k + \mathbf{w}_k \tag{4.3}$$

$$E\left[\mathbf{w}_n\mathbf{w}_k^T\right] = \begin{cases}\mathbf{R}_k & \text{for } n = k \\ \mathbf{0} & \text{for } n \neq k\end{cases} \tag{4.4}$$

The goal of the Kalman filter is to estimate the state of $\mathbf{x}$ for all $k \geq 1$ from the observed data $\mathbf{y}$. The goodness or optimality of the estimation of $\mathbf{x}$ called $\hat{\mathbf{x}}$ is determined by assigning a cost to the error. This cost function J needs to be chosen such that it is non-decreasing and positive for the estimation error $\tilde{x}_k$.

$$\tilde{x}_k = (\mathbf{x}_k - \hat{\mathbf{x}}_k). \tag{4.5}$$

The Kalman filter is set up in such a way that the average cost, shown in Equation 4.6 is minimized. Do note that the notation has been changed from vector to scalar random variables. This has been done for readability and does not limit the theory.

$$E\left\{J\left[x_k\left(t_k\right) - \hat{x}_k\left(t_k\right)\right]\right\} = E\left[E\left\{J\left[x_k\left(t_k\right) - \hat{x}_k\left(t_k\right)\right]|y_1, \ldots, y_k\right\}\right] \tag{4.6}$$

To find the optimal estimate which minimizes the average cost function two theorems are invoked.

Theorem 1

If the cost function is the mean-square of the error, or $J(\tilde{x}) = (\tilde{x})^2$, and the processes $\{x_k\}$ and $\{y_k\}$ are Gaussian, then the random variable $\hat{x}_k$ which minimizes the average cost is the conditional expectation, given in Equation 4.7. Proof and more elaborate explanation of this theorem can be found in [31] and references therein.

$$\hat{x}_k = E\left[x_k(t_k)|y_1, \ldots, y_k\right] \tag{4.7}$$

Theorem 2

Let $\{x_k\}$ and $\{y_k\}$ be random processes with zero mean. Observed are $y_1, \ldots, y_k$. If either

- (A) the random processes $\{x_k\}$ and $\{y_k\}$ are Gaussian or;
- (B) the optimal estimate is restricted to be a linear function of the observed values and the cost function is the mean-square error;

Then, with the vector space Y_k, formed by the set of linear combinations of observed random variables:

$$\sum_{i=1}^{k} a_i y_i \tag{4.8}$$

$$\hat{x}_k = \textit{orthogonal projection of } x_k \textit{ on } Y_k = \bar{x}(k|k) = \hat{E}\left[x_k|Y_k\right] \tag{4.9}$$

With the optimum estimator defined, the Kalman Filter can be derived.

Suppose there exists an ‘a priori’, or ‘beforehand’ estimate for x at time k, $\hat{x}_k^-$ and that the ‘new knowledge’ of the measured value y at time k is to be used to update the a priori estimate. Since the

estimation is set up to be linear, the 'a posteriori' or 'afterwards' estimate $\hat{x}_k$ is a linear combination of the a priori estimate and the measured value, shown in Equation 4.10.

$$\hat{x}_k = \mathbf{G}_k^{(1)}\hat{x}_k^- + \mathbf{G}_k y_k \tag{4.10}$$

The matrices $\mathbf{G}_k^{(1)}$ and $\mathbf{G}_k$ need to be found. Theorem 2 is invoked, where the expected error and the observed values are Gaussian and uncorrelated, meaning they are orthogonal to each other.

$$E\left[\tilde{x}_k y_i^T\right] = 0 \text{ for } i = 1, 2, \ldots, k-1 \tag{4.11}$$

Filling in Equation 4.11 with previous equations 4.10, 4.3, and 4.5

$$E\left[(x_k - \mathbf{G}_k^{(1)}\hat{x}_k^- - \mathbf{G}_k\mathbf{H}_k x_k - \mathbf{G}_k w_k) y_i^T\right] = 0 \text{ for } i = 1, 2, \ldots, k-1 \tag{4.12}$$

Using orthogonality relations similar to 4.11

$$E\left[w_k y_i^T\right] = 0 \text{ for } i = 1, 2, \ldots, k-1 \tag{4.13}$$

$$E\left[(x_k - \hat{x}_k^-) y_i^T\right] = 0 \text{ for } i = 1, 2, \ldots, k-1 \tag{4.14}$$

Equation 4.12 is rewritten to

$$(\mathbf{I} - \mathbf{G}_k\mathbf{H}_k - \mathbf{G}_k^{(1)}) E\left[x_k y_i^T\right] = 0 \text{ for } i = 1, 2, \ldots, k-1 \tag{4.15}$$

This equation is in general true if the first part of the left hand side is zero, or

$$\mathbf{G}_k^{(1)} = \mathbf{I} - \mathbf{G}_k\mathbf{H}_k \tag{4.16}$$

Substitute this into Equation 4.10

$$\hat{x}_k = \hat{x}_k^- + \mathbf{G}_k(y_k - \mathbf{H}_k\hat{x}k^-) \tag{4.17}$$

Where $\mathbf{G}_k$ is called the *Kalman gain* in later discussions on the Kalman filter. Where the previous equations from 4.11 to 4.14 looked at the state estimation part to obtain relations for the Kalman gain, now the measurement part of the state space relations is used to obtain new relations to obtain the closed form for the Kalman gain.

First, the innovation $\tilde{y}$ is defined, giving a notion of new information imparted by each new measurement. The new measurement y_k is compared to the expected value of the new measurement, given all previous measurements, $\hat{y}_k$.

$$\begin{aligned}\tilde{y}_k = y_k - \hat{y}_k &= \mathbf{H}_k x_k + v_k - \mathbf{H}_k\hat{x}_k^- \\ &= \mathbf{H}_k\tilde{x}_k^- + v_k\end{aligned} \tag{4.18}$$

With 4.18 and 4.17 the state estimation error can be rewritten

$$x_k - \hat{x}_k = \tilde{x}_k^- - \mathbf{G}(\mathbf{H}\tilde{x}_k^- + v_k) \tag{4.19}$$

The orthogonality relation

$$E\left[(x_k - \hat{x}_k)\tilde{y}_k^T\right] = 0 \tag{4.20}$$

can be filled in with the rewritten state estimation error.

$$E\left[\left\{(\mathbf{I} - \mathbf{G}_k\mathbf{H}_k)\tilde{x}_k^- - \mathbf{G}_k v_k\right\}(\mathbf{H}_k\tilde{x}_k^- + v_k)\right] = 0 \tag{4.21}$$

Observing that the measurement noise v_k is independent of the a priori state estimation error $\tilde{x}_k^-$, this equation is rewritten such that the measurement noise, Equation 4.4 appears.

$$(\mathbf{I} - \mathbf{G}_k\mathbf{H}_k) E\left[\tilde{x}_k\tilde{x}_k^{T-}\right]\mathbf{H}_k^T - \mathbf{G}_k E\left[v_k v_k^T\right] = 0 \tag{4.22}$$

Rewriting for the Kalman gain

$$\mathbf{G}_k = E\left[\tilde{x}_k^- \tilde{x}_k^{T-}\right]\mathbf{H}_k^T\left[\mathbf{H}_k E\left[\tilde{x}_k \tilde{x}_k^{T-}\right]\mathbf{H}_k^T + \mathbf{R}_k\right]^{-1} \tag{4.23}$$

Now the update relation relating the a posteriori updated estimate $\hat{x}_k$ to the a priori prediction of the estimate $\hat{x}_k^-$ is known

$$\hat{x}_k = \hat{x}_k^- + \mathbf{G}_k(y_k - \mathbf{H}_k\hat{x}_k^-) \tag{4.24}$$

The remaining expectation term in Equation 4.23 can be expanded and is called the a priori covariance matrix
$\mathbf{P}_k^-$

$$\mathbf{P}_k^- = E\left[\tilde{x}_k \tilde{x}_k^{T-}\right] = E\left[(x_k - \hat{x}_k^-)(x_k - \hat{x}_k^-)^T\right] \tag{4.25}$$

As indicated by the $^-$ symbols, this term has an updated counterpart, the a posteriori covariance matrix $\mathbf{P}_k$

$$\mathbf{P}_k = E\left[\tilde{x}_k \tilde{x}_k^T\right] = E\left[(x_k - \hat{x}_k)(x_k - \hat{x}_k)^T\right] \tag{4.26}$$

Substituting Equation 4.21 in the a priori estimation and reformulating using again the independence of v_k from $\tilde{x}_k^-$ and Equation 4.23, the update relation between the a priori and a posteriori covariance matrices is found

$$\mathbf{P}_k = (\mathbf{I} - \mathbf{G}_k\mathbf{H}_k)\mathbf{P}_k^- \tag{4.27}$$

With this equation it is possible to compute the influence of a 'new' measurement or the innovation on the estimation of the covariance matrix. The next step is the prediction of the covariance matrix, or computing the new a priori covariance matrix from the previous a posteriori covariance matrix.

First, the update of of the state estimate is defined from the process equation 4.1

$$\hat{x}_k^- = \mathbf{F}_{k,k-1}\hat{x}_{k-1} \tag{4.28}$$

Rewriting using Equation 4.5

$$\tilde{x}_k^- = \mathbf{F}_{k,k-1}\tilde{x}_{k-1} + w_{k-1} \tag{4.29}$$

When this rewritten a priori state estimation error is filled in in Equation 4.25 and observing that the process noise w_k is independent of $\tilde{x}_{k-1}$, the 'current' a priori covariance matrix can be written as a function of the previous a posteriori covariance matrix and the process noise, from Equation 4.2)

$$\mathbf{P}_k^- = \mathbf{F}_{k,k-1}\mathbf{P}_{k-1}\mathbf{F}_{k,k-1}^T + \mathbf{Q}_k \tag{4.30}$$

As the total derivation is rather long, a summary (adapted from [26]):

Kalman Filter summary

Given the noise driven state space model

$$\begin{aligned}\mathbf{x}_{k+1} &= \mathbf{F}_{k+1,k}\mathbf{x}_k + \mathbf{w}_k,\\ \mathbf{y}_k &= \mathbf{H}_k\mathbf{x}_k + \mathbf{v}_k\end{aligned} \tag{4.31}$$

with $\mathbf{w}_k$ and $\mathbf{v}_k$ zero mean, independent Gaussian noise processes, and with covariance matrices $\mathbf{Q}_k$ and $\mathbf{R}_k$;
The optimal estimation filter consists of 5 steps for each k and is recursively solved.

- *A priori prediction of the state estimate*

$$\hat{\mathbf{x}}_k^- = \mathbf{F}_{k,k-1}\hat{\mathbf{x}}_{k-1} \tag{4.28}$$

  If the process is not purely noise driven, as in the derivation, but there exists a control signal in the process with a separate known input variable $\mathbf{u}_k$ and input matrix $\mathbf{B}$, which is customary in state-space representation, the a priori prediction is slightly different.

$$\hat{\mathbf{x}}_k^- = \mathbf{F}_{k,k-1}\hat{\mathbf{x}}_{k-1}^- + \mathbf{B}\mathbf{u}_k \tag{4.32}$$

- *A priori prediction of the covariance matrix*

$$\mathbf{P}_k^- = \mathbf{F}_{k,k-1}\mathbf{P}_{k-1}\mathbf{F}_{k,k-1}^T + \mathbf{Q}_k \tag{4.30}$$

- *Kalman gain computation*

$$\mathbf{G}_k = \mathbf{P}_k^-\mathbf{H}_k^T\left[\mathbf{H}_k\mathbf{P}_k^-\mathbf{H}_k^T + \mathbf{R}_k\right]^{-1} \tag{4.33}$$

- *a posteriori update of the state estimate*

$$\hat{\mathbf{x}}_k = \hat{\mathbf{x}}_k^- + \mathbf{G}_k(\mathbf{y}_k - \mathbf{H}_k\hat{\mathbf{x}}_k^-) \tag{4.24}$$

- *a posteriori update of the covariance matrix*

$$\mathbf{P}_k = (\mathbf{I} - \mathbf{G}_k\mathbf{H}_k)\mathbf{P}_k^- \tag{4.27}$$

As the filter operates recursively, the initialization state and covariance estimations need to be provided. If no other information is available, suitable initial values are

$$\begin{aligned}\hat{\mathbf{x}}_0 &= E\left[\mathbf{x}_0\right] \\ \mathbf{P}_0 &= E\left[(\mathbf{x}_0 - E\left[\mathbf{x}_0\right])(\mathbf{x}_0 - E\left[\mathbf{x}_0\right])^T\right]\end{aligned} \tag{4.34}$$

4.1.2. Kalman Deconvolution

In this thesis, the Kalman filter as explained above is used for deconvolution. This was proposed by Bora et al [10]. In the paper by Bora et al., a random signal convoluted with an ARMA process (G(z)) and an LTI process (F(z)), was subsequently deconvoluted using the described Kalman filter and an augmented state-space system consisting of a combination of the state-space representation parameters of both $G(z)$ and the $F(z)$. The process is shown in block-form in Figure 4.2

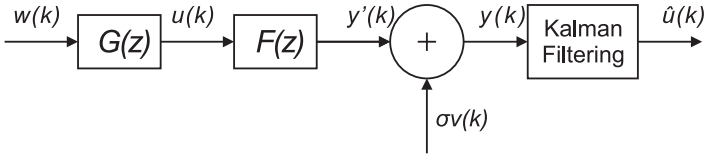

Figure 4.2: Block diagram of the process demonstrated in the paper by Bora et al. [10]

The method as described in [10] is used by Ahlfeld [1] to deconvolute the measured rocket thrust pulses, convoluted with the mechanical vibrational dynamics of the thrust stand to which the rocket was mounted. In this application, the ARMA-process state-space equations were replaced with a built-in low-pass filter or integrator. This was possible as the parameters of the low-pass filter or ARMA-process are only used in estimating the process input, which for the physical experiments is already known and therefore not a goal to obtain. In this sense, the low-pass filter acts as a stabilization, dampening out high-frequency fluctuations in the estimated input to the LTI process. The integrator also acts as a stabilization, but in the way of suppressing steady-state errors. The low-pass filter could conceivably be used to integrate low-pass filtering as a separate signal-processing step in the deconvolution filter. However, as conventional low-pass filtering is simple to do outside the deconvolution Kalman filter, and the built-in low-pass filter works counterintuitively [1], this option will not be explored, and the ARMA process will be represented by an integrator.

In [10], the process F(z) and G(z) are represented as discrete state-space models. The states of both state-space models are combined into a single state, and the state-space matrices of both models are combined as well, giving a single augmented state-space model. Using this augmented state-space model, the Kalman filter can estimate not just the signal without noise, but also without the influence of the system F(z). How this works is clear by inspection from the augmentation and the Kalman filter steps. The augmentation itself is straightforward and will be explained using an example, incorporating the derivation of a state-space model for a mass-spring-damper system, giving physical significance to the augmentation process.

System F(z)

In this thesis, the system F(z) from Figure 4.2 will represent the mechanical vibrations corrupting the signal. F(z) is derived for a single spring-mass-damper system, however in reality this system can be more complex. The state-space model for F(z) is derived from the second order differential equation describing the motion of a spring-mass-damper system (Equation 4.35). The conversion from these equations to both state-space and a transfer function can be found in many books covering engineering vibrations, such as [27]. It must be noted that the derivation is given for the continuous time domain, and not for the discrete time domain as is used in the rest of this chapter. The conversion from continuous time to discrete time is not discussed here. This subject can be explored in various textbooks discussing linear modelling.

$$\begin{gathered} L = \textit{position} \\ m = \textit{mass} \\ c = \textit{damping coefficient} \\ n = \textit{spring constant} \\ u = \textit{force input} \\ m\ddot{L}(t) + c\dot{L}(t) + kL(t) = u(t) \end{gathered} \tag{4.35}$$

In the rest of the equations, the suffix $_f$ is added to denote that they are part of the state-space representation of system F.

This second order differential equation is rewritten as a set of two first order differential equations by defining two new variables $L_1 = L$ and $L_2 = \dot{L}$ followed by division and differentiation.

$$\begin{gathered} \dot{L}_1(t) = L_2(t) \\ \dot{L}_2(t) = -2\zeta\omega_n L_2(t) - \omega_n^2 L_1(t) + u(t)/m \\ \text{With:} \\ \zeta = c/(2m\omega_n) = \textit{damping ratio} \\ \omega_n = \sqrt{n/m} = \textit{undamped natural frequency} \end{gathered} \tag{4.36}$$

The state-space representation is

$$\begin{gathered} \dot{\mathbf{L}}_f = A_f\mathbf{L} + B_f\mathbf{u} \\ \text{With:} \\ \mathbf{L} = \begin{bmatrix} L_1 \\ L_2 \end{bmatrix} \\ A_f = \begin{bmatrix} 0 & 1 \\ -2\zeta\omega_n & -\omega_n^2 m \end{bmatrix} \\ B_f = \begin{bmatrix} 0 \\ 1/m \end{bmatrix} \end{gathered} \tag{4.37}$$

In this example, the output of this system is conveniently defined as the force on the base of the spring-mass-damper.

$$\begin{gathered} \mathbf{y} = C_f\mathbf{L} + D_f\mathbf{u} \\ C_f = \begin{bmatrix} \omega_n^2 & 2\zeta\omega_n \end{bmatrix} \\ D_f = \begin{bmatrix} 0 \end{bmatrix} \end{gathered} \tag{4.38}$$

Where the D matrix is a zero-matrix as there is no direct link between the output of the model and the input of the model. In case there is, the D matrix is non-zero.

A low-pass filter can also be expressed in a state-space equation. The from filter parameters can be found in textbooks concerning signal processing, but will not be part of this thesis. For now, the state-space matrices of a low-pass filter are accepted to be A_g, B_g, C_g, and D_g. The state vector is **z**, the input vector is **w**, and the output vector is **u**.

The A, B, C, and D matrices are combined into an augmented state-space system as described in [10]

$$\mathbf{F}_{k,k-1} = \begin{bmatrix} A_f & B_f & \mathbf{0} & \mathbf{0} \\ \mathbf{0} & \mathbf{0} & C_g & D_g \\ \mathbf{0} & \mathbf{0} & A_g & B_g \\ \mathbf{0} & \mathbf{0} & \mathbf{0} & \mathbf{0} \end{bmatrix}$$
$$\mathbf{B} = \begin{bmatrix} \mathbf{0} \\ \mathbf{0} \\ \mathbf{0} \\ \mathbf{I} \end{bmatrix} \tag{4.39}$$
$$\mathbf{H}_k = \begin{bmatrix} C_f & D_f & \mathbf{0} & \mathbf{0} \end{bmatrix}$$

The state- and input vectors are combined into an augmented state- and input vector

$$\mathbf{x} = \begin{bmatrix} \mathbf{L} & \mathbf{u} & \mathbf{z} & \mathbf{w} \end{bmatrix} \tag{4.40}$$

The size of the zero matrices **0** are found from the context of the other matrices. As can be seen, any input-output transfer or 'feedthrough' is incorporated into the augmented state-space matrices and no separate D matrix is needed. The input of the spring-mass-damper system $\mathbf{y}_f$ is also not present in the B matrix, as it is part of the estimated augmented state vector. This has minor implications on the Kalman filter equations, but not on the actual steps, which are as follows:

- *A priori prediction of the state estimate*

$$\hat{\mathbf{x}}_k^- = \mathbf{F}_{k,k-1}\hat{\mathbf{x}}_{k-1} \tag{4.28}$$

  This is the same equation as for the purely noise driven system without input. Although not noise driven, for the Kalman deconvolution filter, the input is combined into $\mathbf{F}_{k,k-1}$.

- *A priori prediction of the covariance matrix*

$$\mathbf{P}_k^- = \mathbf{F}_{k,k-1}\mathbf{P}_{k-1}\mathbf{F}_{k,k-1}^T + \mathbf{B}\mathbf{Q}_k\mathbf{B}^T \tag{4.41}$$

  This is also slightly different from Equation 4.30, however, the $\mathbf{B}\mathbf{Q}_k\mathbf{B}^T$ part reduces to $\mathbf{Q}_k$ if $\mathbf{Q}_k$ is a number, which it is for 1D signals such as force signals. The other steps are the same.

- *Kalman gain computation*

$$\mathbf{G}_k = \mathbf{P}_k^-\mathbf{H}_k^T\left[\mathbf{H}_k\mathbf{P}_k^-\mathbf{H}_k^T + \mathbf{R}_k\right]^{-1} \tag{4.33}$$

- *a posteriori update of the state estimate*

$$\hat{\mathbf{x}}_k = \hat{\mathbf{x}}_k^- + \mathbf{G}_k(\mathbf{y}_k - \mathbf{H}_k\hat{\mathbf{x}}_k^-) \tag{4.24}$$

- *a posteriori update of the covariance matrix*

$$\mathbf{P}_k = (\mathbf{I} - \mathbf{G}_k\mathbf{H}_k)\mathbf{P}_k^- \tag{4.27}$$

To obtain the estimation for the input force of system $F(z)$, one needs to observe the estimated augmented state vector $\hat{\mathbf{x}}$, and use Equation 4.40 to determine $\hat{\mathbf{u}}$.

4.1.3. Code validation

As a check if the code works, the results of Bora et al. [10] are reproduced. In this paper, system F(z) from Figure 4.2 consists of the state-space matrices A_f, B_f, C_f, and D_f. System G(z) is a 10th order Yule-Walker lowpass filter with a normalized cut-off frequency of $0.5\pi\ rad$/sample. The equations and matrices making up these systems are given in Equation 4.42 and 4.43. Recall Figure 4.2.

$$\mathbf{x}_f(k+1) = A_f\mathbf{x}_f(t) + B_f\mathbf{u}(k)$$
$$\mathbf{y}'(k) = C_f\mathbf{x}_f(k) + D_f\mathbf{u}(k)$$

With:

$$A_f = \begin{bmatrix} 0 & 1 & 0 & 0 \\ 0 & 0 & 1 & 0 \\ 0 & 0 & 0 & 1 \\ -0.0032 & 0.0309 & -0.3297 & 0.6855 \end{bmatrix} \tag{4.42}$$

$$B_f = \begin{bmatrix} 0 & 0 & 0 & 1 \end{bmatrix}^T$$

$$C_f = \begin{bmatrix} -0.02739 & 0.1119 & -0.4685 & 0.1935 \end{bmatrix}$$

$$D_f = 0.4652$$

$$\mathbf{x}_g(k+1) = A_g\mathbf{x}_g(k) + B_g\mathbf{w}(k)$$
$$\mathbf{u}(k) = C_g\mathbf{x}_g(k) + D_g\mathbf{w}(k)$$

With:

$$A_g = \begin{bmatrix} 0 & 1 & 0 & 0 & 0 & 0 & 0 & 0 & 0 & 0 \\ 0 & 0 & 1 & 0 & 0 & 0 & 0 & 0 & 0 & 0 \\ 0 & 0 & 0 & 1 & 0 & 0 & 0 & 0 & 0 & 0 \\ 0 & 0 & 0 & 0 & 1 & 0 & 0 & 0 & 0 & 0 \\ 0 & 0 & 0 & 0 & 0 & 1 & 0 & 0 & 0 & 0 \\ 0 & 0 & 0 & 0 & 0 & 0 & 1 & 0 & 0 & 0 \\ 0 & 0 & 0 & 0 & 0 & 0 & 0 & 1 & 0 & 0 \\ 0 & 0 & 0 & 0 & 0 & 0 & 0 & 0 & 1 & 0 \\ 0 & 0 & 0 & 0 & 0 & 0 & 0 & 0 & 0 & 1 \\ -0.003 & -0.03 & -0.14 & -0.43 & -1.08 & -1.86 & -2.80 & -3.09 & -2.90 & -1.76 \end{bmatrix} \tag{4.43}$$

$$B_g = \begin{bmatrix} 0 & 0 & 0 & 0 & 0 & 0 & 0 & 0 & 0 & 1 \end{bmatrix}^T$$

$$C_g = \begin{bmatrix} 0.0098 & 0.0688 & 0.2840 & 0.7282 & 1.3712 & 2.0921 & 2.1327 & 1.3983 & 0.6206 \end{bmatrix}$$

$$D_g = 0.2651$$

These systems are combined as in Equations 4.39 and 4.40.

In Figure 4.3 the performance in terms of input signal ($\mathbf{y}(k)$) to input noise ($\mathbf{y}'(k) - \mathbf{y}(k)$) ratio (SNR) in decibel and SNR of the estimate for a range of Q to R ratios is shown. The estimate noise is defined as the estimate $\hat{\mathbf{x}}(k)$ minus the computed signal $\mathbf{x}(k)$. In Figures 4.5 and 4.4, select deconvolution results are shown for square-wave and white Gaussian noise respectively. As can be seen, the performance of the Deconvolution Kalman filter is slightly better for the square-wave signal. For the square-wave, the estimate SNR rises to almost as high as the measurement SNR, for the white Gaussian noise input, the estimate SNR is markedly lower than the measurement SNR, indicating the DK filter adds noise. This is contradiction with the statements made in [10]. It must be noted that the exact circumstances in terms of Q and R were not disclosed. A possible explanation for the lower performance in terms of Gaussian noise removal of the Deconvolution Kalman filter, compared to the regular Kalman filter, is that the same Q/R ratio is used to estimate two different processes. For the deconvolution to work well, the Q/R ratio needs to be set suitably high, or else the magnitude of the estimation will be lower

than the value to be estimated, which is clearly observable in Figure 4.5. This error in steady state magnitude converges to a nonzero magnitude for an ill-chosen Q/R ratio. One needs to pay attention to this behaviour, and ideally set up the experiment such that there is a portion of which there is a region in the force data of which a nonzero magnitude is known. Then this part can be used as a check on the magnitude of the DK filter, utilizing the behaviour of the amplitude error for the entire force history. As can be seen in the figure, if the force magnitude is correct for the steady state, it is correct over the entire dataset (after convergence of the Kalman gain). The filter still performs up to expectations as, for high enough Q/R and high enough SNR, the estimate SNR rises to over 50 dB. For lower measurement SNR values, the error reaches a plateau when the Q/R ratio is suitably high.

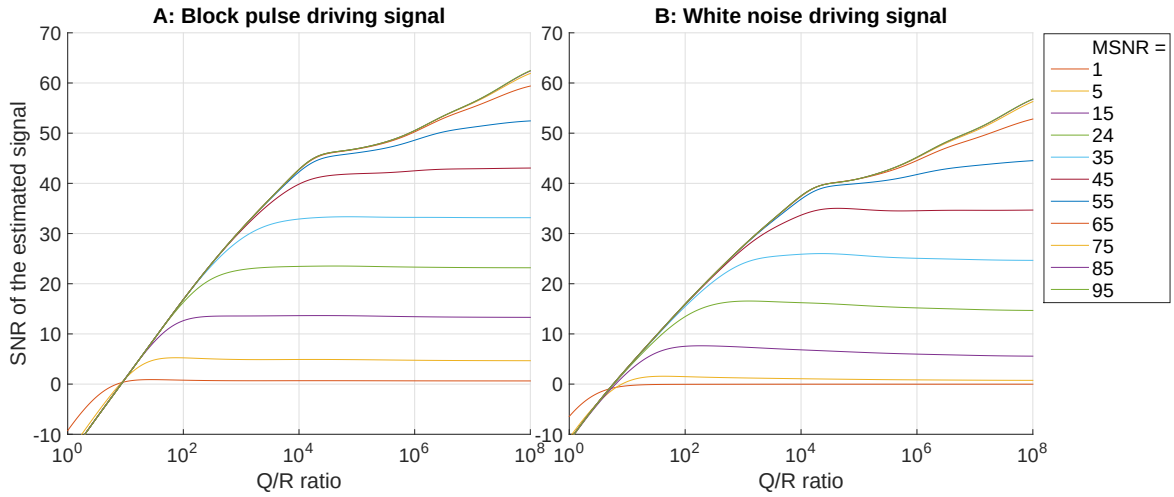

Figure 4.3: Estimation SNR for various measurement SNR (MSNR) values and Q/R ratios for both square wave input and random noise input

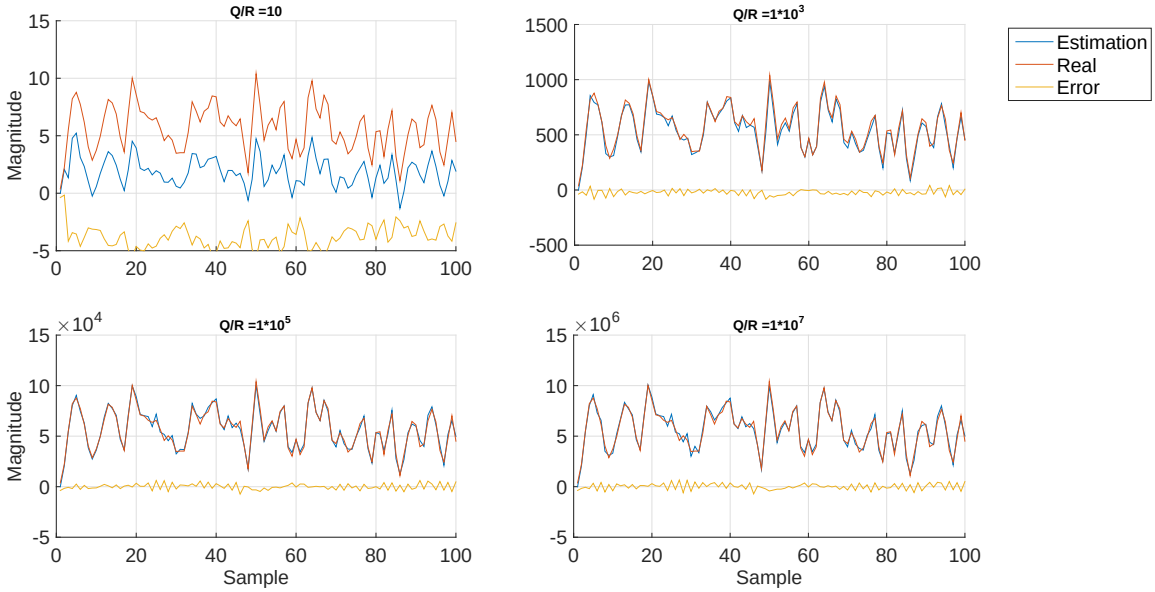

Figure 4.4: Deconvolution results for 40 dB measurement SNR white-gaussian noise input signal for various Q/R ratios

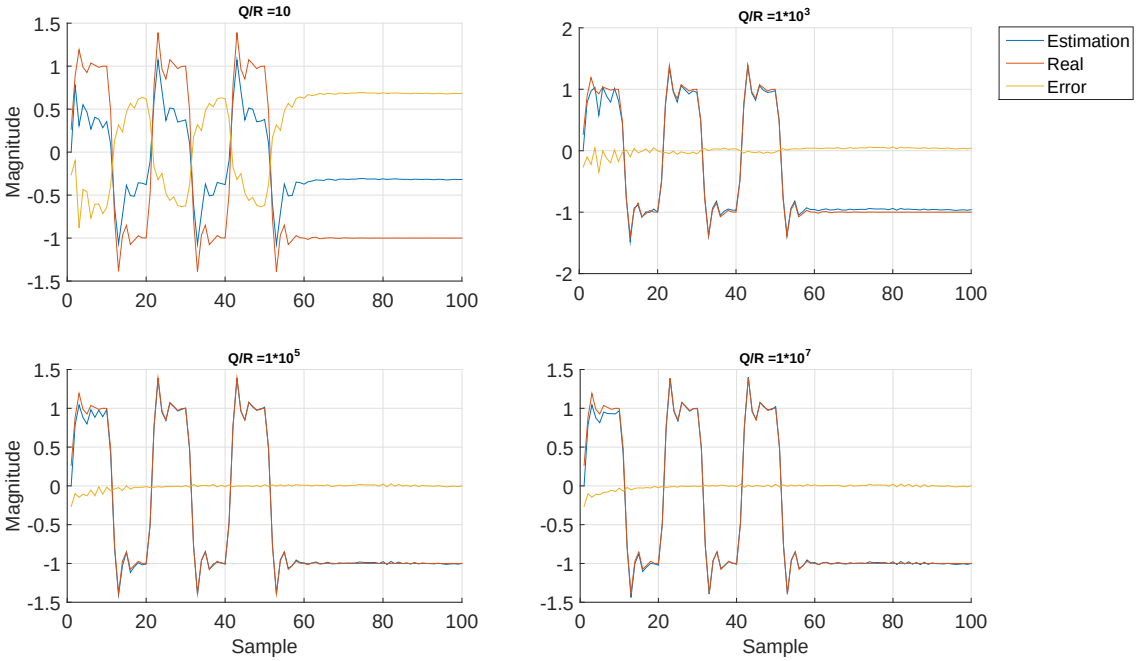

Figure 4.5: Deconvolution results for 40 dB measurement SNR block-pulse input signal for various Q/R ratios

4.1.4. State space system error sensitivity

In the previous section, the sensitivity of the Deconvolution Kalman filter to changes in the Q and R matrices have been discussed. Also, the DK filter was tested for noisy measurements. However, the measurements are not expected to be very noisy. As explained in Chapter 3.3, the measured, denoised data is expected to have a small measurement error besides the mechanical influence. On the other hand, as will be explained in Chapter 4.2, some necessary assumptions were made in the system identification process. These assumptions might lead to an identified state-space model which is not exactly describing reality. This was also the case in [1], however, it was found that the DK filter still proved better performing than the other tested deconvolution schemes. In the thesis of Richard Ahlfeld, it was possible to determine the magnitude of the difference between the simulated and real response. As will be shown in the following sections, this is not possible for the measurement setup currently under consideration. Therefore, a sensitivity test is set up to investigate the impact of DK filtering with a misidentified state-space model. The state space system pair identified in Chapter 4.2 is used to generate a synthetic force history from the quasi-steady model. The state-space systems are modified in terms of resonance frequency to generate a set of misidentified state-space systems. The resonance frequency is the selected parameter to modify, as changing the behaviour of the system in other ways would make the eventual results difficult to interpret. The resonance frequency is shifted 20, 10, and 5% upwards and downwards to obtain 6 'misidentified' system pairs. The bode plots of these misidentified systems together with the identified system is shown in Figure 4.6. The deconvoluted signal together with the reference deconvoluted signal is shown in Figure 4.7. The standard deviation from the original signal is shown as well. As can be seen, the SD for the perfect system is very small, and the standard deviation rises linearly with the system shift. This linearity demonstrates a degree of robustness of the DK filter, and if the error in system identification is small, the corresponding error in the deconvoluted result is expected to be small as well. The magnitude of the signal stays intact, and the general shape of the signal is conserved as well. Still, the error due to misidentification of the state-space system are much larger than the expected measurement error.

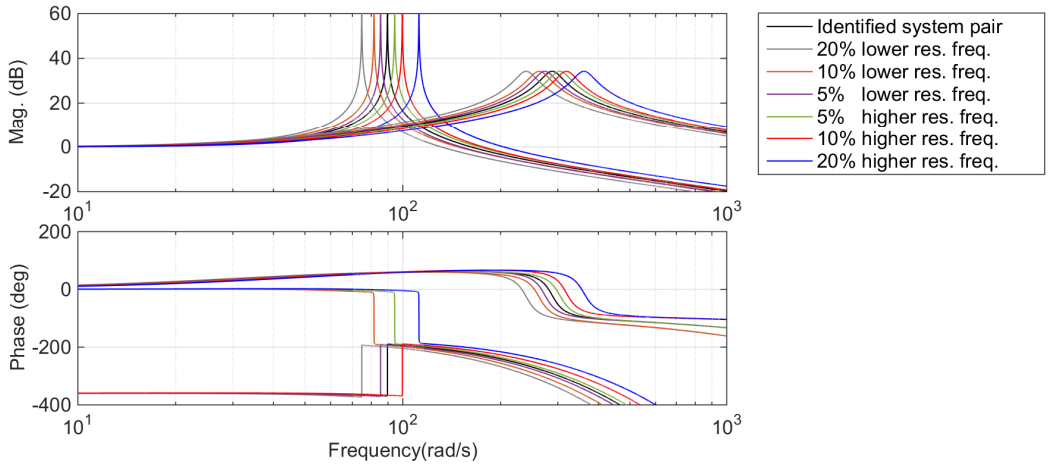

Figure 4.6: Bode plots of modified systems compared to non-modified system

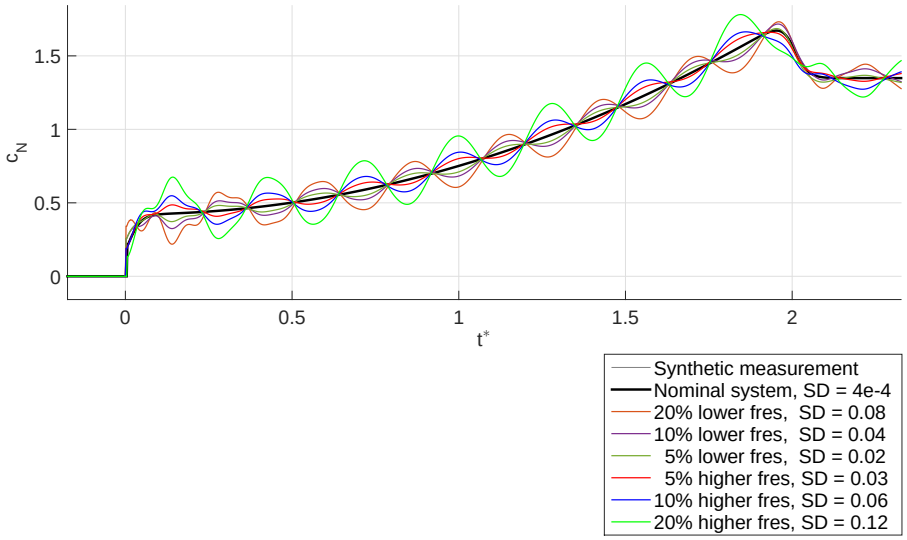

Figure 4.7: Deconvolution results for 40 dB measurement SNR block-pulse input signal for various Q/R ratios

4.1.5. DK filter accuracy summary

The identified factors for the error in the filtered result were the (1) filter algorithm itself, the input noise, the shape of the input signal, the Q/R ratio, and how well the system used in the filter matches with the system that is convoluted with the signal to be estimated. Of these, it was found that for an experimentally representative input signal and a measurement noise in the range of 30 dB to 60 dB, the Q/R ratio can be tuned with relative ease to find an estimation error slightly larger than the measurement error if the system representation is perfect. However, it is possible that an imperfect Q/R ratio leads to results that are correct in terms of shape, but incorrect in terms of magnitude. Therefore, it seems prudent to design at least a part of the experiment such that there is at least a phase where the forces are known. In terms of revolving-wing measurements, after few chord lengths travel where the wing is moving at a constant velocity, the vibrations will have damped out, and the value attained can be used to check the results of the DK filter. The chance of error due to a wrongly-chosen Q/R ratio is expected to be small due to the broad range of Q/R ratios giving optimal results for a given input noise and perfect system identification. But as can be seen in the figures of this chapter, a misidentified system introduces much larger errors in the DK filtered results. Therefore, the focus on accuracy in the rest of this thesis will be on the identification of the correct state-space matrices, rather than finding the optimal Q/R ratio.

4.2. System Identification

4.2.1. Introduction to system identification

For the DK filter to work, as described in Chapter 4.1, the test rig vibrations need to be captured in a state-space system. Converting the real-world test setup into a mathematical model is termed system identification, and is not trivial [42]. For tractability, one can compare the system identification to finding a collection of springs, masses, and dampers that respond in the same way as the experimental setup. The response of such a collection of springs, masses, and dampers can be converted into a set of equations, such as the state-space form explained in Chapter 4.1. To find this state-space system, an optimization algorithm searches for the best fitting set of parameters that recreates a given output from a given input.

4.2.2. Process

The system identification process consists of three parts: (1) obtaining a force input signal, (2) obtaining a force output signal, and (3) finding a fitting set of equations that describe a process that matches the input to the output.

Input force

The force input signal ideally contains the entire frequency spectrum to have a complete description of the system behaviour. When trying to measure the input force on the system, one encounters the same problem for which the deconvolution filter and the system identification process is needed, as it is only possible to measure the output, which is the input, convoluted with the mechanical system response. Therefore, it is necessary to make assumptions regarding the input force. In [58] a quasi-steady model for revolving wings was proposed. This model distinguishes between forces generated due to revolving acceleration and revolving velocity. Especially for the added mass part of the generated fluid-dynamic forces (Chapter 2), this model offers a good approximation [49].

With the quasi-steady model accurate enough to estimate generated forces during the acceleration part of the motion, a motion profile is chosen such that it consisted primarily of acceleration, with low displacements, and low velocities. The motion profile consists of a sharp acceleration peak up and a sharp acceleration peak down over a short timespan. The forces on the wing during this motion can be computed accurately using the quasi-steady model. To take up any mechanical slack during the motion, the acceleration pulse was given while the wing was revolving at low velocity. This low revolving velocity (0.05 m/s at 75% span, see Chapter 3.2) is not expected to influence the force production due to acceleration, as the force production due to wing acceleration is expected to be purely inertial and linear. The wing revolves for 5 t* at the described low velocity to let the mechanical vibrations caused by the initial startup damp out. The velocity input to the motor during the impulsive motion phase is shown in Figure 4.8 and the calculated force is shown in 4.9 respectively. It must be noted that only the velocity input to the motor is shown, as the sampling rate of the feedback on the position of the motor was 33 Hz, not high enough to obtain a detailed force input over the short amount of time. Furthermore, the motor control used a special control system to position the wing accurately. This can be seen in the irregular shape of the velocity input graph (Figure 4.8), therefore the motor controller feedback data is less suitable to obtain input force measurements.

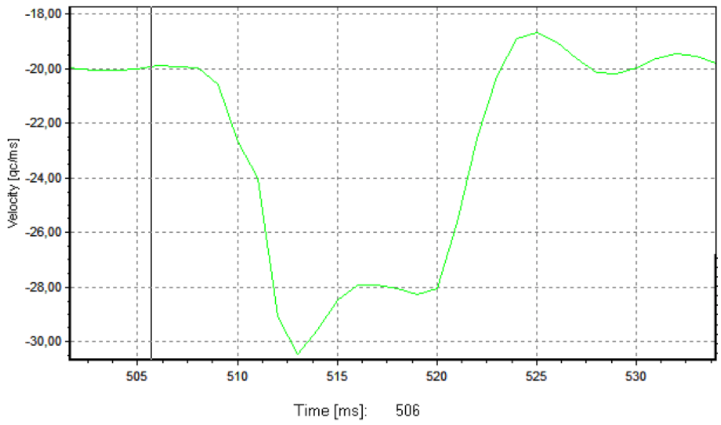

Figure 4.8: Velocity data screenshot from Maxon motor control software.-1 qc/ms is equal to 0.004 m/s at 75% span

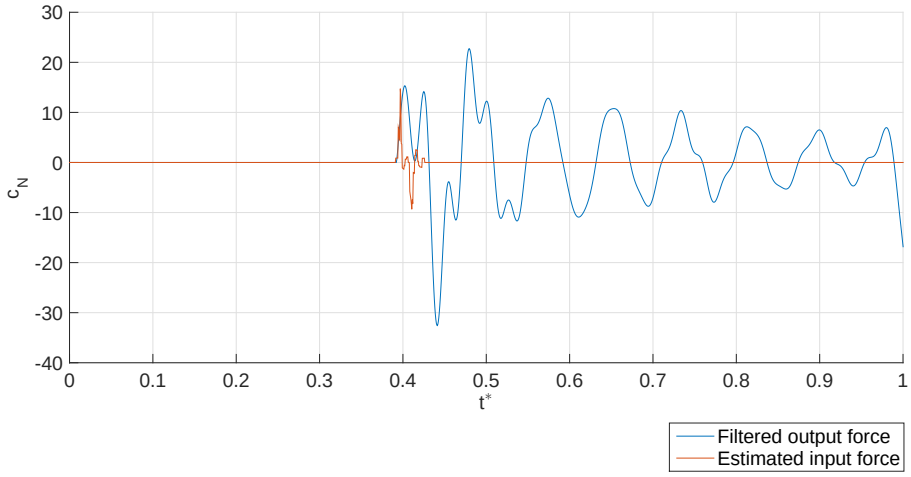

Figure 4.9: Quasi-steady estimated input force and 33 Hz Chebyshev Type II low-pass filtered output force for use in system identification algorithm

Output force

The output force of the wing ideally is the input force convoluted with the state-space system representing the motion. The measured output force therefore is assumed to be free of time-delayed nonlinear force generation due to the accelerative input pulse. As the wing is revolving at the mentioned 0.05 m/s the mechanical oscillations are expected to be centered around the steady-state value of force production at that velocity. The experiment was repeated ten times and ensemble averaged. The obtained force history is shown in Figure 4.10. The start-up occurs at 0.5 t*, then clearly the mechanical resonance is excited. At around 1.5 t*, these vibrations have damped out. At 5 t*, the acceleration pulse is given, giving rise to substantial vibrations. The motion is stopped at t^* =5.5. Interestingly, during the steady part of the motion, where very little oscillations are expected, there is still a lot of noisy behaviour. To investigate, a Welch's power spectral density (PSD) estimate of the measured force is made. This estimate is shown in Figure 4.11. Clearly to be seen are some very narrow-band frequency peaks, the first one at 50 Hz. These peaks are assumed to be too narrow to be purely mechanical resonance, and therefore are deemed difficult to filter out, as high-order response modelling is required. Therefore, the signal is low-pass filtered with a Chebyshev Type II low-pass filter with a cut off frequency of 50 Hz. This leaves power peaks at two frequencies. These peaks are broad, and around 15 Hz and 45 Hz. Taking into account that the magnitude of the generated fluid-dynamic force is low during the steady part of the velocity, and the expected change in fluid-dynamic force generation only happens over a short amount of time (around 33 Hz, or 0.03 t*, these oscillatory peaks are attributed to the mechanical resonance in the structure.

The impact of low-pass filtering at 50 Hz on the fluid-dynamic force measurements is investigated in Chapter 4.2.4. The resulting input- and output force data to be used for the system identification are shown in Figure 4.9.

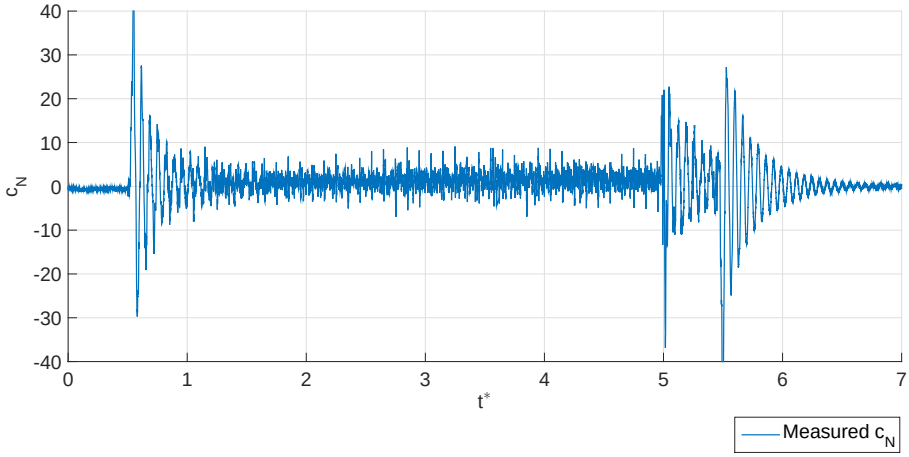

Figure 4.10: Ensemble averaged measured output

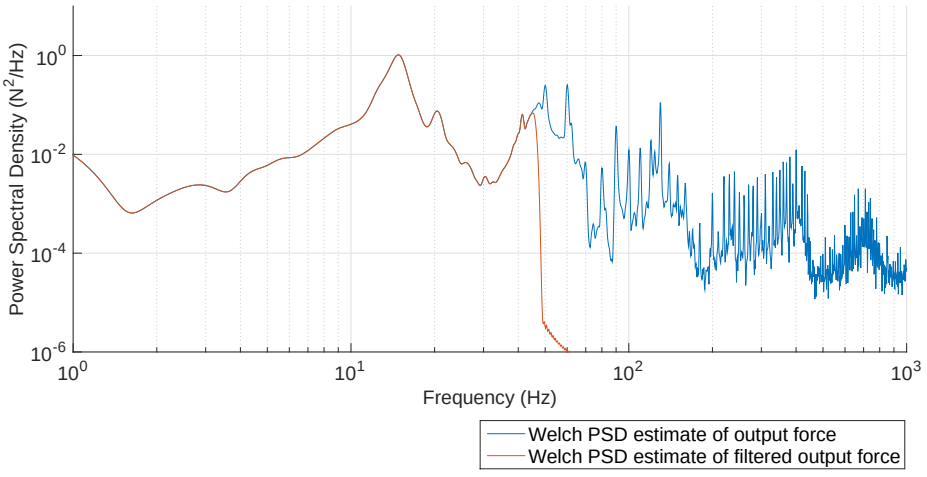

Figure 4.11: Unfiltered and 50 Hz Chebyshev Type II low-pass filtered measured output force Welch's PSD estimate

4.2.3. Implementation

From the output signal, only the portion after the start of the acceleration peak is used in the system identification algorithm. The mean is subtracted as that represents the steady-state revolving part of the signal. After consulting Richard Ahlfeld, a lead-in tail of zeros is added to the signal and only the first four cycles of the main mode were considered part of the output. These steps are for ease of convergence for the system identification algorithm. The nominal output signal and input signal to be used in the system identification algorithm are plotted in Figure 4.9. The system identification algorithm used was the Prediction Error Minimization (PEM) algorithm from the System Identification Toolbox in Matlab. This is an iterative optimization algorithm which aims to find a transfer function that can be used to reconstruct the output, given the input. With the described input and output, the PEM algorithm produced transfer functions that had a non-zero gain for low-frequency to DC signals. These systems could not be considered as describing the real world situation. Mechanical equilibrium states that for a constant applied force, after the vibrations have damped out, the input force is the same as the output force, which means there can be no gain for a DC signal. In the input-output signal pair there seems to be a lack of information on the mechanical behaviour at very low-frequency as evidenced by the drop in power for low frequency (< 45 Hz) signals in Figure 4.11. The PEM algorithm lacks the physical insight and therefore, the notion that there should be zero gain at low frequencies should be passed to the algorithm. To do this, a very low frequency (1 Hz) sine signal was summed with both the input and output forces. It was not possible to add this information using the input signal. If the input signal were to be longer, the nonlinear fluid-dynamic effects are expected to interfere with the assumption that the output force is predominantly the result of the linear system representing mechanical vibration. To adequately identify a transfer function with a double response peak as expected from the Welch PSD estimate of the output force would leave the optimization algorithm with a large amount of free variables, leading to the chance of the algorithm finding erroneous results. However, from observing the PSD estimate in Figure 4.11, the transfer function to be found is expected to have two resonance peaks, one around 15 Hz and one around 45 Hz. Therefore, the PEM algorithm was first tasked to find a 2-pole and 1-zero transfer function focussing on the 0 Hz to 45 Hz part of the signal, and a secondary transfer function describing the response from 40 Hz to 50 Hz. By setting these limitations on the search space, the PEM algorithm was able to identify two transfer functions. These were rewritten in state-space form to use in the DK filter.

4.2.4. System Validity

The identified system pair is shown by way of state-space matrices and Bode response plots in Equations 4.44, 4.45 and Figure 4.12 respectively. To test the applicability of the system pair for deconvolution, the original signal used for the system identification is DK filtered using the system pair sequentially in the DK filter. It makes sense to test the system pair directly in the DK filter as that is the only reason the system pair was identified. This is shown in Figure 4.13, together with the 50 Hz low pass filtered quasi-steady estimate of the forces generated during the start and the end of the complete motion. As can be seen, these forces are replicated within a margin of error acceptable for a quasi-steady model. The shape is also correct, with no large, spurious oscillatory structures present. The acceleration pulse used as input is also replicated in a qualitatively correct way as there is a definite up and down pulse. This pulse is stretched out in time quite significantly. The source of this error could be that the motor input does not exactly represent the actual input. The motion start and motion end are replicated in agreement with the expectations. But, the acceleration pulse is not replicated to the same degree. Therefore, this test is considered not sufficient to either accept or discard the identified system pair as being a suitable model for the experimental setup. Formal verification is very difficult as it is not possible to determine the exact forces the DK filtered result should replicate. However, for the revolving-surging experiments, it is possible to gather some information on features a correctly filtered force history result should have. These features should be present in the DK filtered force histories.
Another option that is explored is a replication of the DK filter sensitivity test. Replicating the synthetic results with the measured data can show if the signal quality, determined by observing the previously obtained features from the measured signal, changes for a modified system pair. If the force signal quality improves when DK filtering with the modified systems, it follows that the identified system cannot be accepted as being a good representation.

System 1:

$$\begin{aligned}
\mathbf{A} &= \begin{bmatrix} 1.998 & -1 \\ 1 & 0 \end{bmatrix} \\
\mathbf{B} &= \begin{bmatrix} 0.25 \\ 0 \end{bmatrix} \\
\mathbf{C} &= \begin{bmatrix} 0.214 & -0.206 \end{bmatrix} \\
\mathbf{D} &= 0.052
\end{aligned} \tag{4.44}$$

System 2:

$$\begin{aligned}
\mathbf{A} &= \begin{bmatrix} 1.96 & -0.981 \\ 1 & 0 \end{bmatrix} \\
\mathbf{B} &= \begin{bmatrix} 1 \\ 0 \end{bmatrix} \\
\mathbf{C} &= \begin{bmatrix} 0.973 & -0.972 \end{bmatrix} \\
\mathbf{D} &= 0.992
\end{aligned} \tag{4.45}$$

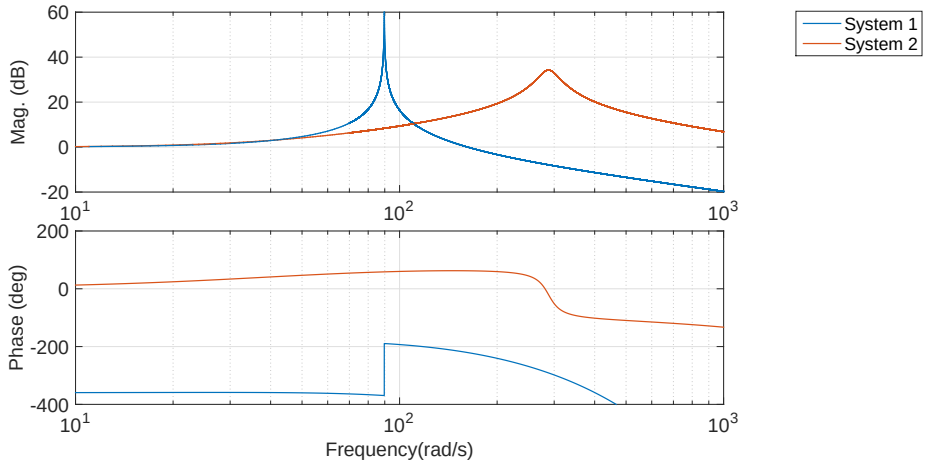

Figure 4.12: Bode plot of identified system pair response

Measurement data information

As stated, it is possible to define qualitative properties of the force history for the revolving surging experiments, that can be used to assess the validity of the DK filtered force history.

For this test case, the measured, 50 Hz filtered normal force from the $45\,°\alpha$ revolving-surging experiment (see Chapter 3.2) is used. This force is plotted in Figure 4.13, together with the quasi-steady estimate. The first observation is that the vibrations are mostly excited by the parts where there is a notable jump in the expected fluid-dynamic force, such as at the start- and end of the acceleration phase. This is illustrated more clearly in Figure 4.14, where the measured normal force coefficient (c_N) is band-pass filtered with to accentuate the measured vibrations, together with the acceleration data of the motion. As the magnitude of the oscillations follows a decaying trend outside of regions where there are jumps in the expected fluid-dynamic loading on the wing, these oscillations are consistent with

mechanical vibrations, rather than fluid-dynamic loading. If the oscillations were to be fluid-dynamic in origin, they are expected show a rise in magnitude as the wing reference velocity increases for 0 t* to 2 t*. Therefore, it is expected that the qualitative behaviour as prescribed by the quasi-steady model holds true, and it is expected that the 'true' fluid-dynamic force on the wing is free of large scale oscillations for parts of the motion that are not part of the acceleration phase. This also suggests the true force should be very close to the conventionally filtered results for the phase of the motion with a constant revolving velocity. The second notion is that since the wing is impulsively started, the initial force rise should be steep. As can be observed in Figure 4.13, these notions are generally true for the deconvoluted results under consideration.

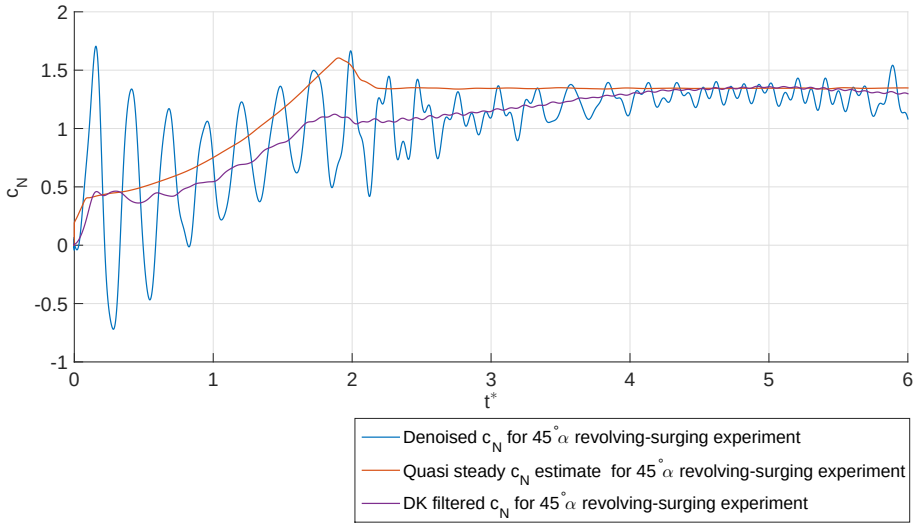

Figure 4.13: 50 Hz low-pass denoised measurement, Quasisteady estimate and DK filtered normal force coefficient for the 45 °α revolving-surging experiment

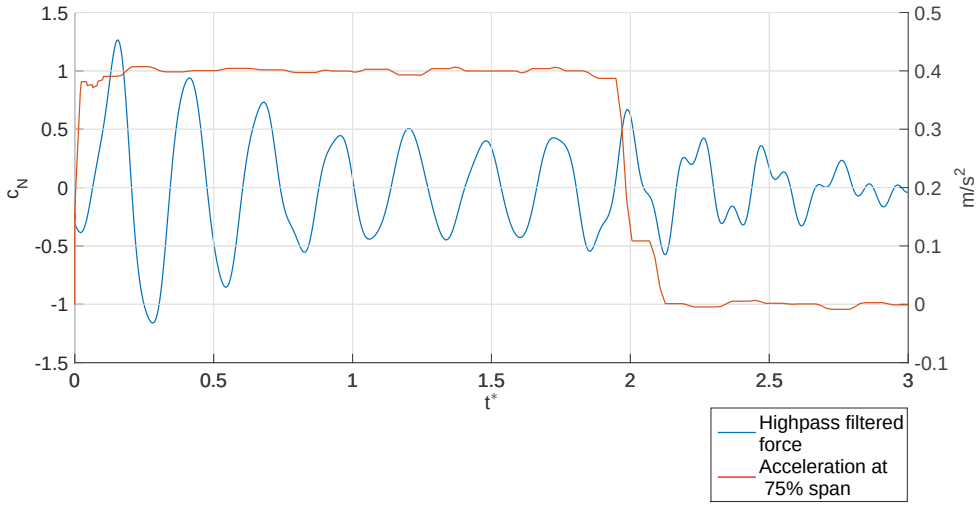

Figure 4.14: 6 Hz to 50 Hz bandpass filtered measured c_N, revolving acceleration.

Sensitivity test

The second test on the DK filtered force history is a replication of the sensitivity test from Chapter 4.1. To replicate this test, measured force data is used, instead of synthetically generated data, and then deconvoluted with the same 'shifted' systems. As can be seen in Figure 4.15, when compared to Figure 4.7, the qualitative behaviour is very similar, with the modified system pairs not quite capturing the mechanical dynamics, leaving progressively larger oscillations in the deconvoluted result for larger discrepancies between the identified and modified systems. This indicates that in terms of resonance frequency, the optimization algorithm seems to have found an optimum that matches the system dynamics up to 50 Hz.

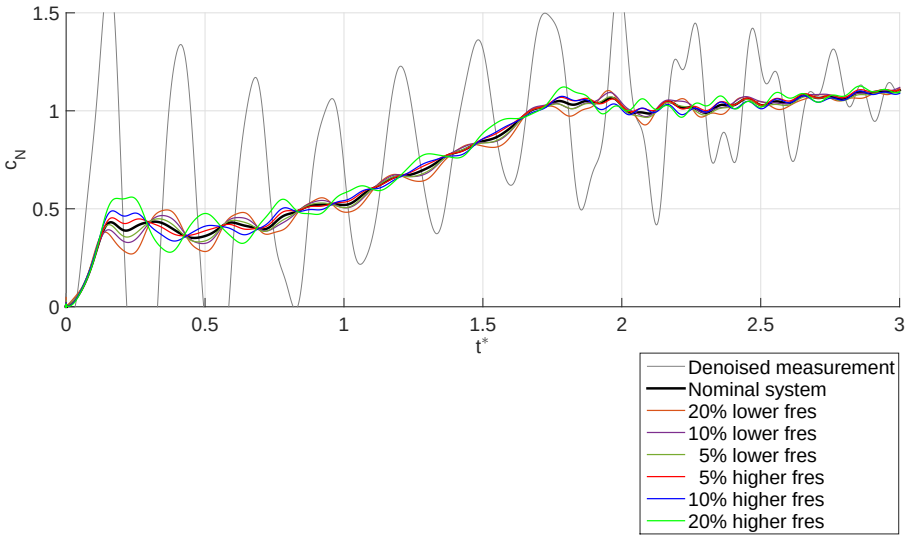

Figure 4.15: Sensitivity test for measured data, compare with Figure 4.7. The denoised measurement refers to the 50 Hz low-pass filtered data.

Frequency range of the deconvoluted result

As shown in Chapter 2, a low-pass filter has the risk of impacting the actual forces to be measured. In this thesis, due to measurement limitations, it was not possible to identify a system pair that could represent the mechanical dynamics above 50 Hz. Even identification for the dynamics below 50 Hz was not trivial. However, this has necessitated the use of a 50 Hz low-pass filter. It is important to know if this impacts the fluid-dynamic force measured. To this end, the obtained DK filtered result is filtered with progressively lower cut-off frequency Chebyshev type II low-pass filters, until the result is judged to diverge too much from the original result. This is shown in Figure 4.16. It was concluded that the results do not diverge much from the 50 Hz filtered result up until a 26 Hz cut-off frequency. The 26 Hz cut off frequency influences not only the peak position, but also the steepness of the flank of the force signal. The peak is shifted to 0.02 t* later, compared to 0.01 t* shift of the 32 Hz filtered force. As there seems to be no fluid-dynamic force information lost when filtering with a cut-off frequency of 32 Hz compared to 50 Hz, it is concluded that it is unlikely that the fluid-dynamic force has frequency components above 50 Hz. Therefore, the 50 Hz upper bound found in the system identification process is not expected to have an influence on the measured force. Converted to convective time, a 32 Hz response is around 8 cycles per t*. In terms of insect wing kinematics, with a 180 degree flapping angle, properly resolving force generation requires a measurement system that is capable of resolving at least 120 cycles per wing beat.

Also shown in Figure 4.16 is the linearity of the DK filter, where the sequence of filtering is inverted. The results for first low-pass filtering then DK filtering are the same as when the measurements are first DK filtered and then low-pass filtered.

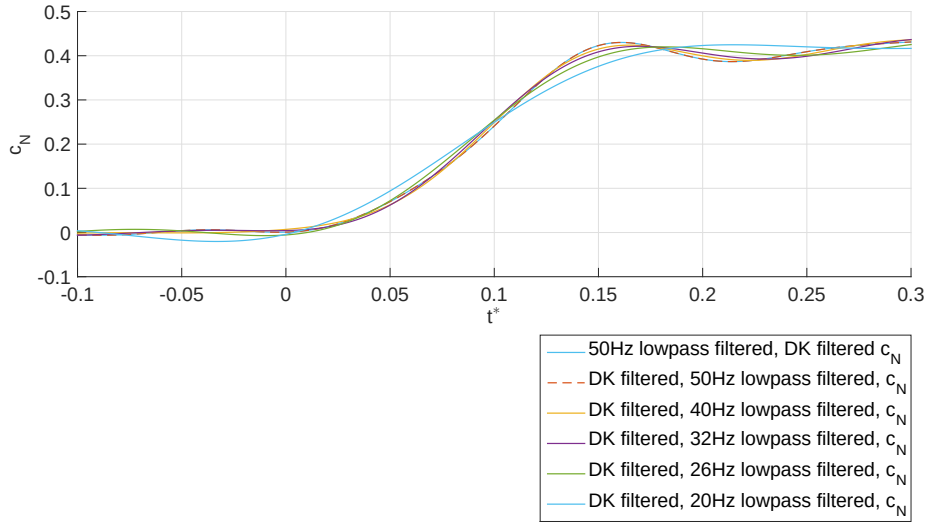

Figure 4.16: Comparison for low-pass filtered data.

System Validity conclusion

In conclusion, the DK filtered force is in agreement with the expectations for the fluid-dynamic force, and if the system pair is modified, the DK filtered force agrees progressively less well with the mentioned expectations. Therefore, the author accepts the identified system pair as suitable for use in the DK filter. There is no appreciable difference in low-pass filtering the measurements at 50 Hz or at 32 Hz, from which it is concluded that the 50 Hz low-pass filter does not interfere with the fluid-dynamic force measurements.

4.2.5. System Applicability

In Chapter 4.1 the DK filter was found to be robust in terms of small errors regarding resonance frequency in the system identification. This was repeated in this chapter, with the systems that were slightly modified not having a large influence on the estimated force. Therefore, it seemed possible that the identified system pair would also be suitable for use in the DK filter for slightly modified experimental setup. The system pair was identified with the wing pitched to $45\,°\alpha$. As a different pitch angle could represent a slight change in response, the DK filter performance was investigated for other angles of attack from $8\,°\alpha$ to $80\,°\alpha$. As the basic structure of the measurement setup does not change, the mathematical structure of the state-space system representing the mechanical structure should not be impacted either. For this investigation, it was recalled that a system misidentified in terms of resonance frequency did not influence the magnitude of the DK filtered forces, but did increase the oscillations in the force. To quantify the mis-fit, the measured signal is filtered with a 32 Hz low-pass filter as discussed in the previous section. This way, the increase in oscillations can be quantified, without impacting the shape of the signal. The increase in oscillations is quantified by way of normalized standard deviation. This is plotted in Figure 4.17, where it can be seen that the standard deviation increases for angles of attack smaller than $45\,°\alpha$. However, as the system was identified for a wing at $45\,°\alpha$, the standard deviation was also expected to increase for angles of attack greater than $45\,°\alpha$, as the changes in mechanical dynamics are expected to be qualitatively similar for pitching up or pitching down. It is concluded that the rise in standard deviation is mainly due to a lower signal to noise ratio for the wing at a lower α, as the noise stays the same, but the generated fluid-dynamic force is lower. The force history shape stays the same for the entire range of α.

The force components also suffered from low signal to noise ratio due to a low force magnitude. It was therefore not possible to obtain a state space representation for these forces individually. However, it was observed that the wing itself is the least stiff in the normal force direction. In the tangential force direction, the wing is very stiff, and also in the pitching moment direction, no wing vibrational modes

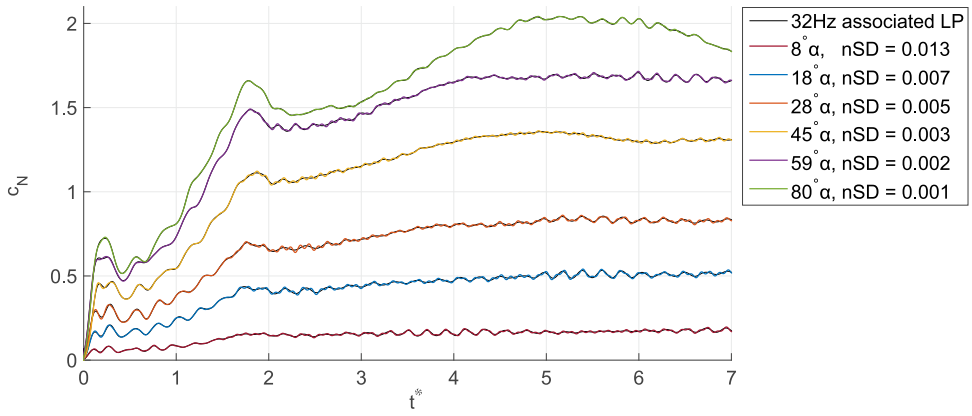

Figure 4.17: DK filtered response compared to 32 Hz low-pass (LP) filtered DK filtered response of selected experiments. Note that it is difficult to ascertain differences, but this is this by design as the 32 Hz low-pass filter was chosen as being at the boundary of not meaningfully interfering with the measured data.

are expected in the wing itself. Therefore, the mechanical structure that causes the vibrations in the wing normal direction is expected to be very similar to the structure causing vibrations in the wing tangential- and moment direction. In Figure 4.18, the Welch PSD estimate for the normal force impulse measurement, tangential force and moment around the centre of pressure (see Chapter 5.1 and 5.2), during the surging acceleration of the motion is given. As can be seen, the PSDs are very similar in shape and therefore it seems likely that the magnitude and tangential force can be DK filtered with the same system pair identified for the normal force component. This is shown in Figure 4.19, where the DK filtered pitching moment and tangential force are shown. These results seem much noisier than the DK filtered normal force, however the reader is advised to take note of the Y-axis scale. The DK filtered results are further smoothed by filtering with a 32 Hz low pass filter as it was demonstrated that the information on the generated fluid-dynamic force is not affected by this low pass filter.

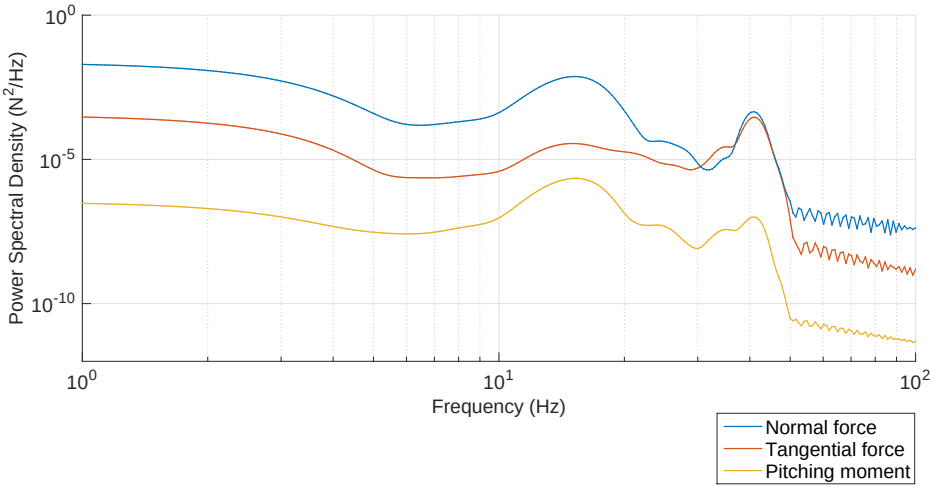

Figure 4.18: Welch PSD estimate for the impulse start portion of the motion 0 t* to 1.5 t* for all force components

In conclusion, it can be stated that the identified system pair is suitable in the DK filter to filter the normal force, tangential force, and pitching moment for the measurement setup at all angles of attack. This conclusion seems too convenient, but one must keep in mind that the measurement apparatus

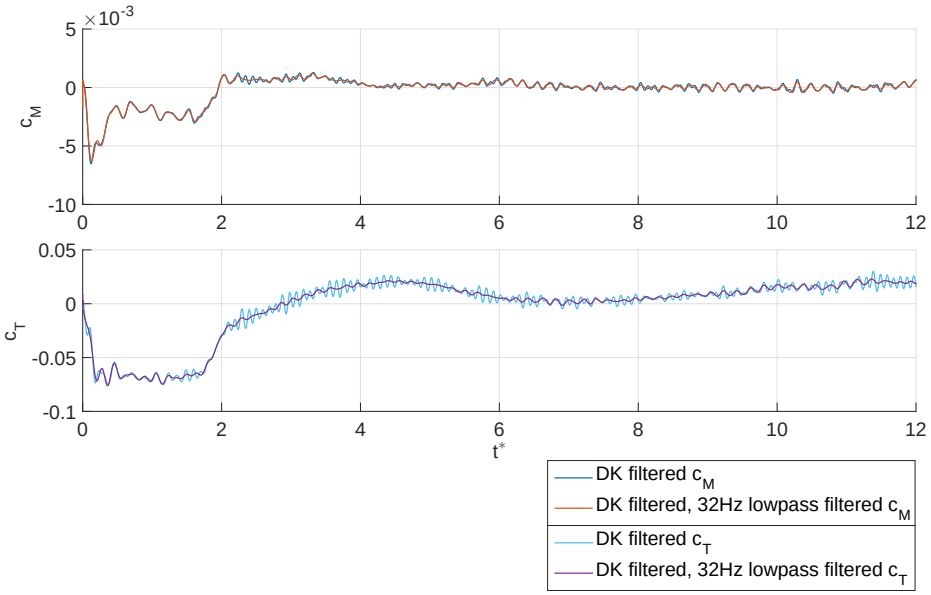

Figure 4.19: DK filter performance for tangential force and moment coefficients. Note that the moment is around the centre of pressure for steady motion.

stays the same for all the measurements, and the goal of using the DK filter is to filter out vibrational modes of the measurement apparatus. It would be unlikely that the vibrational modes are aligned exactly with a measured force direction, and therefore it follows that any vibrational mode is expected to have a very similar influence on each measured force component. Furthermore, small variations in the wing mounting are not expected to have influence on the wing modes itself as the wing shape and wing mounting type stays the same. A change in wing mounting on the entire measurement apparatus is unlikely as well, since the wing is low in mass compared to the complete setup. In retrospect, it is therefore not unexpected, nor coincidental that the single identified system pair is suitable for all pitch angles and all force components.

5

Measurement results and discussion

In this chapter, the measurement results are presented. First, the revolving-surging experiments are discussed, then the revolving-pitching experiments. The presentation of the measurement result is in terms of c_N, c_T, force vector angle, and center of pressure location. The measured forces during the acceleration phase and during the steady phase are discussed separately. It was observed in [49] that, for revolving-surging and revolving-pitching experiments, the generated c_T is sufficiently small to consider the force generation to consist mainly of normal force. Therefore, in this chapter, the forces will be discussed mainly in terms of normal- and tangential force instead of the lift- and drag force as is customary in steady-flow aerodynamics. As discussed in Chapter 2, a typical filtering setup has a cut-off frequency in the region of 15 Hz, and in Chapter 4.2.4, the required frequency range to capture all dynamics in the measurement is up to 32 Hz. The conventional filtering setup is not further discussed in this chapter. The discussion on the performance increase of the DK filtering compared to a more conventional filtering setup can be found in Vester et al. [63].

5.1. Revolving-Surging Results and discussion

5.1.1. Unsteady force generation

As discussed, the force normal to the wing surface is expected to be the largest component of the total force generation. The c_T and c_N conventions as used in this report are shown in Figure 5.1. The c_N values of the revolving-surging experiments for the period t^* = 0 to 8 are shown in Figures 5.2 to 5.4. It is clear that the normal force history is in general similar for increasing α. As the motion starts, there is a short-lived peak in generated force, around 0.2 t^* wide. Then the force rises sharply as the wing accelerates. Just before the end of the acceleration phase (t^* = 2), the force rise levels off. The fluid-dynamic mechanism responsible is unknown, but the steep rise levels off at the same point in time for all motions. As the motor controller setup provides revolving velocity feedback, it was checked that there were no changes in the velocity at the time the rise in normal force levels off. The maximum c_N magnitude during the acceleration phase is lower than the steady c_N value, presumably as circulatory effects continue to build up after the acceleration phase As the acceleration falls to zero, the normal force drops off. The magnitude of this drop-off is almost zero for lower α, and up to Δc_N = 0.2 for higher α. A possible explanation is a lower acceleration in the wing-normal direction for the cases of small angles of attack. After the acceleration phase, there is a broad 'hump' during 2 t* to 8 t* during which the measured c_N rises and then drops to the steady-state value. The prominence of this 'hump' feature correlates well with the angle of attack, again with the larger α showing a larger difference between the maximum attained value during the hump and the steady-state value. The experiments with a lower α show almost no hump, with only a gradual rise towards the steady value. The experiments at high α in Figure 5.4 are very similar for the initial phase of the motion. This indicates that at very high α, the force generation is to be strongly linked to the cross-sectional area in the direction of motion.

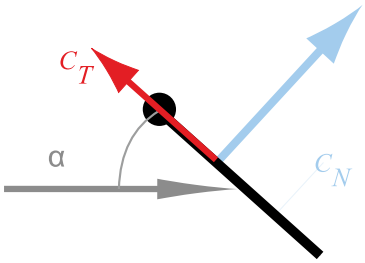

Figure 5.1: Directions of c_N and c_T vectors, following the convention of Figure 2.1. The c_N vector is perpendicular to the wing chord, c_T is parallel to the wing chord with a positive c_T towards the wing leading edge.

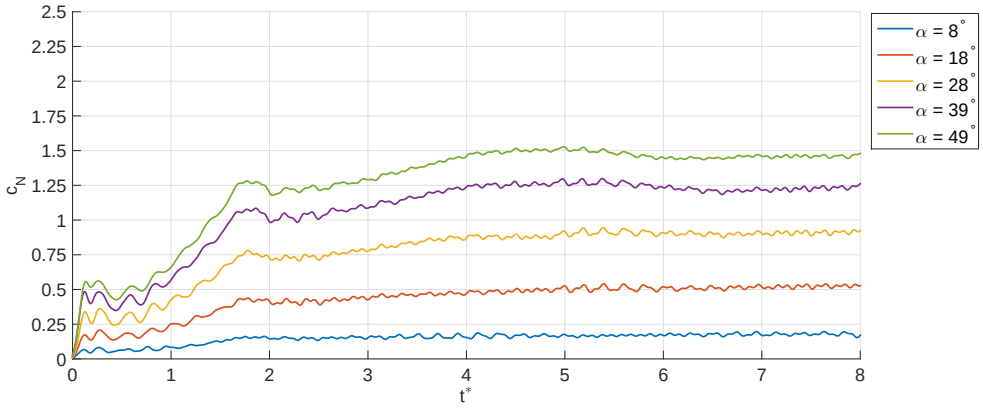

Figure 5.2: DK filtered measured normal force coefficients for 8, 18, 28, 39, and 49°α.

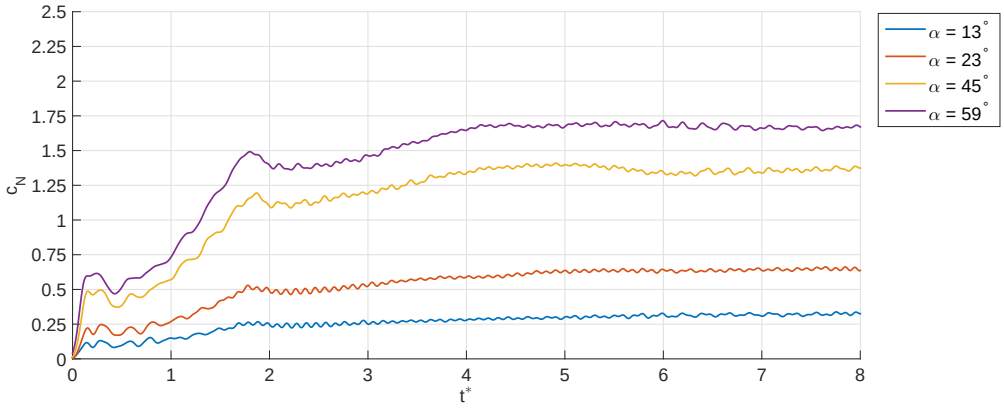

Figure 5.3: DK filtered measured normal force coefficients for 13, 23, 45,and 59°α.

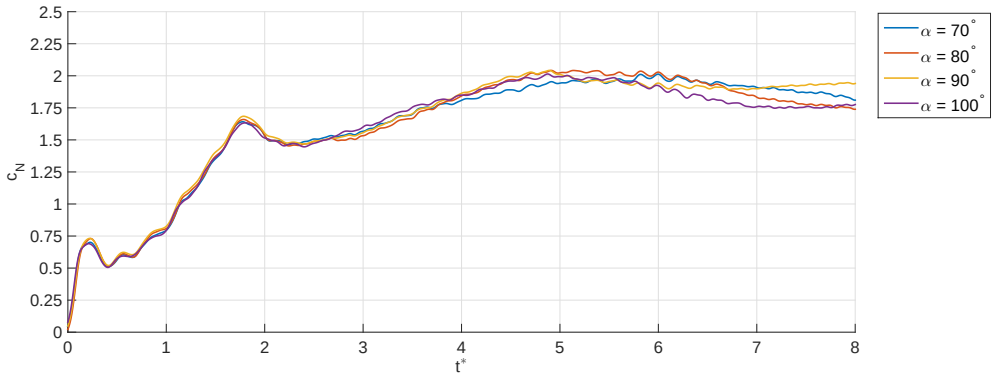

Figure 5.4: DK filtered measured normal force coefficients for 70, 80, 90, and 100°α.

The DK filtered, 32 Hz low-pass filtered (as described in Chapter 4.2) tangential force coefficients (c_T) are plotted for all measured angles of attack in Figures 5.6,5.7, and 5.8. To obtain a reasonably smooth result, visually free from spurious oscillatory effects, the c_T force history requires 32 Hz low-pass filtering due to the low signal to noise ratio. Still these forces are less visually clean than the c_N measurements, but the trend is observable. The first thing to notice is that the c_T is small compared to the c_N for all but the lowest α, which is as expected as the force vector of the tangential force aligns itself with the motion for lower α. The c_T seems to be less dependent on α than the normal force coefficient. In general, the c_T starts negatively and stays negative during the acceleration. This is in line with the expectations as the wing is accelerated forward, and the reaction force is expected towards the trailing edge of the wing. However, for those measurements that show a more pronounced c_N 'hump' from 2 t* to 6 t*, the c_T values show a mirrored hump towards the positive c_T direction. The temporal nature of this effect is expected to be related to shedding or formation of vortical structures, the exact nature of which is difficult to determine from these force measurements. Interestingly, the 90°α c_T measurements do not oscillate around zero. Oscillations due to a Kármán sheet-like shedding are expected, but these oscillations are expected to be around zero. It could be that the support structure, which is not completely symmetrical over the wing chord (see illustration in Figure 5.5) influences the shedding in such a way that the wing has a different shedding pattern than expected.

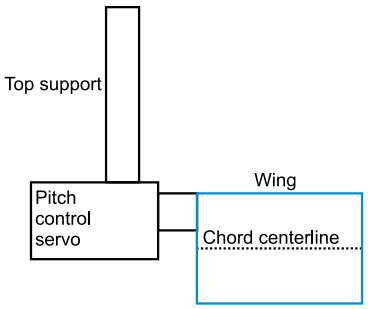

Figure 5.5: Sketch of wing support structure to illustrate the mounting being assymetric over the wing chord, and therefore having a different flow interference effect at the leading edge compared to the trailing edge.

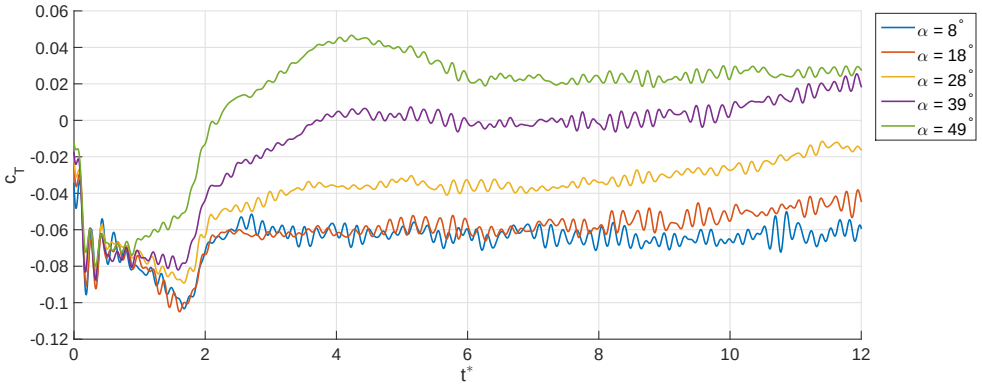

Figure 5.6: DK filtered measured tangential force coefficients (c_T) for 8, 18, 28, 39, and 49°α.

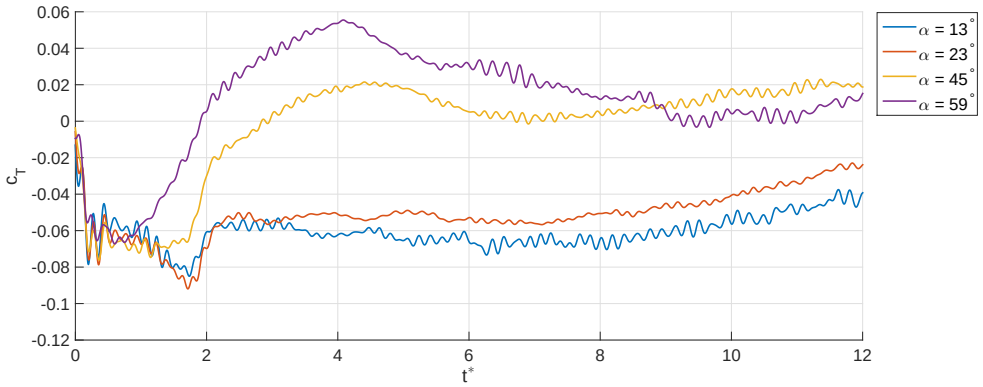

Figure 5.7: DK filtered measured tangential force coefficients (c_T) for 13, 23, 45, and 59°α.

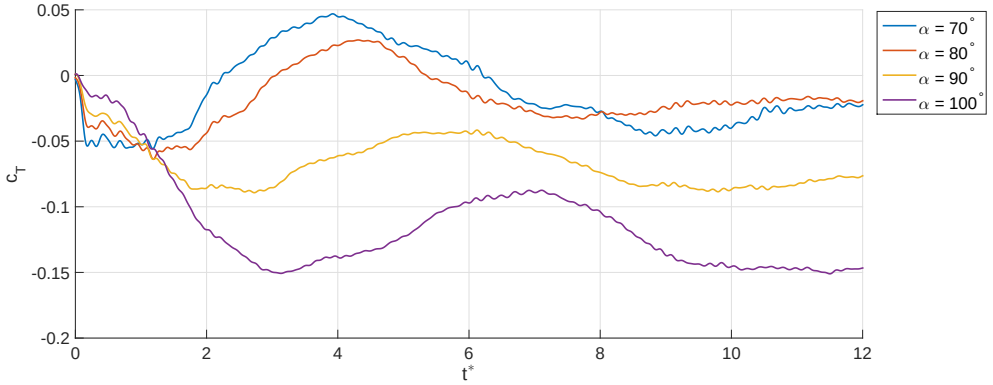

Figure 5.8: DK filtered measured tangential force coefficients (c_T) for 70, 80, 90, and 100°α.

5.1.2. Steady-state forces

Several t* after the acceleration phase of the motion, the forces attain an almost constant value, or 'steady-state' value. This steady-state value is the average measured value from 8 t* to 12 t*, shown for c_N, c_T, c_L, and c_D in Figure 5.9. To facilitate comparison with other literature c_L and c_D values are shown, instead of just the c_N and c_T values. In the Figure, low-order curve fits are presented to investigate a possible simple relationship between angle of attack and steady-state force generation. To achieve a good fit (arbitrarily defined as R^2>0.995), the c_N measurements required a single term sine fit, the c_L and c_D measurements required a two-term sine fit. It is not possible to obtain a good c_T fit, therefore the best attainable fit with a two-term sine fit is used. As the possible explanation can be found in the very low magnitude of the c_T values (note that they are magnified ten times in Figure 5.9), leading to larger measurement uncertainties. The sine fits and associated R^2 values are shown in Equation 5.1.

The observation that a single term sine fit can adequately capture the steady-state normal force is considered a promising indication of the possibility to create a simple steady-state force estimation model, but this is not further explored.

$$\begin{aligned} c_{N_{steady-state}} &= 1.87\sin(1.031\alpha - 0.047) && R^2 = 0.996 \\ c_{L_{steady-state}} &= 0.24\sin(0.286\alpha + 2.756) + 0.882\sin(1.197 + 1.563) && R^2 = 0.995 \\ c_{D_{steady-state}} &= 19.57\sin(0.841\alpha + 1.935) + 18.966\sin(0.866 - 1.143) && R^2 = 0.998 \\ c_{T_{steady-state}} &= 0.093\sin(0.014\alpha + 3.114) + 0.081\sin(0.047 - 1.201) && R^2 = 0.955 \end{aligned} \tag{5.1}$$

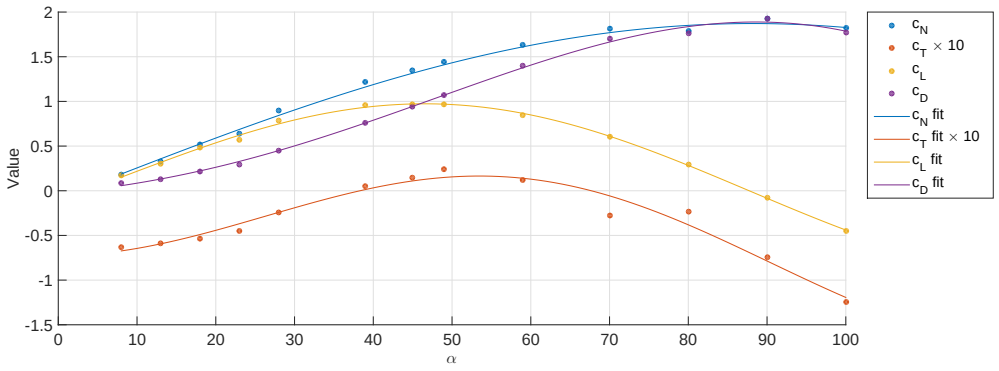

Figure 5.9: Fitted c_N, c_T, c_L, and c_D evolutions compared to measured steady-state values from the revolving-surging experiments. The fits and R^2 values are given in Equation 5.1. Note that the c_T values were multiplied by 10 for clarity.

5.1.3. Force vector angle

To gain more insight in the relation between the normal force and the tangential force, the angle between the normal plane of the wing and the total force vector is computed as in Equation 5.2

$$\text{Force Vector Angle} = tan(\frac{c_T}{c_N})^-1 \tag{5.2}$$

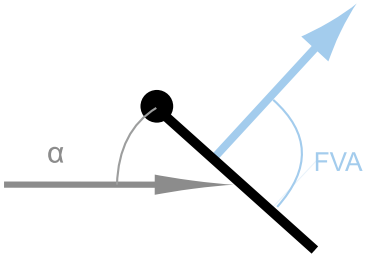

Figure 5.10: Definition of the Force Vector Angle FVA in blue, together with α in grey, and the wing in black, following the convention of Figure 2.1

From this convention, a force vector angle of $0°$ means that the force vector is parallel to the wing, pointing towards the trailing edge, a force vector angle of $90°$ is normal to the chord line, and a force vector angle of $180°$ means that the force vector points towards the leading edge of the wing, parallel to the chord line. This angle is shown in Figure 5.10, together with α.

This angle, averaged over $6\,t^*$ to $8\,t^*$, for the $45°\alpha$ surging experiment is plotted in Figure 5.11, together with the force angle results of Birch et al. [8]. In those experiments, the dynamically scaled wing of a Drosophila Melanogaster was investigated for a revolving-surging motion. The type of motion kinematics is similar to those in the current study although the Re and Ro are different. The Rossby number for the wing under consideration in [8] is 2.9 [41], the Reynolds number 140 (low Re case) and 1200 (high Re case). As can be observed, the force angle coincides reasonably well with the results of Birch et al [8], especially the 'high Re case'. This observation affirms the notion that at high angles of attack, the wing generates mostly normal force. Similar to measurements in this report, Birch et al. observed a positive c_T, as can be seen from the measured force vector angle of greater than $90°$.

In Figures 5.12 to 5.14, the complete force vector angle history over the motion is shown for the revolving-surging experiments. During the acceleration part of the motion, the tangential force is more prominent, although the normal force is still dominant. The force angle therefore points more towards the trailing edge during the start-up phase of the motion. This is shown . At high α, the force vector angle does not change meaningfully during acceleration, but for lower α, the force vector angle starts lower and increases during acceleration as the normal force increases.

Especially for lower α during the start of the acceleration phase, the measurements are noisy, with force vector angle oscillations of up to $20°$ over less than $0.1\,t^*$. This is attributed to the very low force generated, the resulting low SNR, and the division of two measurements, which further decreases the SNR.

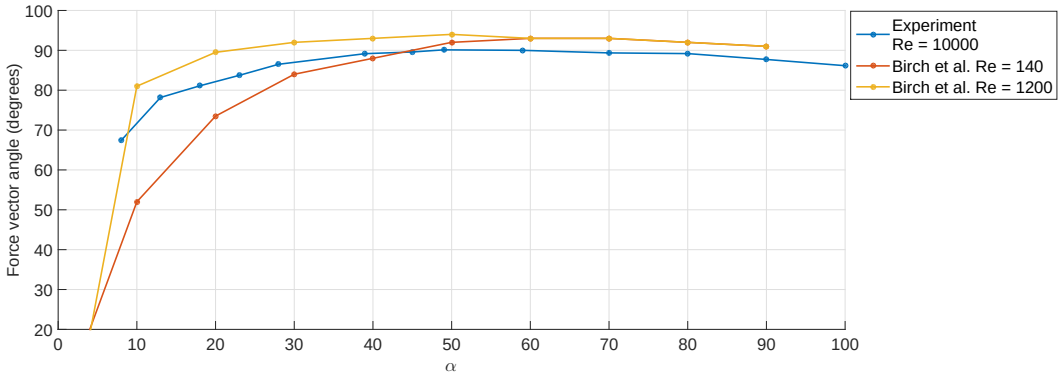

Figure 5.11: Average force vector angles over 6 t* to 8 t*, compared with those from Birch et al. [8].

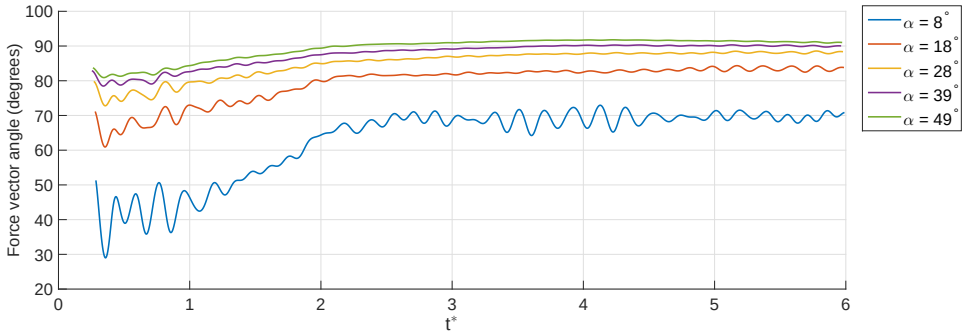

Figure 5.12: DK filtered measured force vector angles for 8, 18, 28, 39, and 49°α.

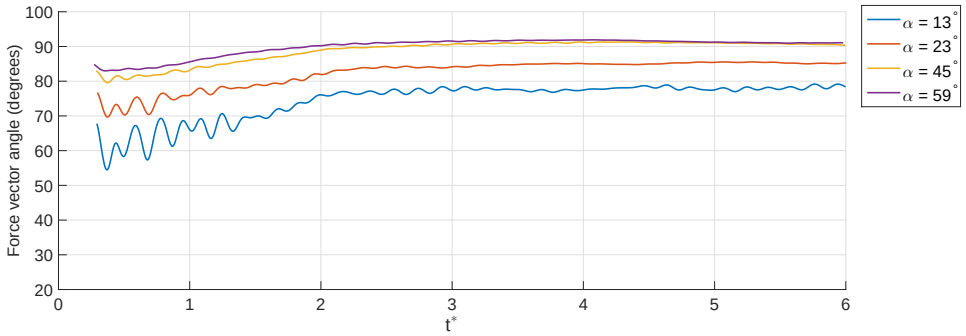

Figure 5.13: DK filtered measured force vector angles for 13, 23, 45, and 59°α.

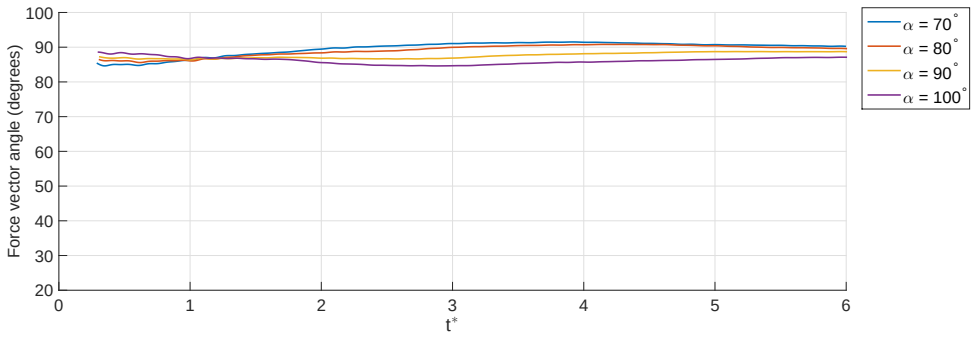

Figure 5.14: DK filtered measured force vector angles for 70, 80, 90, and 100°α.

5.1.4. Center of Pressure

The center of pressure (COP) of the wing is the location on the wing on which the average force vector acts. This is computed by dividing the wing-root bending moment coefficient and the pitching moment coefficient by c_N. This operation does increase the noise of the measurement, as two measurements are multiplied. For the experiment with 49°α the entire time history is plotted in Figure 5.15. For the other time histories, the reader is referred to Appendix A. For the experiment with the wing at 49°α COP starts at a location quite tipward, and then moves inward during the motion. The rootward speed of the COP location is high during the acceleration phase, and is lower afterwards when the wing is revolving at a constant velocity. Even after 5 t*, the COP continues to move rootward, even though the kinematics have been constant for 3 t*, or three chord lengths at the 75% span. The chordwise COP stays relatively constant at around 40% chord. The measured position of the COP is oscillates extensively in the spanwise direction, but not in the chordwise direction.

Figure 5.16 show the location of the COP at the start of the motion (in the middle of the acceleration phase), and at the end of the motion. In general, the lower α experiments have a more tipward COP, both at the beginning and end of the experiment. The experiments with the lowest α even have a COP outside the wing surface at the start of the motion, which would indicate that during the acceleration phase, the wing root generates a negative c_N, however this observation cannot be considered conclusive as the fluiddynamic forces are low, with the c_N less than 0.25. This means that the signal to noise ratio is low as well, and since the COP location computation generates a noisy result as discussed, the measurement error can be very large. The rootward motion of the COP as described for the 49°α case is present for all experiments, with the magnitude of the rootward displacement of the COP more prominent for the lower α experiments. At the end of the experiment, the higher α experiments generally have a more rootward COP location. Curiously, the 45°α measurement seems to be an outlier in terms of COP, where the COP is more tipward over the entire motion, compared to the trend of the other measurements. However, the measured c_N and c_T are not indicative of an outlier. Chordwise, the COP goes from around 25% chord for the 8°α experiment, to around 65 % chord for the 100°α experiment. As also observed for the c_T measurements, the 90°α measurements do not behave as expected. One would expect the COP to be located at the 50% chordwise position, but in contrast, it is located at the 60% position instead.

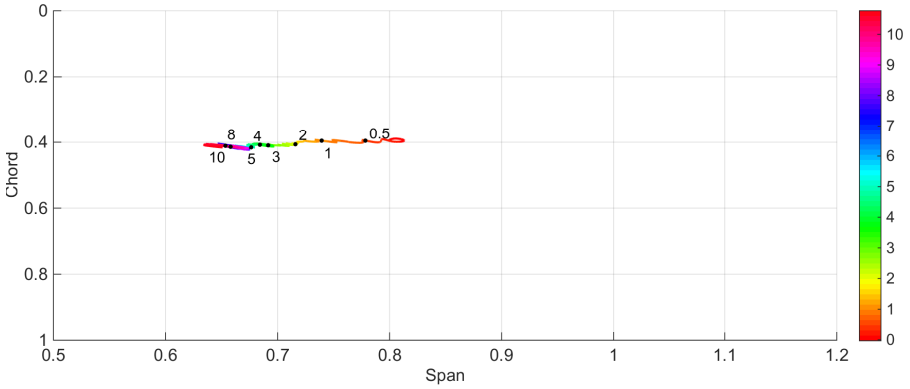

Figure 5.15: Center of Pressure (COP) for the revolving-surging motion of the wing at 49°α. The colorbar signifies the progressing of time in t*, with t* = 0.5,1,2,3,4,5,8, and 10 indicated with black dots. Chord = 0 is at the leading edge, Span = 1 is at the wing tip.

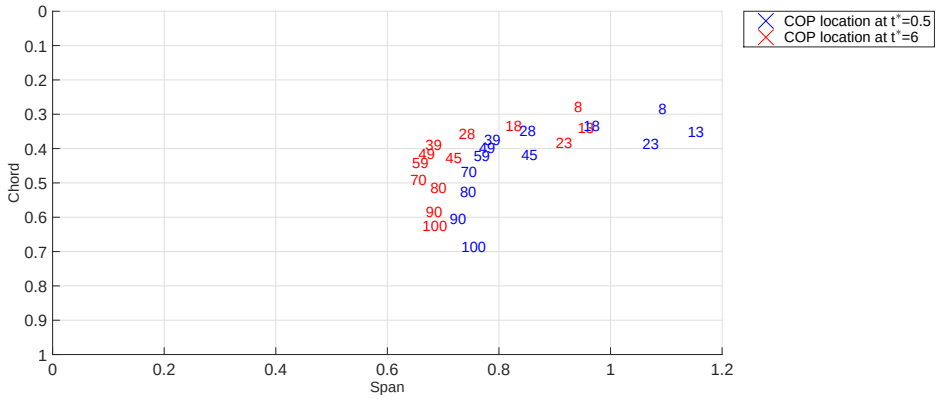

Figure 5.16: Center of Pressure (COP) for the revolving-surging motion of the wing at different α at the beginning of the motion (0.5 t*), and at the end of the motion (6 t*). 0 chord is at the leading edge, 0 span is at the root of the wing. The positions are averaged over 0.2 t*, ie. the shown COP positions for 0.5 t* are the average COP positions between 0.4 t* and 0.6 t* The position of the COP for a given α is shown by the location in the plot of the number equal to α ie. the position of the COP for the wing at 8°α at 0.5 t* is at around 0.29 fractions of chord from the leading edge, and 1.1 fractions of span distanced from the wing root.

5.1.5. Comparison with low-order force estimation models

Steady force

Firstly, it is observed that the generated steady normal force is substantially linear up to around 50°α. This linear relationship is compared to the theoretical c_L of a Prandtl lifting line, corrected for aspect ratio (Equation 5.3) in Figure 5.17. The force measurements performed by of Perçin et al. [52], are also shown in the figure. These measurements were performed on the same measurement apparatus with slightly different kinematics (Ro = 1.8, Re = 20.000 as compared to Ro = 1.65, Re = 10.000 under consideration). As the kinematics were different, the root-relative c_N was used (as discussed in 3.3 and [5]). Detailed information on the Prandtl lifting line theory can be found in many textbooks, such as [2]. It can be observed that there is a good agreement between the measured normal force and lifting-line *lift* force, up to around α =55°. The experimental results from [52] display the same match, indicating that the match is likely not out of mere coincidence. This agreement is unexpected as the lifting line model in general is only suited for a prediction of the lift of a wing at small angles of attack, under attached-flow conditions. In this case, the normal force for a wing at high α, under separated-flow conditions seems to be predicted rather accurately. A possible explanation can be found in that both the normal force in the measurements is close to the total force vector (as the tangential force is close to zero), while the lifting line theory also aims to predict the total lift force as the predicted drag force is zero for a potential flow solution such as the lifting line.

$$c_L = \frac{a_0}{\sqrt{1 + (\frac{a_0}{\pi AR})^2} + (\frac{a_0}{\pi AR})}\alpha \text{ with } a_0 = 2\pi \tag{5.3}$$

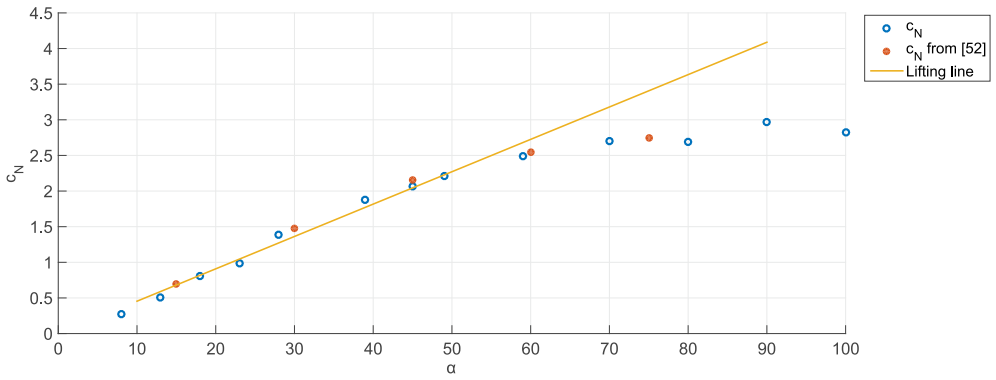

Figure 5.17: Normal force coefficients compared to theoretical lifting-line lift coefficients and the normal force coefficients of [52]. All coefficients shown are calculated with the reference velocity at the radius of gyration.

Forces during acceleration

The quasi-steady force estimation model as discussed in Chapter 2 is utilized to estimate the unsteady forces generated by the revolving wings. To implement this model, the motion data is filtered mainly to obtain a physically representative motion without discontinuities in the velocity, acceleration, and jerk (third derivative of the position). The smoothing function used is the C^∞ function decribed by Eldredge et al. [21], as also used in [25]. For the revolving-surging motion, a smoothing factor a_{sm} of 100 was used as in [21]. The amount of smoothing is determined heuristically, and to quantify the magnitude of smoothing, the drop-off in generated force at the end of the acceleration phase is intended to take 0.1 t*, instead of being discontinuous. F_{steady} as described in Equation 2.9 is obtained by using the function fitted to the steady c_N measurement data from Figure 5.9.

As the normal forces as shown in Figures 5.3 to 5.4 display similar behaviour, so do the quasi-steady estimations, only the 18, 28 ,45; , and 70°α cases are compared to the quasi-steady model. This is shown in Figure 5.18.

In general, the quasi steady model matches qualitatively with the measured force, especially during the acceleration phase. There are differences in the force signal shape at the start- and endpoints of the acceleration phase. At the start of the acceleration phase, there is a slight peak for larger angles of

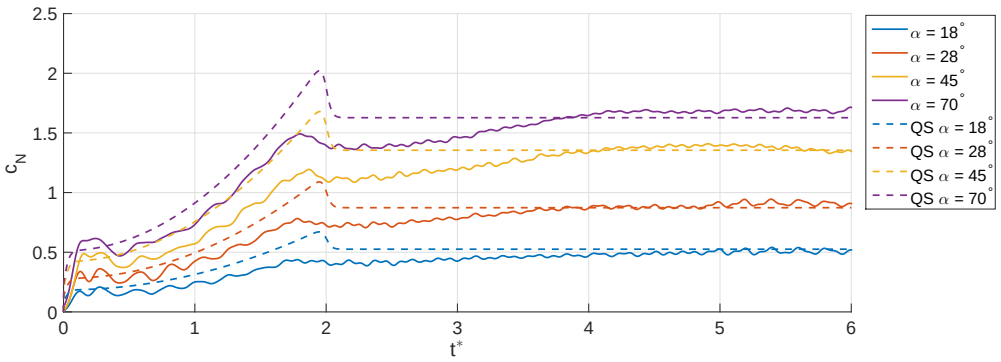

Figure 5.18: DK filtered measured normal force coefficients, compared to quasi-steady estimations for 18, 23, 45, and 70°α

attack, absent in the quasi-steady model. At the end of the acceleration phase, the observed leveling off of the force rise for the measurements is not present for the quasi-steady model, and therefore the generated force peak at the end of the acceleration is much lower than predicted by the quasi-steady model. Also, the quasi-steady model predicts that the force immediately reaches the steady force when the acceleration phase is over. The steady force in the quasi-steady model is the circulatory force component. In the experiments, this force generation mechanism is very time dependent, taking several t* to build up, and even builds up past the 'steady' value for the higher α experiments (the observed 'hump').

The quasi-steady model suggests that the magnitude of the initial force peak should rise with the sine of the angle. This is checked by comparing the mean, normalized value between 0.1 t* to 0.3 t* to the sine of the angle in Figure 5.19. It is observed that there is a good match between the measurements above 23°α and the expected trend, indicating that the expected 'added mass' force term is quite accurate. For comparison, the height of the force peak estimated by the quasi-steady model is also shown (in relative magnitude of the measured peak), which lags the measured force. It is observed that the 'added-mass' force is highest between 0.1 t* to 0.3 t*, and then drops slightly. This drop is up to 0.05 c_N for the higher α measurements, and lower for the others. The predicted added-mass force augmentation stays constant until around 1.85 t*.

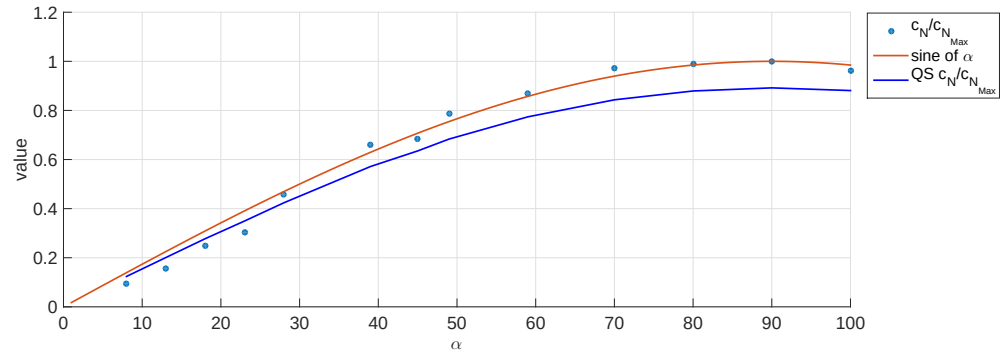

Figure 5.19: Normalized c_N average during the initial peak (0.1 t* to 0.3 t*), compared to sine of the angle and the normalized c_N suggested by the quasi-steady (QS) model. $c_{N_{max}}$ at α = 90°.

Quantitatively, the generated force lag the quasi-steady model significantly during most of the acceleration phase, save for the very start. A possible explanation can be found in the location of the (center of pressure) (COP). As the quasi steady model assumes a constant c_N, and the velocity profile over the wing is linear, the quasi-steady model considers the wing to have a COP is at 61% of the span.

However, the measurements show a COP more towards the tip of the wing. This could indicate that the rootward part of the wing generates much less force than predicted by the quasi-steady model.

5.1.6. Measurement uncertainty

As the experiments are repeated multiple times, the standard deviation σ is computed for each measurement point. This standard deviation is averaged over the 0 t* to 6 t* to find the average σ for each experiment. The average width, in c_N, of the 95% confidence interval is then $2\sigma/\sqrt{N}$ where N is the number of experiments. The derivation of this can be found in literature on statistical analysis such as [55]. It should be noted that uncertainty analysis does not take into account any systematic errors. The 95% interval is shown in percentage of the mean measured c_N to give insight in the relative uncertainty. These uncertainties are similar to those reported in [49], except for the lower angles of attack where the relative uncertainties are higher as the force magnitudes are much lower. As can be observed, the DK-filtered forces have a lower confidence interval, showing that the DK filter helps in decreasing the random error in the force measurement data.

Table 5.1: Uncertainty estimates on the normal force coefficient c_N (95% confidence interval) for the differently filtered signals, in $c_N \times 100$

	c_N uncertainty		
	Ensemble	Denoised	DK
8°α	13.0	1.2	0.7
13°α	10.9	1.7	1.0
18°α	7.3	1.5	0.8
23°α	5.3	1.4	0.7
28°α	7.1	1.6	0.5
39°α	6.6	1.5	0.6
45°α	4.6	2.0	1.1
49°α	9.6	4.8	1.2
59°α	7.0	1.6	0.7
70°α	7.9	2.4	0.9
80°α	7.0	3.0	2.6
90°α	10.3	3.6	1.3
100°α	5.5	2.0	1.6
Average	7.9	2.2	1.1

It can be observed that the raw measurements have a substantial uncertainty of up to 0.79 c_N, compared to a α = 45° steady c_N value of around 1.35. However, 50 Hz filtering has a substantial effect, decreasing the uncertainty window to almost a quarter of that. This was expected from the Welch's PSD estimates from 3.3, where it was observed that there was information at very specific frequencies that were too narrow to have an obvious fluid-dynamic or mechanical source. This indicates a noise source, which would increase the uncertainty. DK filtering further decreases the confidence interval. Again, this is expected as the magnitude of the force peaks measured during acceleration is decreased by the DK filtering and as such, the magnitude of the uncertainty interval will decrease similarly.

5.2. Revolving-Pitching Results and discussion

5.2.1. Evolution of unsteady forces

As discussed in Chapter 2, the total unsteady normal force for the case of revolving-pitching wing consist of added mass forces due to the pitching acceleration, additional circulation due to the pitching motion, and a build up of leading edge vorticity. The experiments were done at varying pitching axis locations ($\hat{x}_0$), and varying pitch rates (k). The first set of figures (5.20 to 5.23) show the c_N evolution for varying $\hat{x}_0$ at a fixed k, for the period of motion until a steady state force is obtained. Figure 5.24 shows the c_N evolution for a varying k at a fixed $\hat{x}_0$ = 0.88. Other figures directly comparing the forces at a fixed $\hat{x}_0$ and a varying k are shown in Appendix B.

The time histories for the normal force coefficients display a similar trend. The force history starts with a peak as the wing undergoes a pitching acceleration, then displays a linear rise in generated normal force as the wing is rotating and attains higher α, followed by a peak in the opposite direction of the first peak as the wing experiencese a reversed pitching acceleration to stop rotating. The width of these peaks does not seem to be not related to k. Interestingly, the force peak lags the timing of the pitching acceleration (compare to Figure 3.5) around 0.4 t*. This time lag is consistent for all experiments, and not related to k. The peak height is also observed to be related to pitching axis location. The experiments with $\hat{x}_0$ = 0.5 show no prominent peaks associated with the phases of pitching acceleration, with the other experiments showing peak sizes, and indeed the force generation during the pitching phase, almost linearly dependent on pitching axis location. This is shown in Figure 5.20, where the $\hat{x}_0$ = 0.25 and $\hat{x}_0$ = 0.75 force histories are shown to be reasonably predicted from linear interpolation between the experiments at other $\hat{x}_0$, although the $\hat{x}_0$ = 0.25 force history is overestimated. After the pitching phase, the experiments with a lower $\hat{x}_0$ (i.e. the cases with the pitching axis location closer to the leading edge) generate a slightly higher c_N. This is surprising as the motion at this point in time is the same. The increased force production by the lower $\hat{x}_0$ cases could either be explained by flow effects which persist for a long time, but also by the different proximity of support structures of the experimental setup. When the pitching axis location is changed, the wing is mounted at another location (observe Figures 3.3 and 5.5). The different proximity of the support structure could be of influence on the result.

The experiments with decreasing k, having lower pitching velocity, generate lower forces during the pitching phase, with similar forces after the pitching phase. The qualitative traits as mentioned are still present.

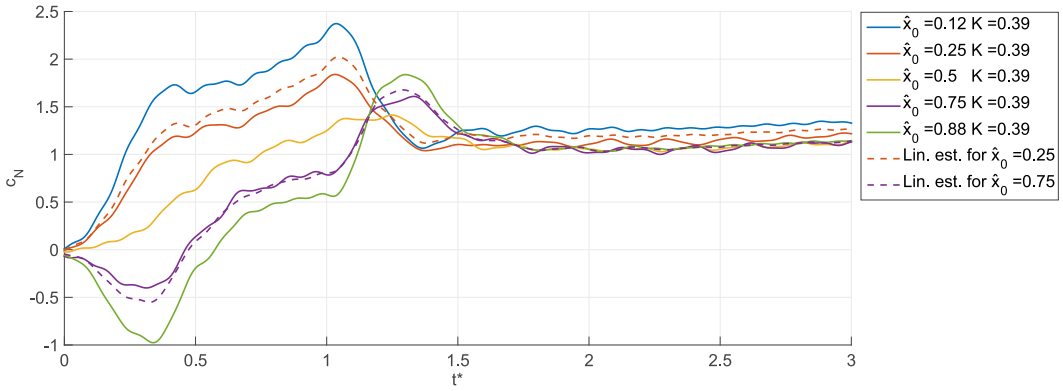

Figure 5.20: DK filtered measured normal force coefficients for revolving-pitching measurements with $\hat{x}_0$ = 0.12, 0.25, 0.5, 0.75, 0.88, k = 0.39, with linear estimates for the $\hat{x}_0$ = 0.25 and $\hat{x}_0$ = 0.75 cases.

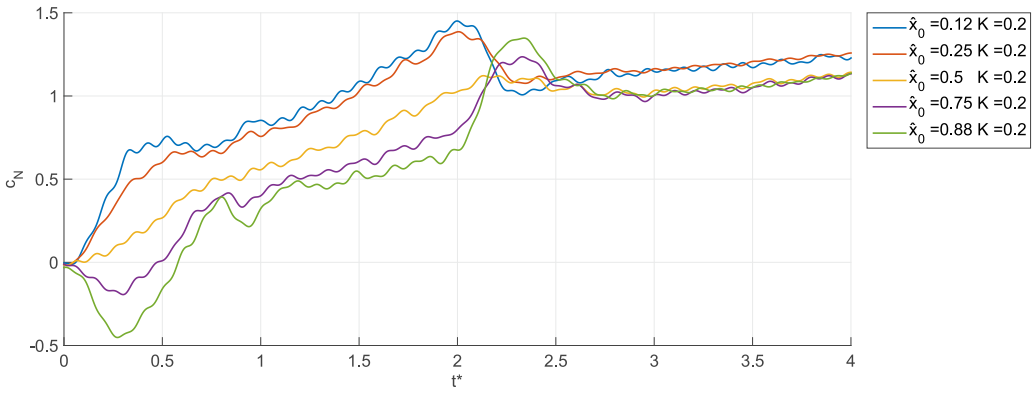

Figure 5.21: DK filtered measured normal force coefficients for revolving-pitching measurements with $\hat{x}_0$ = 0.12, 0.25, 0.5, 0.75, 0.88, k = 0.2.

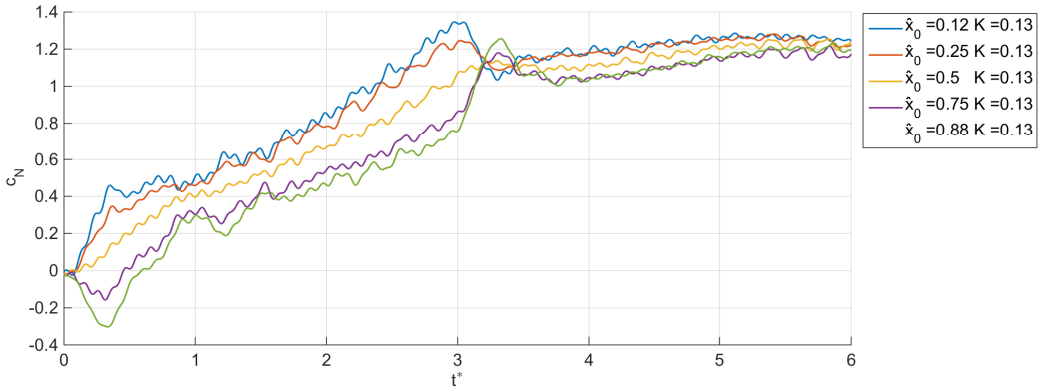

Figure 5.22: DK filtered measured normal force coefficients for revolving-pitching measurements with $\hat{x}_0$ = 0.12, 0.25, 0.5, 0.75, 0.88, k = 0.13.

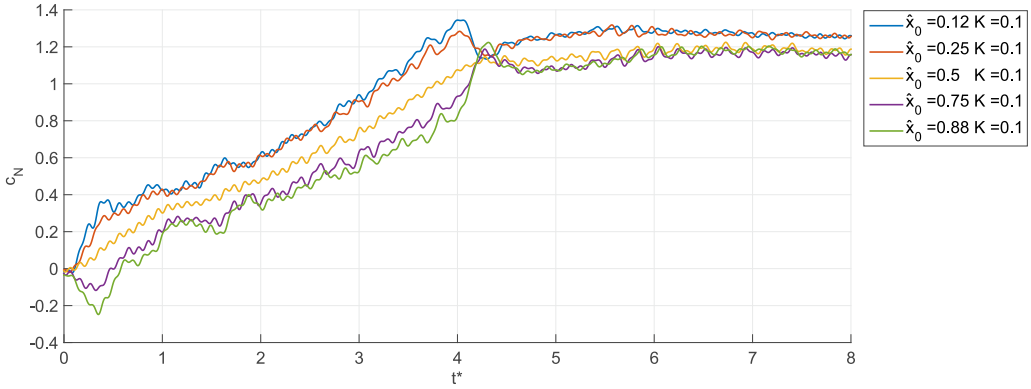

Figure 5.23: DK filtered measured normal force coefficients for revolving-pitching measurements with $\hat{x}_0$ = 0.12, 0.25, 0.5, 0.75, 0.88, k = 0.1.

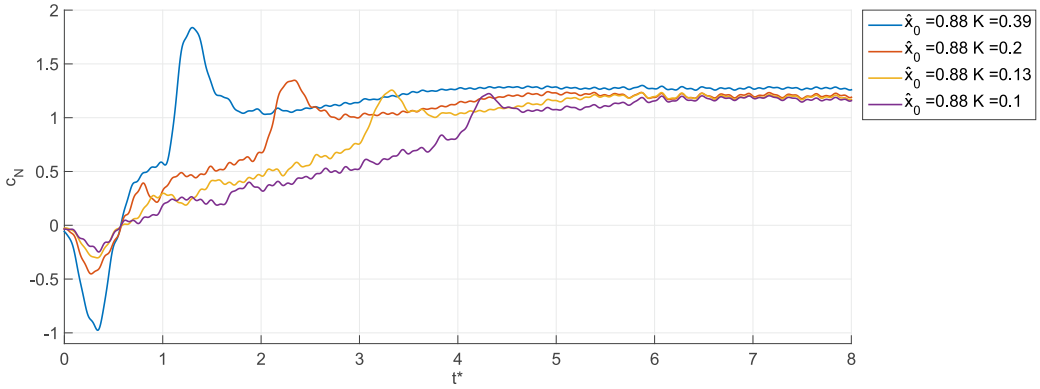

Figure 5.24: DK filtered measured normal force coefficients for revolving-pitching measurements with $\hat{x}_0$ = 0.88, k = 0.39, 0.2, 0.13, 0.1

The c_T force histories are shown for k = 0.39 and k = 0.1 in Figures 5.25 and 5.26. As the generated c_T is low in general, it is difficult to find clear traits when the measurement uncertainty is taken into account. The traits that can be observed are similar for all experiments, as is the case for the c_N measurements. The most interesting trend is that both the acceleration and deceleration of the pitching motion give rise to a positive tangential force (towards the leading edge of the wing). This is more pronounced for the experiments with a higher pitching rate. For those experiments with the pitching axis more towards the trailing edge, a high tangential force peak appears at the beginning and end of the pitching periods. For the lower pitching rate shown, the c_T is almost constant after the initial pitching acceleration phase is over (the same 0.4 t* as also observed for the c_N values), and also almost completely independent of $\hat{x}_0$. Other revolving-pitching c_T force histories are shown in Appendix B.

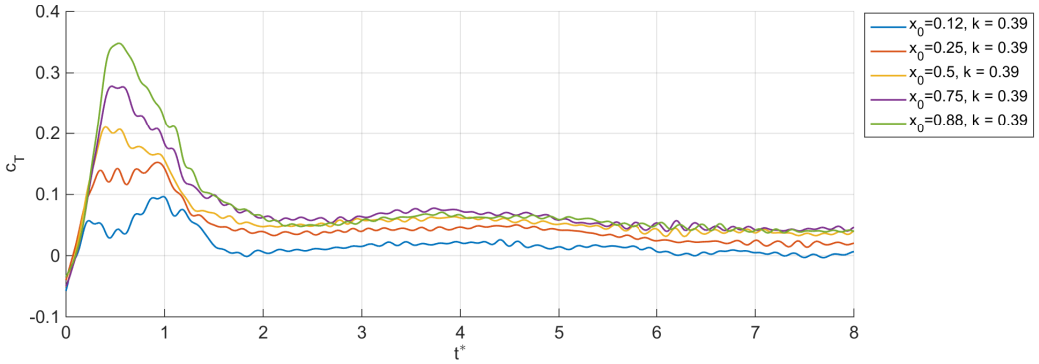

Figure 5.25: DK filtered measured tangential force coefficients for revolving-pitching measurements with $\hat{x}_0$ = 0.12, 0.25, 0.5, 0.75, 0.88, k = 0.39.

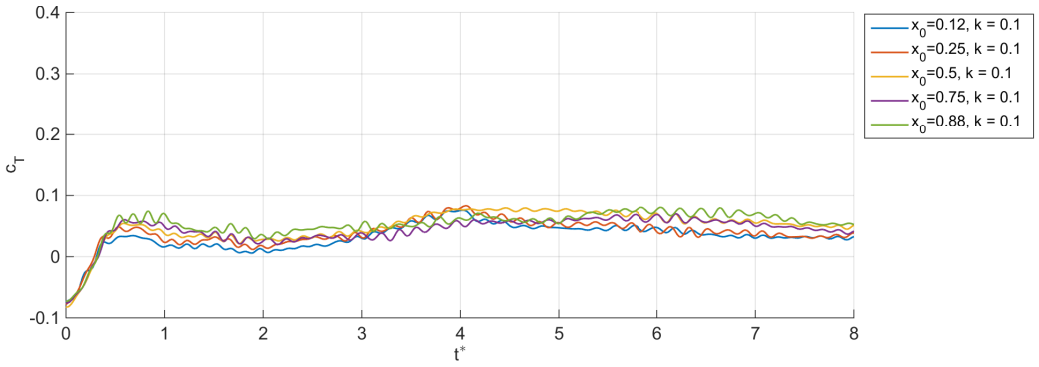

Figure 5.26: DK filtered measured tangential force coefficients for revolving-pitching measurements with $\hat{x}_0$ = 0.12, 0.25, 0.5, 0.75, 0.88, k = 0.1.

5.2.2. Force vector angle

The force vector angle is more easily interpreted as the force histories are less noisy. The downside is that the experiments with a pitching axis location more towards the trailing edge have times where the c_N goes from negative to positive, which causes asymptotic peaks due to the tan^{-1} operation. Therefore, only the force vector angles of the $\hat{x}_0$=0.12 experiments are plotted in Figures 5.27 and 5.28. In the second picture, the time is normalized by multiplying the time vector by k/k_{max} to accurately differentiate which force effects are dependant on wing pitch angle, and which force effects are dependent on t*. After the pitching phase, convective time shows to be the more dominant time scale as the force vector angles match up better. A 'double hump', with the first hump at at 0.2 t^*_{norm} and the second at 1 t^*_{norm} can be discerned in the force vector angle plots, and this is clearly an effect which depends on the pitching position instead of convective time.

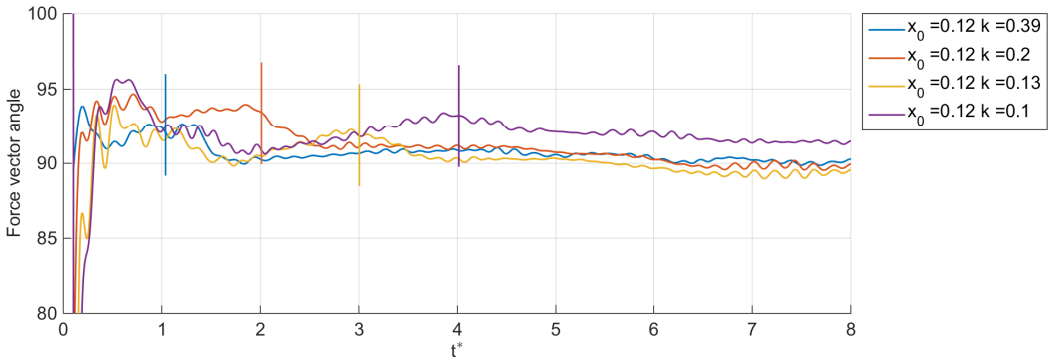

Figure 5.27: Force vector angle for $\hat{x}_0$ = 0.12, k = 0.39, 0.2, 0.13, 0.1. Vertical lines show where the pitching motion ends.

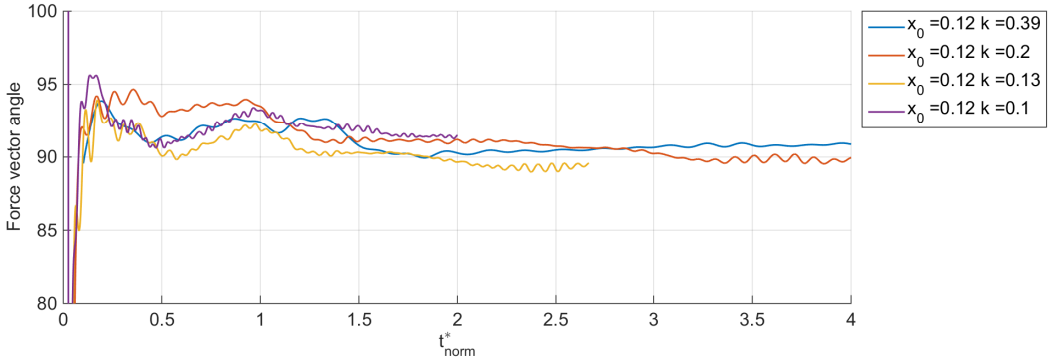

Figure 5.28: Force vector angle for $\hat{x}_0$ = 0.12, k = 0.39, 0.2, 0.13, 0.1. against a normalized time (t^*_{norm} = t* × k/k_{max}). Pitching motion ends at t^*_{norm} = 1.

5.2.3. Center of Pressure

For the revolving-pitching experiments, the COP is computed in the same way as for the revolving-surging experiments. As with the force vector angle, the COP trajectory is difficult to interpret for those experiments with a negative or very low c_N. For the $\hat{x}_0$ = 0.12, k = 0.39 experiment, the complete COP location history is shown in Figure 5.29. The other COP histories for revolving-pitching experiments are shown in Appendix B. It can be observed that the COP location is quite noisy, but trends are observable. Regarding the spanwise position of the COP, the trend is that the COP stays at a relatively constant position of around 0.95 span during the pitching phase of the motion. After the pitching phase, the COP stays at the same spanwise position for around 0.4 t*, mirroring the timing of the c_N measurements. The COP then moves towards the root of the wing. In terms of chordwise COP position during the pitching phase, the COP moves from the trailing edge towards the leading edge of the wing. After the pithing phase, the chordwise position of the COP stays relatively constant. This gives an interesting contrast, where the COP moves predominantly chordwise during the pitching phase of the motion, and predominantly spanwise during the steady-state phase of the motion.

What can be concluded is that just after the pitching phase, between 1 and 2 t*, a lot of flow phenomena are taking place. The c_N goes from around 2.3 to 1, to 1.2, the force angle goes from 92° to 90°, and the COP moves around half a chordlength in total displacement.

The other experiments at $\hat{x}_0$ = 0.12 are represented in terms of start- (1 t*) and end (6 t*) COP in Figure 5.30, similar to Figure 5.16. For the lower pitching rates, the COP starts outside the physical surface of the wing, much like the lower α revolving-surging experiments.

The final positions of the COP for all experiments are shown in Figure 5.31, together with the COP

location of the α = 45° revolving-surging experiment. This affirms the notion of significant differences between the experiments at different $\hat{x}_0$, even long after the actual pitching phase; the COP's of the experiments with a higher $\hat{x}_0$ are more towards the leading edge by up to 0.3 chord lengths. A relation between pitching axis location and a more leading-edgeward location of the COP is observed. There is also a weak relation between a higher k and a more rootward position of the COP endpoint, but this does not hold true for all experiments.

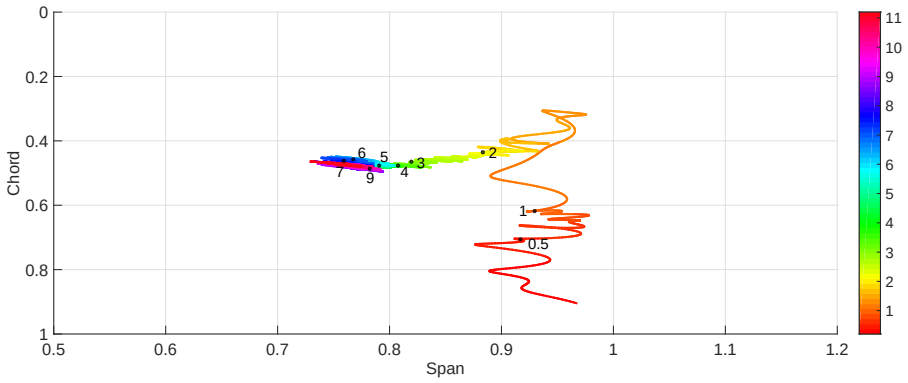

Figure 5.29: Center of Pressure location for entire motion for $\hat{x}_0$ = 0.12, k = 0.39.

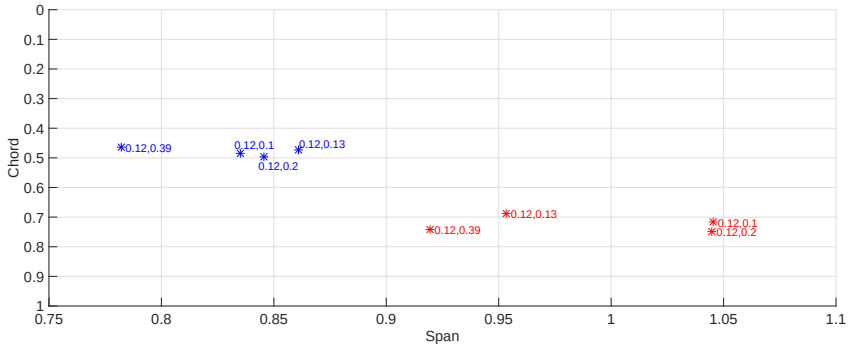

Figure 5.30: Center of Pressure location at the beginning 1 t* (red) and end 6 t* (blue) of the motion for $\hat{x}_0$ = 0.12 k = 0.39, 0.2, 0.13, 0.1.

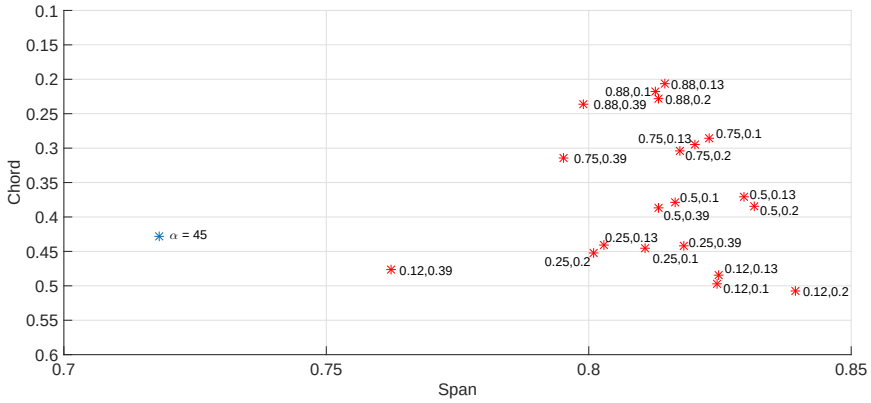

Figure 5.31: Center of Pressure location at end of steady motion (mean of 7.5 t* to 8.5 t* for all revolving-pitching measurements. Red dot is the endpoint, Format given is in ($\hat{x}_0$,k). The blue dot is the end point of the COP of the surging motion at 45°α

5.2.4. Comparison with revolving-surging experiments

In Figure 5.32, the revolving-surging experiment at α = 45° is plotted together with the extremes of the parameter space for the revolving-pitching experiments (those with $\hat{x}_0$ at the lowest and highest value, and k at the lowest and highest value). Note that at the end of the motion, the kinematics are the same, revolving at 0.2 m s^{-1} at α = 45° . The differences in generated force are of interest as they give an insight in the interaction between the different force augmentation mechanisms. Interestingly, the differences are pronounced, even after several t* after the pitching or surging parts of the motion. At t* = 3, the revolving-surging experiment generates Δc_N = 0.15 less than the revolving-pitching experiment ($\hat{x}_0$ = 0.12, k = 0.39), but at 8 t*, the revolving-surging experiment shows a higher force generation of around Δc_N = 0.08. Similar differences exist between the different experiments, with the revolving-pitching experiments for a lower k and higher $\hat{x}_0$ generating lower c_N values. As shown in Chapter 5.1.6, the measurement uncertainty is around Δc_N = 0.01, hence lower than the reported differences in generated force for the constant phase of the motion.

The inverse is true for the for the c_T values as shown in Figure 5.33. The experiments that show relatively lower c_N at the end of the motion show relatively higher c_T values. However, although the relative differences are there, the absolute differences are smaller. The total range of c_T values at the end of the motion in figure 5.33 is around 0.05, the total range of c_N values in Figure 5.32 is around 0.2. As the trend holds true for the range of experiments, the observation is still considered valid, even though the differences in the c_T experiments are at the same order of magnitude as the measurement uncertainties mentioned in Table 5.2.

Interestingly, the similar experiments by Perçin et al. ([49]) show slightly different results. During the unsteady phase of the motion, the revolving-surging experiment consistently lags the revolving-pitching experiment in terms of c_N, with a good match during the steady-state part of the motion. Also, the c_T is negative for all experiments during the steady-state part, instead of positive as in the current investigation. The reported differences are expected to stem from the slightly different kinematics.

When comparing the COP locations for both types of experiments (Figure 5.31), it is observed that the COP is more rootward for those cases that generate higher normal forces at the end of the motion. For instance, the $\hat{x}_0$ = 0.12, k = 0.39 experiment has a COP around 0.05 span more rootward $\hat{x}_0$ = 0.88, k = 0.1, and generates around 0.13 c_N more at t* = 8. However, the spanwise difference in COP is the same between the $\hat{x}_0$ = 0.13, k = 0.39 and $\hat{x}_0$ = 0.39, k = 0.1 cases, with a much less pronounced c_N difference (0.05 c_N). The COP for the surging experiment is between 0.04 and 0.12 span more rootward than the pitching experiments. As the COP is more rootward, and the total force generation higher, this indicates an increased c_N- generating performance of the wing root compared to the wing tip.

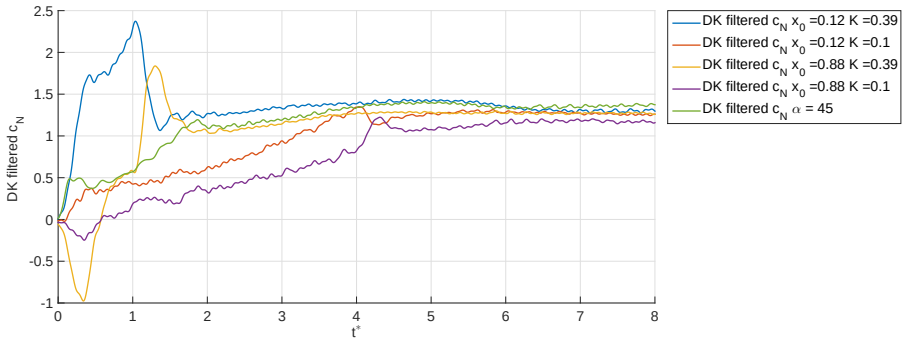

Figure 5.32: Normal force histories of revolving-surging experiment at 45°α and revolving-pitching experiments at $\hat{x}_0$ = 0.12 and $\hat{x}_0$ = 0.88 and k = 0.39 and k = 0.1

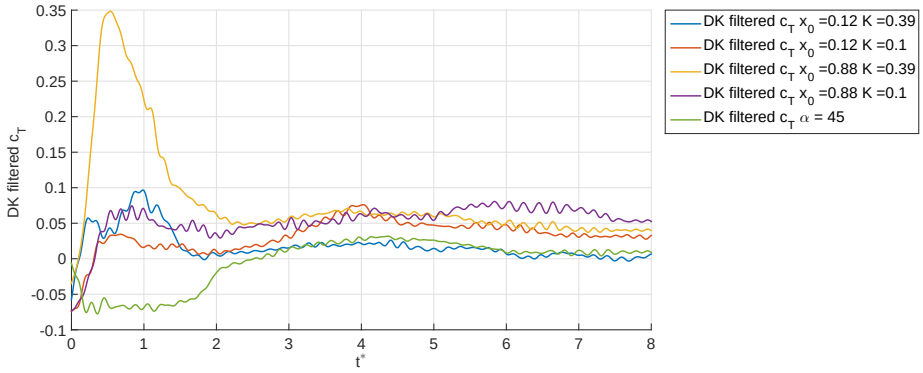

Figure 5.33: Tangential force histories of revolving-surging experiment at 45°α and revolving-pitching experiments at $\hat{x}_0$ =0.12 and $\hat{x}_0$ =0.88 and k = 0.39 and k = 0.1

5.2.5. Comparison with quasi-steady model

As in Chapter 5.1, the quasi-steady model is used for the estimation of the forces and the results are compared with the measured forces. In [58], the quasi-steady model was only suitable for pitching motions around the leading edge. As the experiments performed rotate around other axes than the leading edge, Equation 2.10 for $F_{addedmass}$ needs to be modified. It is observed that the estimated added-mass force generation is the same either the wing rotates around the leading edge or the trailing edge, but the direction of the force vector is reversed. Furthermore, the added-mass force generation should be zero if the wing is rotated around the half-chord axis as the front half of the wing mirrors the aft part of the wing. Therefore, in the scope of the quasi-steady model, linear interpolation suffices, and Equation 2.10 is modified to Equation 5.4. Note that the changes only influence the second term.

$$F_{addedmass} = \rho\frac{\pi}{4}c^2\ddot{\phi}\sin\alpha\int_{r_{root}}^{r_{tip}} r\,dr + (0.5-\hat{x}_0)\rho\ddot{\alpha}\frac{\pi}{4}c^3 b \tag{5.4}$$

As with the revolving-surging motion, the motion kinematics are smoothed. Accurate motor feedback position data is available for the revolving motion, but not for the pitching motion. Therefore the measurements are used as a guide to determine the motion input to the quasi-steady model. The smoothing term a_{sm} in the C^∞ equation is used to match the resulting quasi-steady force estimation to the measured force, where the smoothing term is chosen such that the width of the first peak of the measurements at $\hat{x}_0$, k = 0.39 matches the width of the first peak of the quasi-steady force estimation. For a_{sm} = 40, the results are determined to be acceptable.

Added mass force

In Figure 5.34, the c_N for the pitching experiments for $\hat{x}_0$ = 0.12, 0.5, 0.75, and 0.88, k = 0.39 are compared to the forces expected with the quasi-steady model. In terms of force generation in the steady part of the motion, the quasi-steady model suggests the same force for all the experiments, as the steady force is assumed to be only dependent on α. This suggestion does not hold true, but the differences are slight. The quasi-steady model further suggests that the added-mass force cancels out for $\hat{x}_0$ = 0.5, which shows in the quasi-steady force prediction as no peaks at the start and end of the pitching phase. This hypothesis holds, which can be evidenced from the experiments at x_0 = 0.5. For the experiments with different $\hat{x}_0$, the added mass force can be described as quantitatively correct, as the measurements show much lower magnitude force peaks. However, it is difficult to ascertain how much the quasi-steady model misrepresents these force peaks as the peak height also depends on the heuristically determined a_{sm} value.

Rotational force

The other term in the quasi-steady model is the force augmentation due to increased circulation associated with the pitching velocity. It is difficult to obtain a clear estimation of this force in the measurements, as the force peaks associated with the pitching acceleration lag the actual pitching acceleration. However, from observing the $\hat{x}_0$ = 0.88, k = 0.1 experiment in Figure 5.32, there is a clear 'flat spot' between a negative and a positive force peak, for 0.7 t* to 1 t*. As the force peak widths are not related to pitching rate (see Figure 5.24), the peaks are considered not purely related to pitching rate, leaving the 'flat spot' as the part of the force history in which there is the highest confidence that the generated force is predominantly related to pitching rate. This flat spot shows a slight rise in magnitude over time, which coincides with the notion that the force should consist of a component associated with α, and a constant component associated with pitch rate. The positive and negative force peaks themselves are attributed to pitching acceleration. As discussed, the pitching motor lacks feedback, however, the width of the peak is much wider than expected, as this would imply that for the experiments at k = 0.39, the actual k can not be considered constant over the motion. This would also imply the pitching motor has an angular acceleration of around $2 \times 10^1\ rad/s^2$ (pitch rate of $\pi\ rad/s$, 1 t* = 0.25s for the motion under consideration), which seems a very low figure. A potential 'smearing' on these pitch acceleration peaks due to the DK filter cannot be ruled out in this instance, however, if this were to be the case, the DK filter would have a larger 'smearing effect' for the experiments with a higher pitch rate. However, the experiments at a lower pitch rate show a very similar peak width, which would imply a larger smearing effect, for a smaller disturbance. Therefore, the most likely explanation seems to be a fluid-dynamic damping effect, or simply that the pitching motor control does indeed not reach more than the reported pitching acceleration.

In Figure 5.34 the magnitude of the forces predicted by the quasi-steady model are higher than the measured forces for the $\hat{x}_0$ = 0.12, 0.5, and 0.75 experiments, and lower for $\hat{x}_0$ = 0.88. The difference for the $\hat{x}_0$ = 0.12 experiment is especially large, around Δc_N = 1. The quasi-steady model predicts a zero force augmentation when $\hat{x}_0$ = 0.75. To determine if $\hat{x}_0$ = 0.75 indeed leads to a zero force augmentation in the experiments, the different pitching experiments are plotted for a normalized t* (the same normalized t* as also used in Figure 5.28) in Figure 5.35. If the pitch rate influence is indeed zero, the force between the normalized convective times 0.7 t* to 1 t* should be the same for k = 1 through 4, as the wing is at the same α, moving at the same velocity, without any expected force generation effects other than those related to angle of attack and revolving velocity. For $\hat{x}_0$ = 0.75, this seems the case, which agrees with the notion in the quasi-steady model, and also agrees with the experiments from Grandlund et al. [25], Sane et al. [58], and Dickinson et al. [18].

As the $\hat{x}_0$ = 0.75 experiments give a result that has almost zero force augmentation by pitching velocity, it is possible to estimate the pitching velocity force augmentation effects for the other experiments. This can be compared between the different pitching rates. The quasi-steady model suggests a linear increase in force for an increase in pitching rate. This is checked by comparing the mean value of the experiment at a given $\hat{x}_0$, minus the measured force of the same experiment at $\hat{x}_0$ = 0.75 over 0.7 t* to 1 t^*_{norm} (this time range as discussed in the previous paragraphs). If the results are indeed linear,

the mean value over this normalized time span, divided by the pitching rate k should be the same, and the lines in Figure 5.36 should then be straight. As this is clearly not the case, the force augmentation due to pitching velocity can not be described as linear with respect to pitch rate. The lines do not show a straightforward relation between pitching rate and force augmentation, which hints at complex flow phenomena.

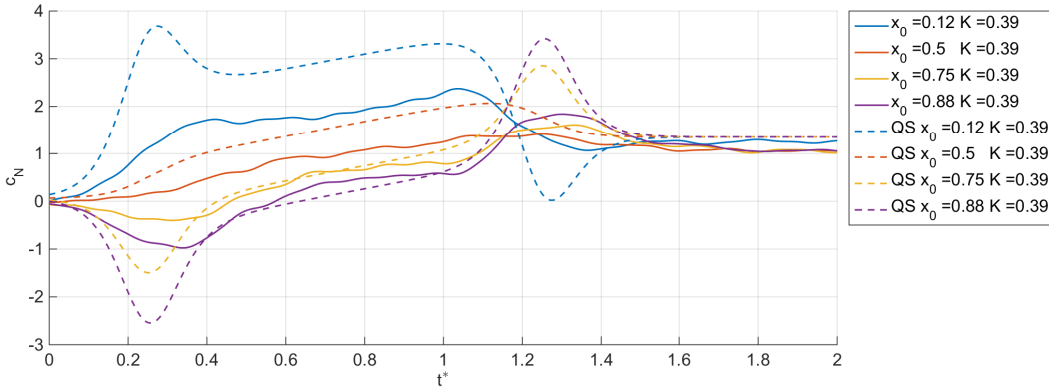

Figure 5.34: DK filtered measured quasi-steady model expected normal force coefficients for revolving-pitching measurements with $\hat{x}_0$ = 0.12,0.5, 0.75, 0.88, k = 0.39.

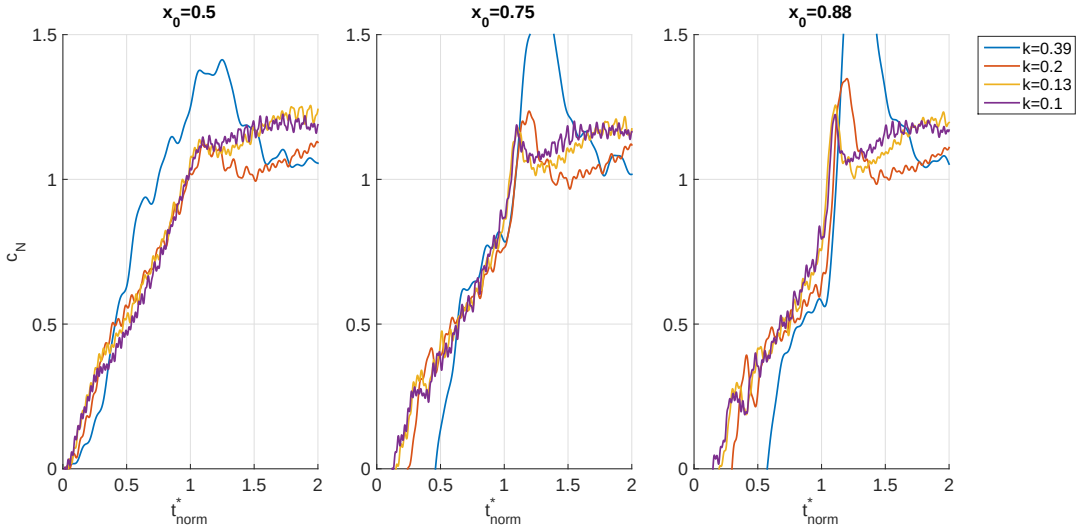

Figure 5.35: DK filtered measured normal force coefficients for $\hat{x}_0$ = 0.5, 0.75, 0.88, k = 0.39, 0.2, 0.13, 0.1 against a normalized time (t^*_norm = $t^* \times k/k_{max}$).

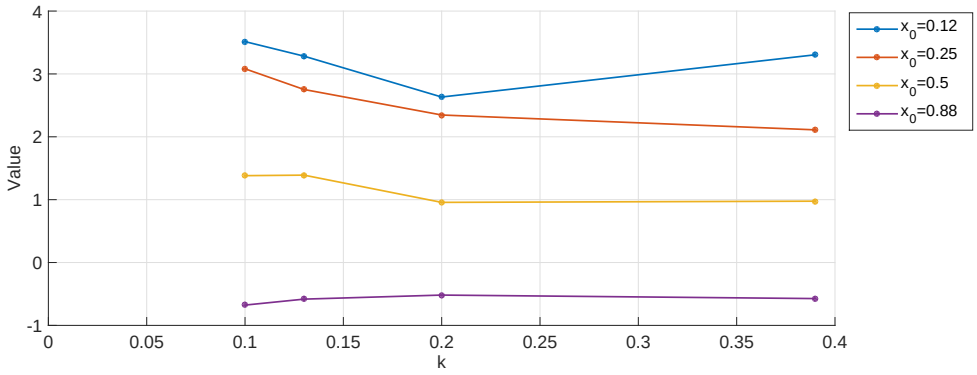

Figure 5.36: mean c_N values for a given $\hat{x}_0$ over a normalized t*, minus the mean c_N value for $\hat{x}_0$ = 0.75 for the same time, divided by k

5.2.6. Measurement uncertainty

In Table 5.2, the measurement uncertainty estimations are given for the experiments performed for 0 t* to 10 t*, in $c_N \times 100$. These uncertainties are similar to those reported in [49].

Table 5.2: Uncertainty estimates on the normal force coefficient c_N (95% confidence interval) for the differently filtered signals, in $c_N \times 100$

		c_N uncertainty		
$\hat{x}_0$	k	Ensemble	Denoised	DK
0.12	0.39	6.4	2.7	1.1
	0.2	6.4	3.0	1.5
	0.13	5.5	3.2	0.8
	0.1	8.2	3.6	1.1
0.25	0.39	9.4	2.5	0.7
	0.2	7.9	2.1	0.8
	0.13	6.3	2.5	0.8
	0.1	9.1	3.2	1.2
0.5	0.39	6.0	1.5	0.7
	0.2	5.4	1.3	0.7
	0.13	5.7	1.7	1.1
	0.1	5.2	1.2	0.7
0.75	0.39	7.5	3.3	1.3
	0.2	6.3	2.4	0.9
	0.13	6.0	2.6	0.9
	0.1	5.9	2.3	0.7
0.88	0.39	7.7	4.2	1.0
	0.2	7.1	2.7	0.8
	0.13	6.8	3.2	0.7
	0.1	7.6	3.1	0.8
	Average	6.8	2.6	0.9

The observations are very similar to those in Chapter 5.1, with the absolute c_N confidence intervals showing a good match.

6

Conclusions and recommendations

6.1. Conclusions

In this report, the Deconvolution Kalman filter is used to filter force measurements on revolving-pitching wings in a water tank. It is identified that the current filtering approach for typical water-tank force measurements in flapping wing research has the possibility to introduce errors. It is furthermore identified that there is little available literature on force measurements on revolving-pitching wings, and that measurements on revolving-surging wings are a logical part of a combined investigation. In this report these topics are addressed. The measurements are performed on a robotic flapper in water tank, the construction and design of which are considered typical for the performed measurements. To use the DK filter, a mathematical model capturing the vibrational modes of the measurement setup is required. For this mathematical model, the loading on the force sensor due to a given input and the mechanical vibrations of the measurement setup is needed. For the measurement setup under consideration, this is challenging as it is not directly possible to load the wing in such a way that only the mechanical vibrations were measured without measuring an unknown fluid-dynamic force component. To circumvent this problem, it is assumed that the motion input on the motor of the wing was accurate, and that a short pulse with high wing accelerations, but low velocity and displacement could be used to construct an input signal, of which the measured output signal would not contain large amounts of circulatory fluid-dynamic loading. A satisfactory state-space system is obtained using the PEM algorithm in Matlab, together with the advice of Richard Ahlfeld. The following steps are found necessary to obtain a satisfactory state space system. First, the impulse pulse is performed with the wing revolving at low speed to have a mechanical pre-load on the test rig, in an effort to reduce potential hysteresis effects. The force measurements need to be matched in time to a higher degree of accuracy than obtained by the start-point of the motion as obtained from the motion controller. If this time-matching is not performed, slight mismatches in timing can create large differences in oscillatory behaviour, as narrow force peaks can be ensemble averaged into a wider force peak. After inspection of the PSD estimate, it is concluded that low-pass filtering is necessary as noise components above $50\,\mathrm{Hz}$ would greatly decrease the chance of a successful identification of a linear system. When using the PEM algorithm, care needs to be taken that the algorithm has knowledge of the spectrum down to $0\,\mathrm{Hz}$. Finally, the search space is further limited by identifying separate lower-order systems for the two main modes of the structure, and by limiting the time span of the input signal.

The DK filter is found to be well-suited to reconstruct synthetically generated force signals. It is found to be straightforward to implement and robust regarding errors in the resonance frequency of the state-space system. The required covariance matrices can be determined heuristically, and it is found that the filter results are equally valid for a broad range of covariance matrix ratios. The steady-state error is very low and independent of frequency. In earlier work, a decrease in noise of the deconvoluted result is reported, which could not be replicated in this report. However, the uncertainty in the validity of the state-space system is found to be greater than the noise introduced by the deconvolution process for the measurements under consideration. Taking these points in consideration, it seems that the DK filter is very well suited to the type of measurements discussed in this report.

Generally, a statement can be made about the spatial resolution needed for force measurements to capture the complete dynamics of the wing. For the shown test rig, the spatial resolution is 50 Hz, or 12.5 cycles per t*. When low-pass filtering this data, no discernible loss of resolving power was found up until a cut-off frequency of 32 Hz, or 8 cycles per t*. Therefore value of 8 cycles per t* seems a good lower bound for required spatial resolution of similar experiments. It is possible that there are higher-frequency fluid-dynamic force mechanisms, but this is considered unlikely as the Welch's PSD estimates in Chapter 3.3 show that the measurement frequency content above 50 Hz consists mainly of peaks that are too narrow to be considered fluid-dynamic in origin. Also, frequency content above 12.5 cycles per t* would be in the order of 1×10^2 cycles per wingbeat for a biological flyer. This seems too high in frequency to be worthwhile to exploit for flapping wings.

The quasi-steady model as described in Chapter 2 qualitatively matches the measurement data. The surging- and pitching force histories show that the forces during accelerations in the motion can be considered a combination of the steady-state value, the rotational forces, and an added-mass value. This is an important observation and can be used designing future experiments, or during the initial design process of a flapping-wing flyer.

For the steady-state results, an agreement is found between the theoretical lift force generated by a Prandtl lifting-line (corrected for aspect ratio) and the normal force of the measurements. The same agreement is found for previous experiments, and this agreement can be used for future estimation models.

Quantitatively, the forces during the unsteady force generation are lower than the quasi-steady predictions, and previous experiments. However, generated forces during the steady part of the motion, especially for the surging experiments match up well with previous experiments in terms of normal force and force vector angle. A possible fluid-dynamic reason for the lower than expected forces during the unsteady phase is found in the lower than expected force contribution of the root part of the wing, as evidenced by the COP locations plotted in Chapter 5. This relation holds true for the entire range of experiments. This in itself is interesting, but without flow visualization it is difficult to hypothesize a reason for this. It must be noted that the lower forces are reported for both the revolving-surging and revolving-pitching experiments, which suggests a relation to either the wing mounting or morphology instead of a relation to wing kinematics. Especially when compared to earlier experiments using almost the same setup, which showed a higher force production (Perçin et al. [49]), the changes in morphology are small: a slightly lower Rossby number (1.66 compared to 1.8) and a change in pitching axis location ($\hat{x}_0$ = 0.12 compared to 0). These changes are small in absolute magnitude, but non-linear effects can potentially be responsible for the lower force production in this report. The COP location during the pitching experiment shows that the pitching motion itself has a pronounced effect on the location of the COP, 'pushing' the COP tipward. After the pitching phase, the COP moves towards the location it will stay for the steady part of the motion, over a period of around Δt^* = 3. This time period can be considered the time for the large-scale effects introduced by the pitching to dissipate, however, the c_N value and COP location are different than for the $45\,^\circ\alpha$ surging experiment, indicating that the pitching changes the structure of the flow around the wing for an extended period of time. This is contrary to what the quasi-steady model suggests. There is an observed relation between the COP chordwise location and the pitching axis location, where the experiments with a more trailing edge-ward pitching axis show a COP that is more towards the leading edge, at the end of the motion. Furthermore, a relation between a lower c_N during the steady part of the motion, and a higher positive c_T was found. However, the absolute differences in magnitude are very small, and the found relation did not translate into meaningful differences in terms of wing performance (c_N/c_T).

Another finding is that the expected linear relationship between pitching rate and generated force due to pitching motion does not hold for the experiments under consideration. More importantly, there does not seem to be a straightforward relationship between pitching rate and generated force due to pitching motion. Based on the data in this report, the possibility of developing an accurate estimation model taking into account pitching rate is doubtful.

6.2. Recommendations

The recommendations are, as the conclusions, split up in the three parts described in this thesis.

The Deconvolution Kalman Filter seems to work well to more accurately filter force measurement setups, given that the measurement setup can be described by a state-space system. Finding such a system was a challenging requirement. For future work, to more accurately perform the system identification, to have more confidence in the identified system, and to facilitate the process, the measured forces due to an excitation of the measurement setup need to be known more precisely. This is especially true for the excitation signal, which, in this report, was obtained using numerous assumptions. This greatly complicated the system identification process. To improve on this, more sophisticated measurement equipment is needed to generate a known excitation of the mechanical vibration of the measurement setup. It could also be of interest to explore the option of designing the measurement setup such that the response can be better captured by a linear state-space system. The need for more sophisticated deconvolution algorithms can be explored and was mentioned by both Bora et al. [10], and Ahlfeld [1], however, the current setup of the DK filter seems to work well and is rather simple to implement, with the most difficult part being the system identification process. According to the author, the need for a more sophisticated deconvolution algorithm, that for instance can work with non-linear systems, only arises if it proves impossible to have a linear system representing the measurement setup. Then the need for a non-linear system identification process also arises, which is expected to further increase the complexity, and decrease the tractability of the filtering stage of the experiment. It is expected that it is be possible to design a measurement setup that can be described by a linear state-space system, especially for the rather low frequencies under consideration.

The filter does offer the possibility to create measurement setups that are less traditionally rigid, but have less interference with the flow. In this report, the presence of the wing pitching servo box is suspected to influence the flow measurements. With a filter that is better suited to deal with mechanical vibrations, more slender constructions might lead to measurement setups in which the researcher can have more confidence regarding flow similarity.

The force measurements itself raised questions, not in terms of the validity of the data, but in terms of what was happening with the flow. The data is found to offer a solid foundation to design new flow visualisation experiments, especially in terms of the relation between the chordwise location of the COP and the pitching axis, even after several t* after the pitching phase. Also during the pitching phase itself, it is expected that it is possible to identify flow structures that can be related to the diminished force production compared to the theoretical force production of the rotating wing. Furthermore, an investigation in the magnitude of the force augmentation related to pitching could be fruitful as the limited amount of data points in this report (16, see Figure 5.36) paint a confusing picture, in disagreement with current simplified models.

To have a good agreement between measurement and data, it is vital that the researcher knows exactly what motion the wing is performing. Wing position sensors with a high spatial and temporal resolution can be considered a requirement for future research into estimation models.

The described agreement between the normal force at steady velocity for a revolving wing and the lift force for an aspect ratio-corrected lifting line could be tested for other wing configurations as the relation could be beneficial to design future force estimation models, or to design new experiments.

Appendices

Appendix A

A.1. Centre of Pressure locations for revolving-surging measurements

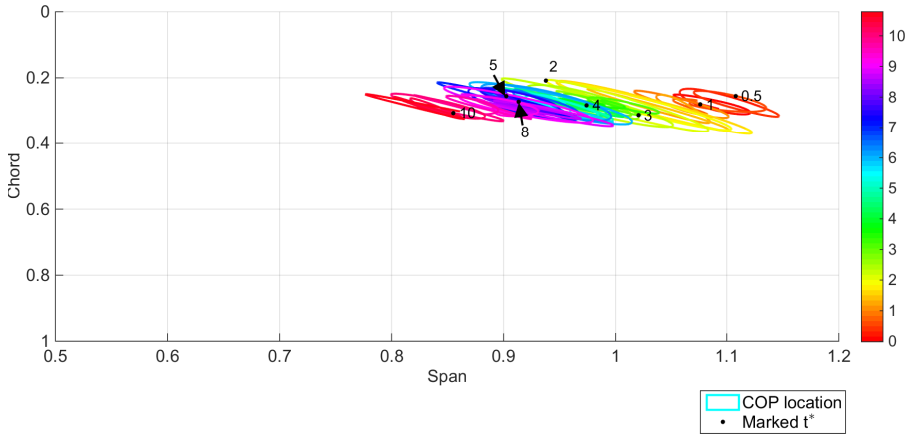

Figure A.1: Center of Pressure (COP) for the revolving-surging motion of the wing at 8°α. The colorbar signifies the progressing of time in t*, with t* = 0.5,1,2,3,4,5,8, and 10 indicated with black dots.

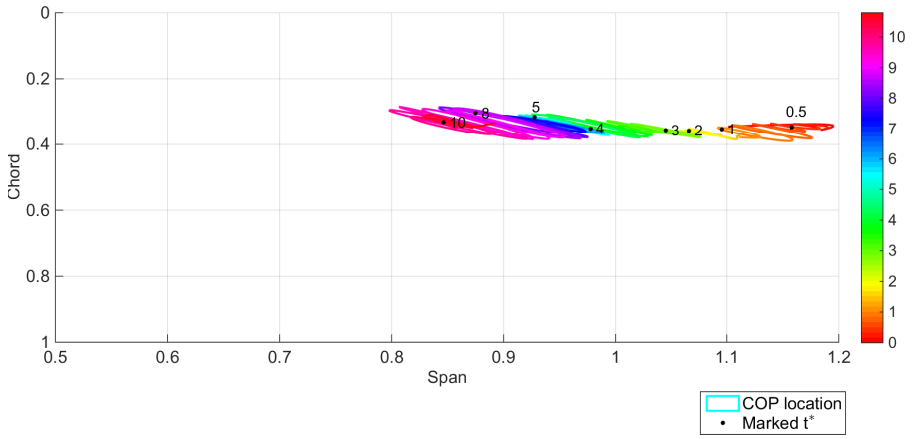

Figure A.2: Center of Pressure (COP) for the revolving-surging motion of the wing at 13°α. The colorbar signifies the progressing of time in t*, with t* = 0.5,1,2,3,4,5,8, and 10 indicated with black dots.

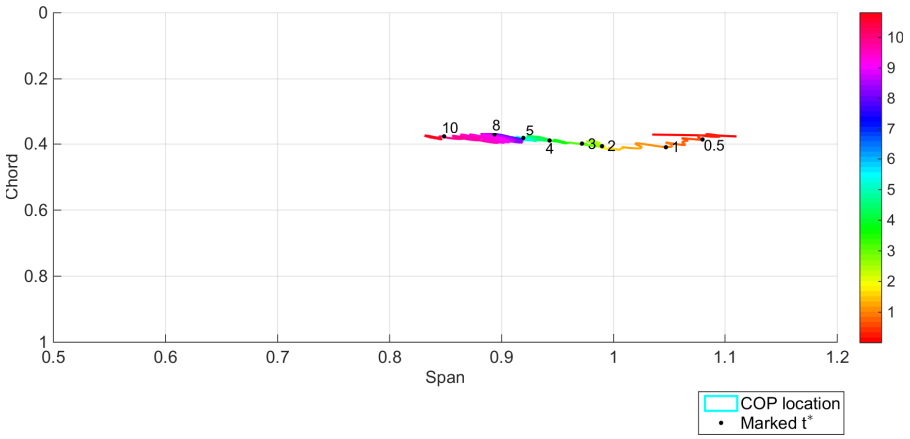

Figure A.3: Center of Pressure (COP) for the revolving-surging motion of the wing at 23°α. The colorbar signifies the progressing of time in t*, with t* = 0.5,1,2,3,4,5,8, and 10 indicated with black dots.

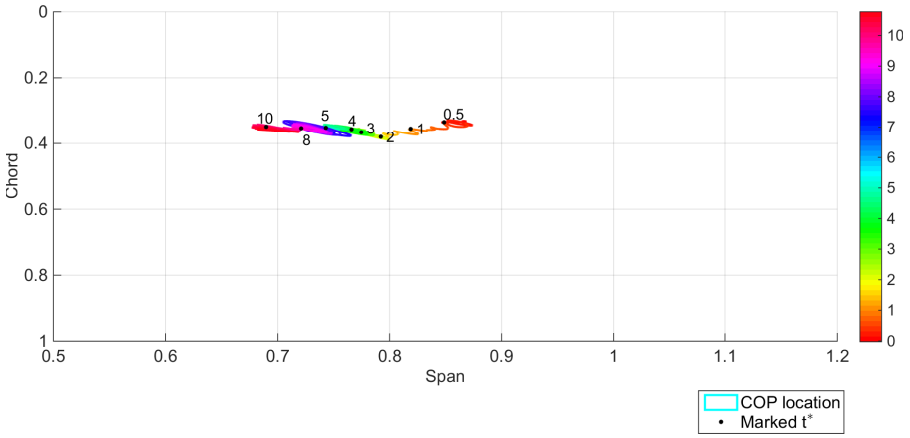

Figure A.4: Center of Pressure (COP) for the revolving-surging motion of the wing at 28°α. The colorbar signifies the progressing of time in t*, with t* = 0.5,1,2,3,4,5,8, and 10 indicated with black dots.

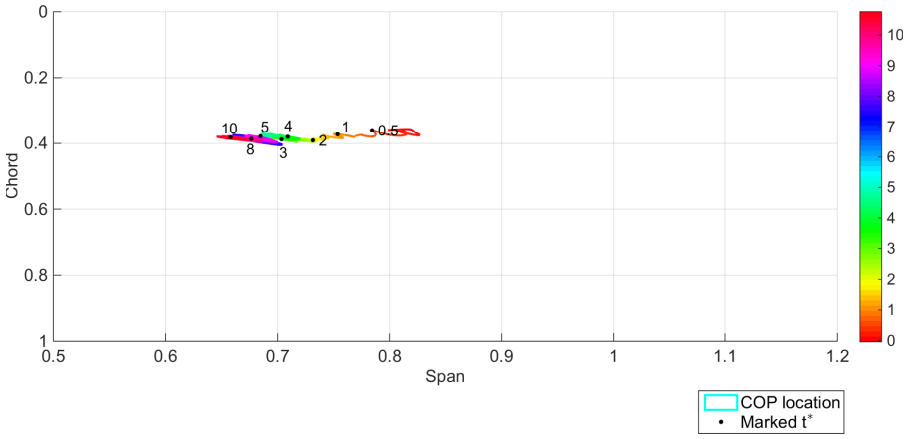

Figure A.5: Center of Pressure (COP) for the revolving-surging motion of the wing at 39°α. The colorbar signifies the progressing of time in t*, with t* = 0.5,1,2,3,4,5,8, and 10 indicated with black dots.

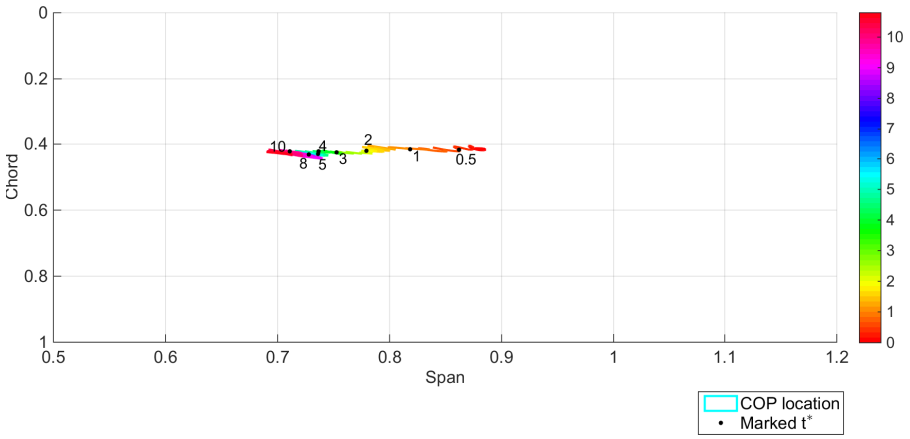

Figure A.6: Center of Pressure (COP) for the revolving-surging motion of the wing at 45°α. The colorbar signifies the progressing of time in t*, with t* = 0.5,1,2,3,4,5,8, and 10 indicated with black dots.

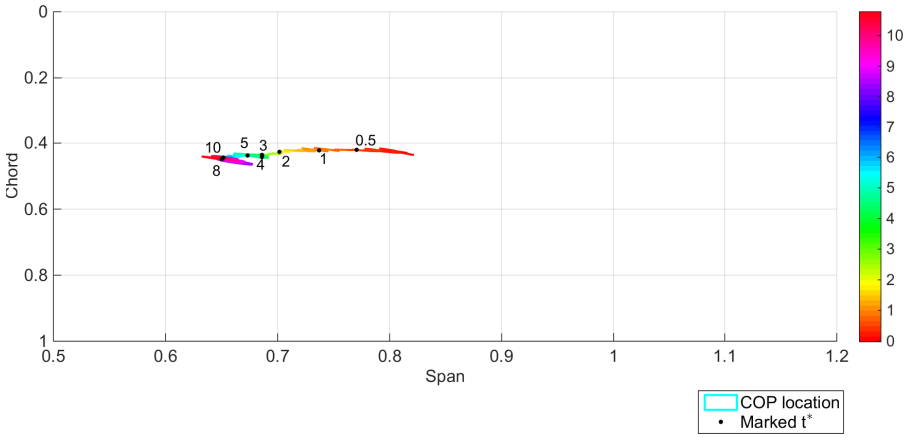

Figure A.7: Center of Pressure (COP) for the revolving-surging motion of the wing at 59°α. The colorbar signifies the progressing of time in t*, with t* = 0.5,1,2,3,4,5,8, and 10 indicated with black dots.

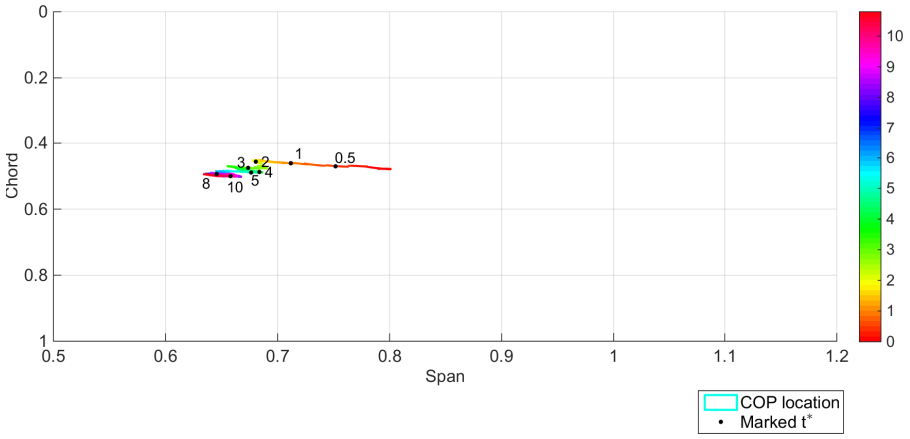

Figure A.8: Center of Pressure (COP) for the revolving-surging motion of the wing at 70°α. The colorbar signifies the progressing of time in t*, with t* = 0.5,1,2,3,4,5,8, and 10 indicated with black dots.

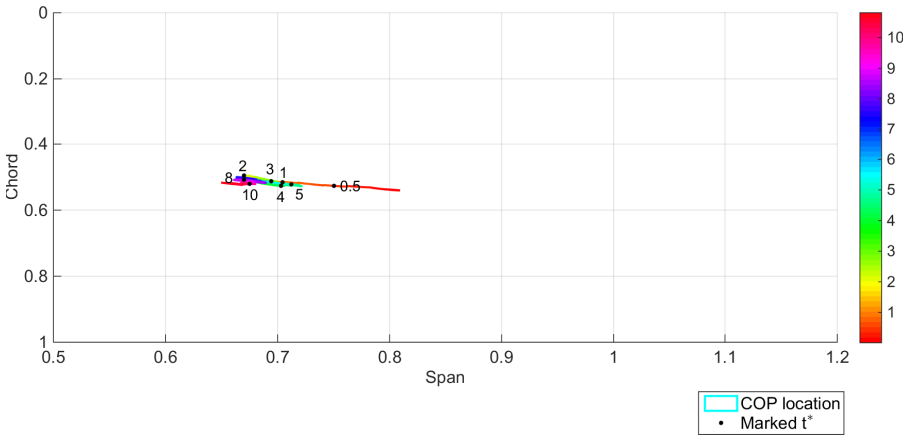

Figure A.9: Center of Pressure (COP) for the revolving-surging motion of the wing at 80°α. The colorbar signifies the progressing of time in t*, with t* = 0.5,1,2,3,4,5,8, and 10 indicated with black dots.

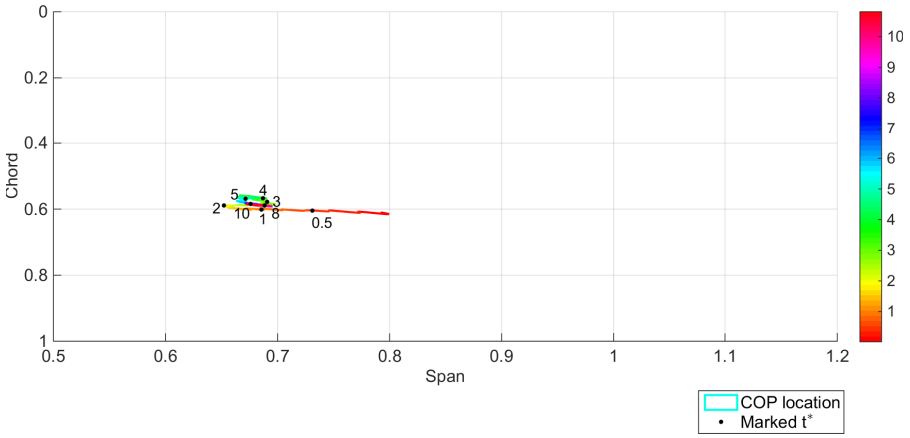

Figure A.10: Center of Pressure (COP) for the revolving-surging motion of the wing at 90°α. The colorbar signifies the progressing of time in t*, with t* = 0.5,1,2,3,4,5,8, and 10 indicated with black dots.

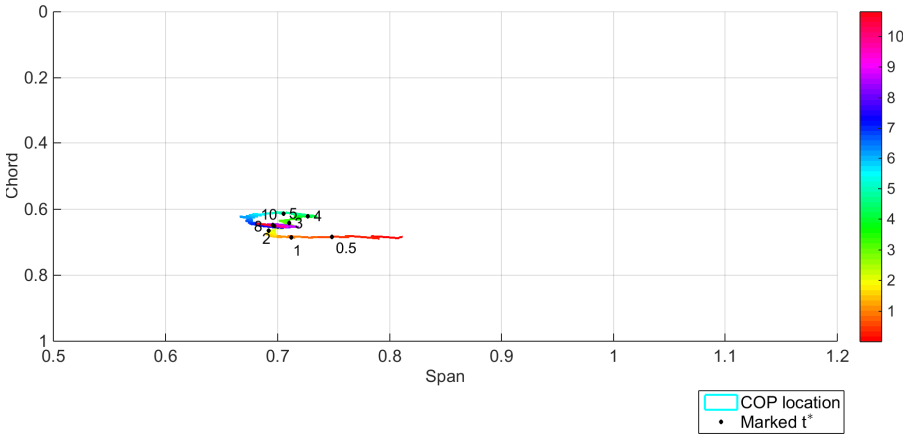

Figure A.11: Center of Pressure (COP) for the revolving-surging motion of the wing at 100°α. The colorbar signifies the progressing of time in t*, with t* = 0.5,1,2,3,4,5,8, and 10 indicated with black dots.

B

Appendix B

B.1. Revolving-pitching normal force coefficient for constant pitching axis location

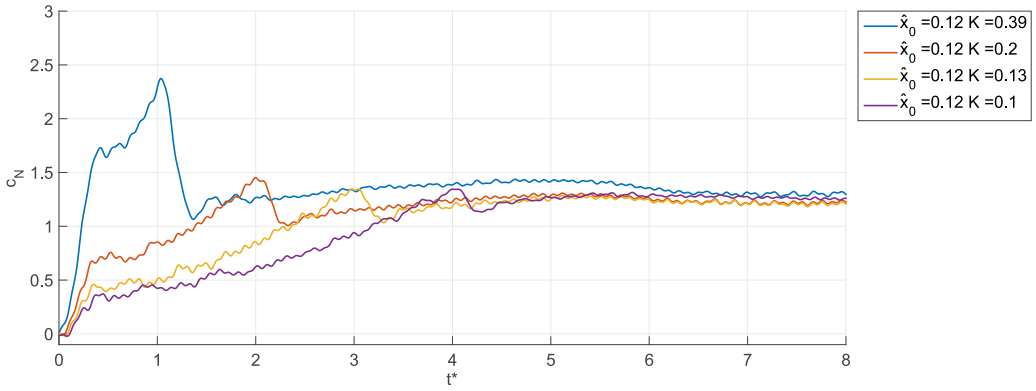

Figure B.1: DK filtered measured normal force coefficients for revolving-pitching measurements with $\hat{x}_0$ = 0.12, k = 0.39, 0.2, 0.13, 0.1

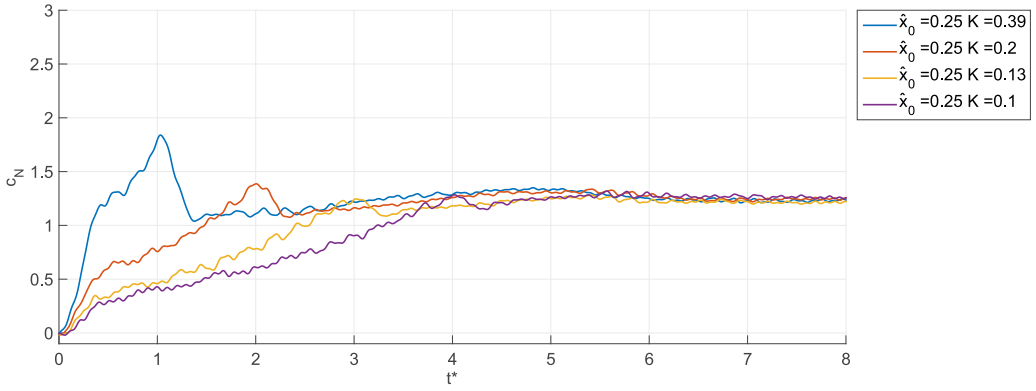

Figure B.2: DK filtered measured normal force coefficients for revolving-pitching measurements with $\hat{x}_0$ = 0.25, k = 0.39, 0.2, 0.13, 0.1

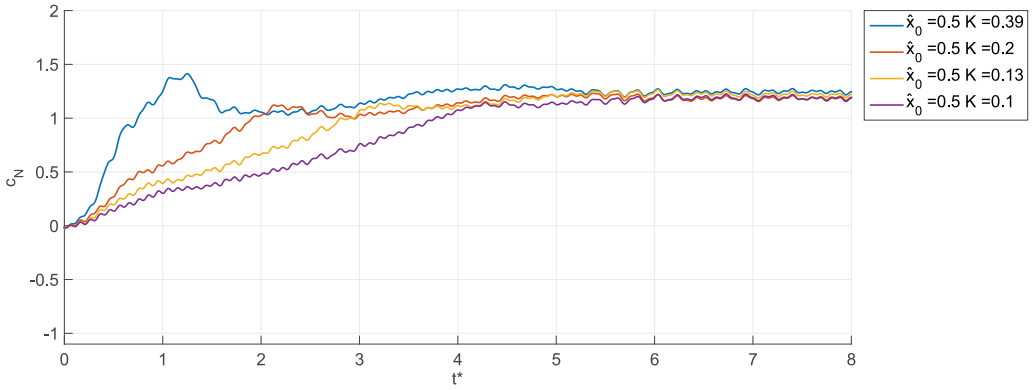

Figure B.3: DK filtered measured normal force coefficients for revolving-pitching measurements with $\hat{x}_0$ = 0.50, k = 0.39, 0.2, 0.13, 0.1

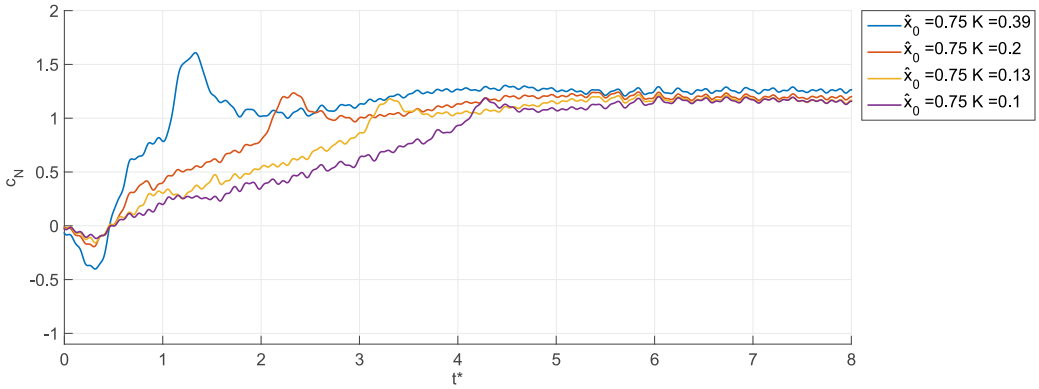

Figure B.4: DK filtered measured normal force coefficients for revolving-pitching measurements with $\hat{x}_0$ = 0.75, k = 0.39, 0.2, 0.13, 0.1

B.2. Revolving-pitching thrust coefficient for constant pitching axis location

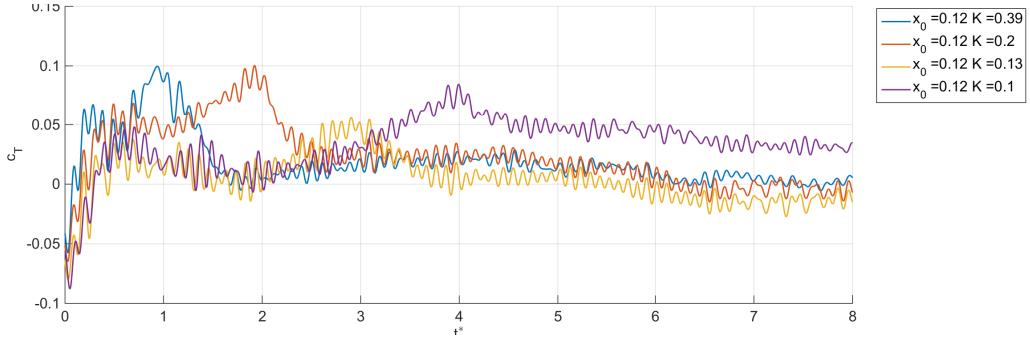

Figure B.5: DK filtered measured tangential force coefficients for revolving-pitching measurements with $\hat{x}_0$ = 0.12, k = 0.39, 0.2, 0.13, 0.1

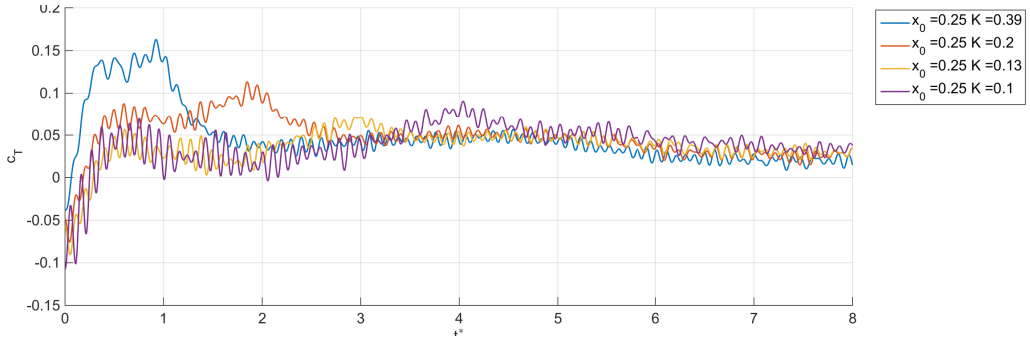

Figure B.6: DK filtered measured tangential force coefficients for revolving-pitching measurements with $\hat{x}_0$ = 0.25, k = 0.39, 0.2, 0.13, 0.1

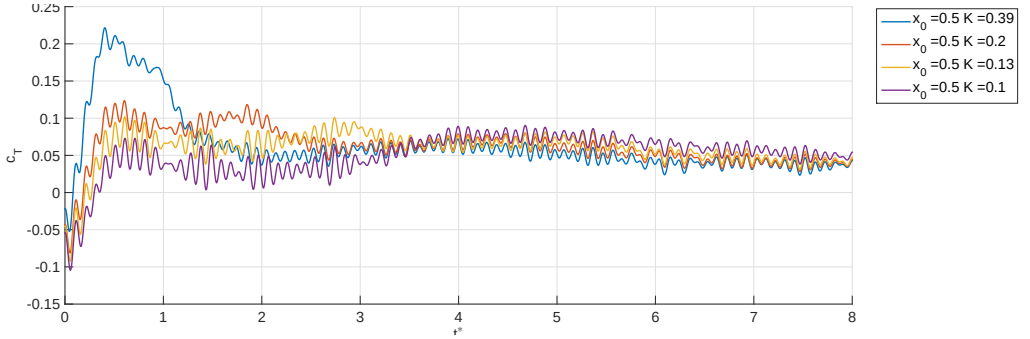

Figure B.7: DK filtered measured tangential force coefficients for revolving-pitching measurements with $\hat{x}_0$ = 0.50, k = 0.39, 0.2, 0.13, 0.1

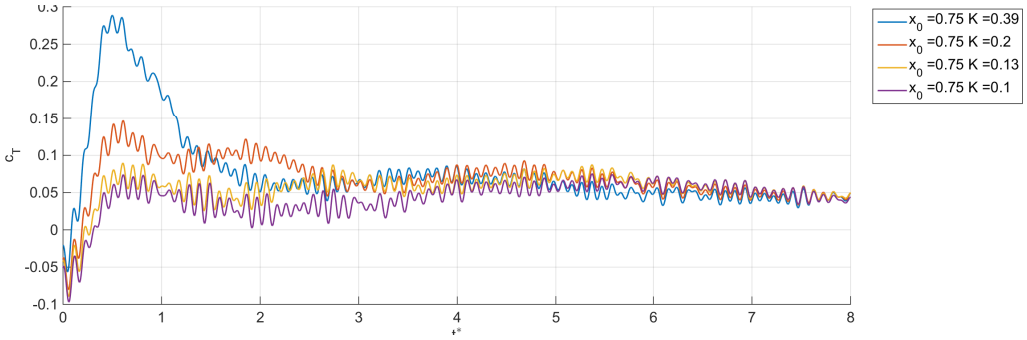

Figure B.8: DK filtered measured tangential force coefficients for revolving-pitching measurements with $\hat{x}_0$ = 0.75, k = 0.39, 0.2, 0.13, 0.1

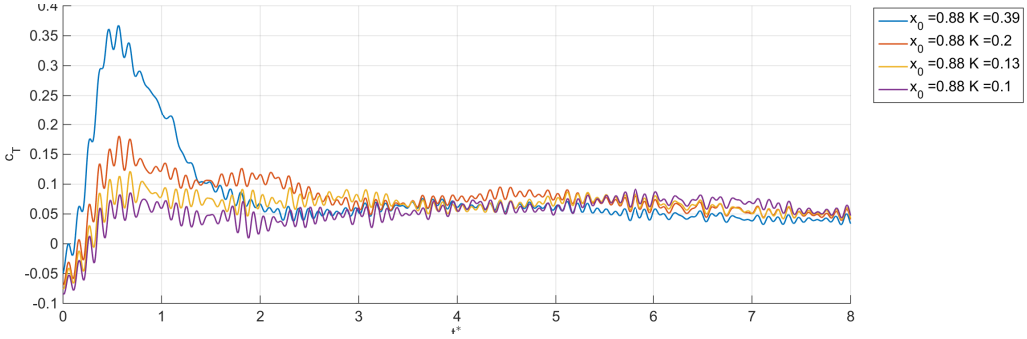

Figure B.9: DK filtered measured tangential force coefficients for revolving-pitching measurements with $\hat{x}_0$ = 0.88 k = 0.39, 0.2, 0.13, 0.1

B.3. Centre of Pressure locations for revolving-pitching measurements

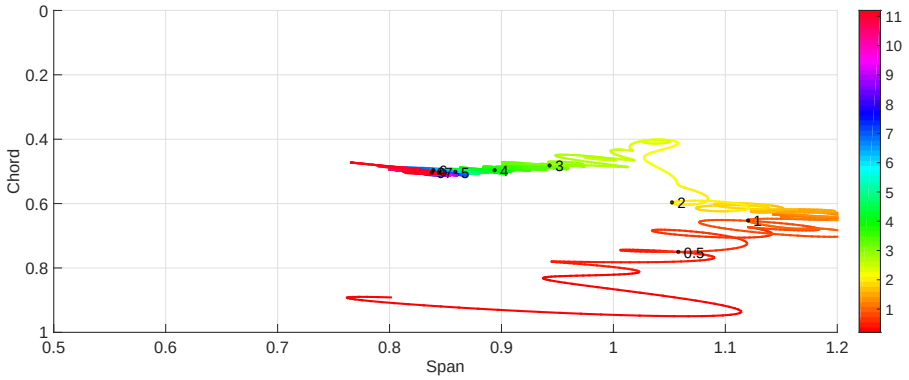

Figure B.10: Center of Pressure location for entire motion for $\hat{x}_0$ = 0.12, k = 0.2. The colorbar signifies the progressing of time in t*, with t* = 0.5,1,2,3,4,5,6,7, and 9 indicated with black dots.

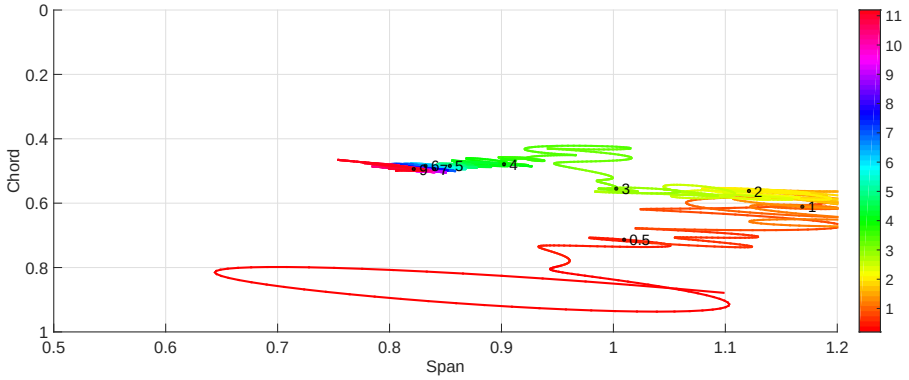

Figure B.11: Center of Pressure location for entire motion for $\hat{x}_0$ = 0.12, k = 0.13. The colorbar signifies the progressing of time in t*, with t* = 0.5,1,2,3,4,5,6,7, and 9 indicated with black dots.

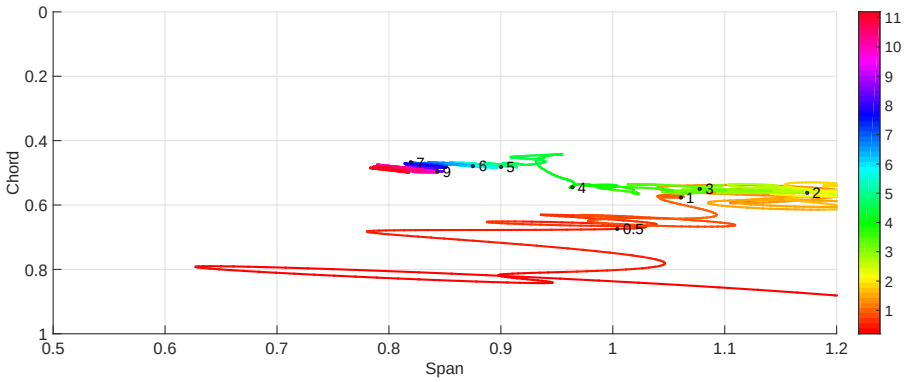

Figure B.12: Center of Pressure location for entire motion for $\hat{x}_0$ = 0.12, k = 0.1. The colorbar signifies the progressing of time in t*, with t* = 0.5,1,2,3,4,5,6,7, and 9 indicated with black dots.

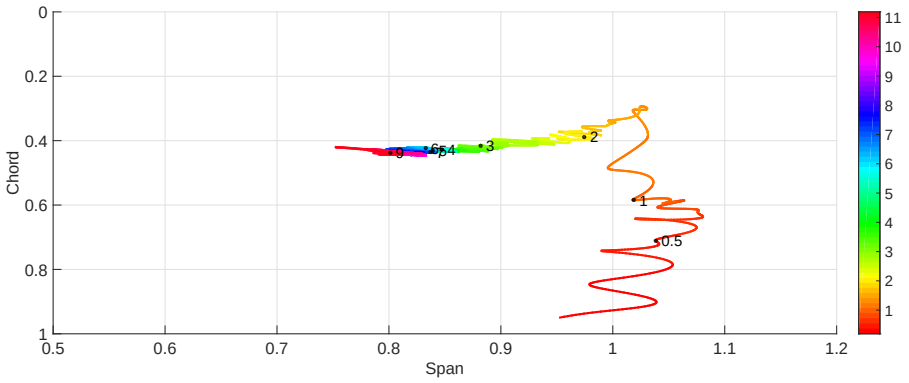

Figure B.13: Center of Pressure location for entire motion for $\hat{x}_0$ = 0.25, k = 0.39. The colorbar signifies the progressing of time in t*, with t* = 0.5,1,2,3,4,5,6,7, and 9 indicated with black dots.

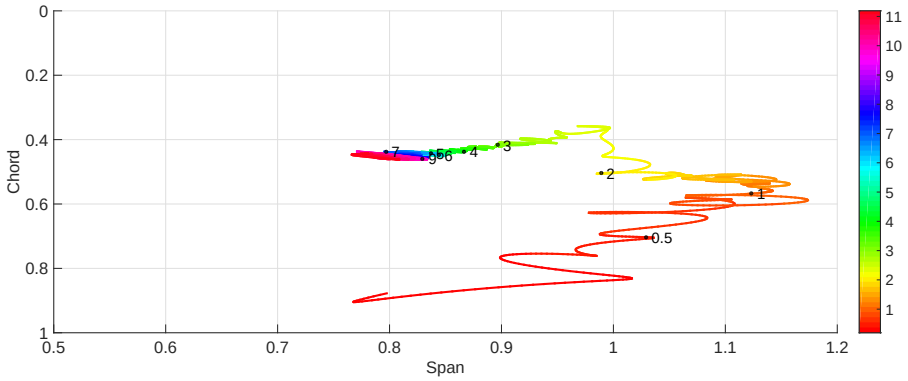

Figure B.14: Center of Pressure location for entire motion for $\hat{x}_0$ = 0.25, k = 0.2. The colorbar signifies the progressing of time in t*, with t* = 0.5,1,2,3,4,5,6,7, and 9 indicated with black dots.

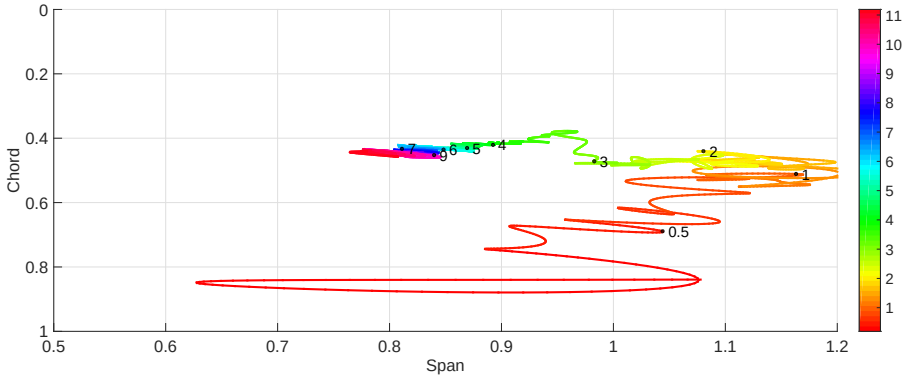

Figure B.15: Center of Pressure location for entire motion for $\hat{x}_0$ = 0.25, k = 0.13. The colorbar signifies the progressing of time in t*, with t* = 0.5,1,2,3,4,5,6,7, and 9 indicated with black dots.

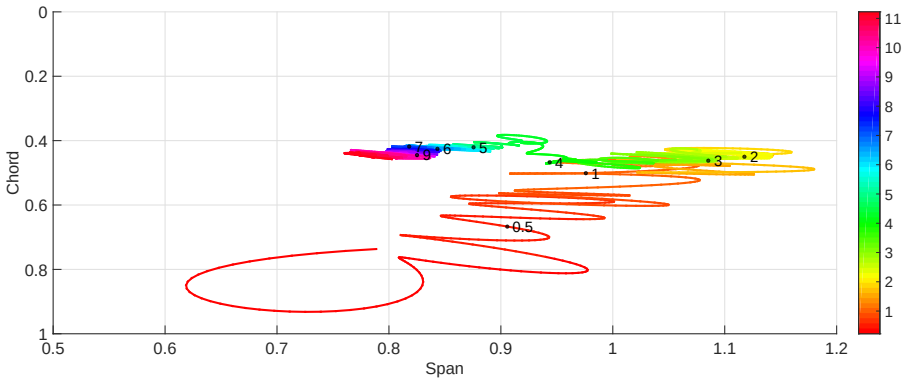

Figure B.16: Center of Pressure location for entire motion for $\hat{x}_0$ = 0.25, k = 0.1. The colorbar signifies the progressing of time in t*, with t* = 0.5,1,2,3,4,5,6,7, and 9 indicated with black dots.

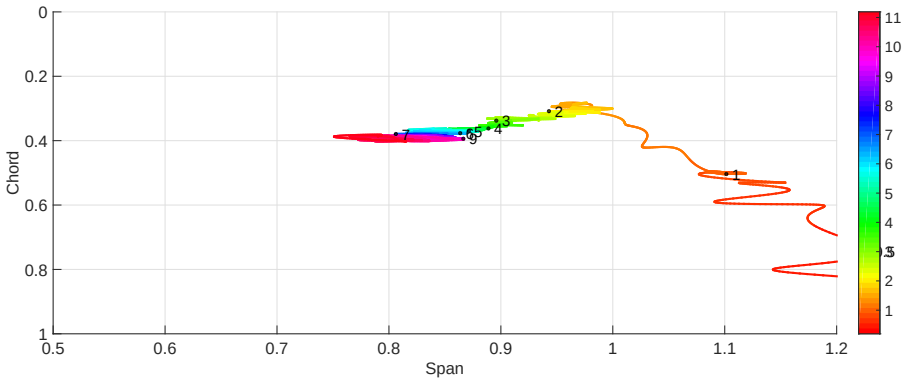

Figure B.17: Center of Pressure location for entire motion for $\hat{x}_0$ = 0.5, k = 0.39. The colorbar signifies the progressing of time in t*, with t* = 0.5,1,2,3,4,5,6,7, and 9 indicated with black dots.

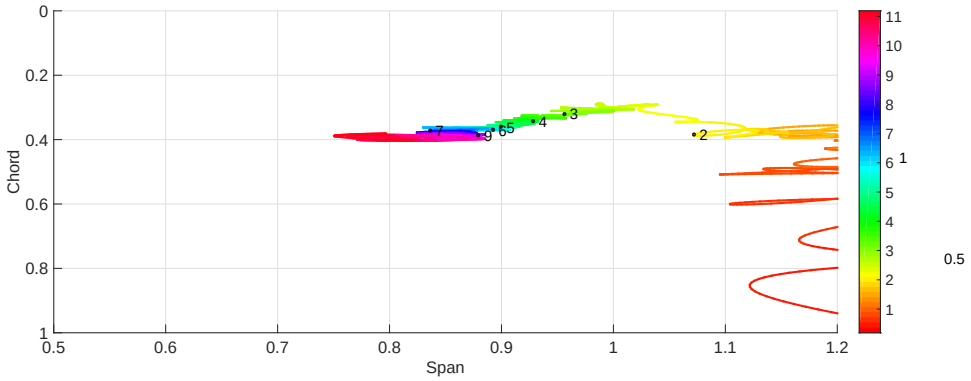

Figure B.18: Center of Pressure location for entire motion for $\hat{x}_0$ = 0.5, k = 0.2. The colorbar signifies the progressing of time in t*, with t* = 0.5,1,2,3,4,5,6,7, and 9 indicated with black dots.

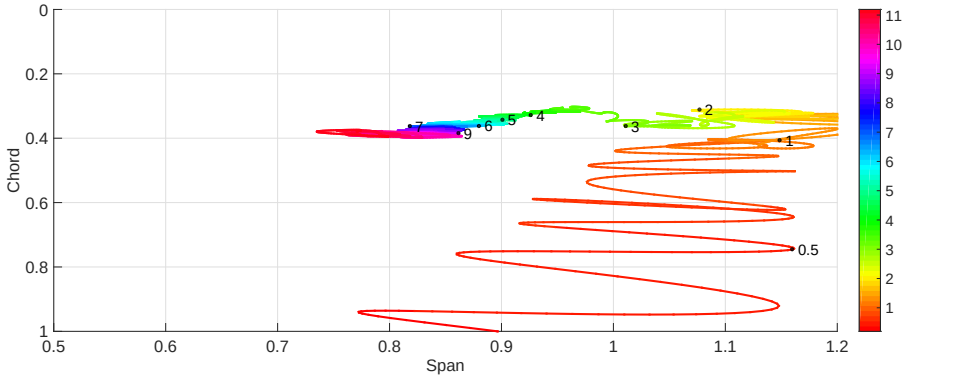

Figure B.19: Center of Pressure location for entire motion for $\hat{x}_0$ = 0.5, k = 0.13. The colorbar signifies the progressing of time in t*, with t* = 0.5,1,2,3,4,5,6,7, and 9 indicated with black dots.

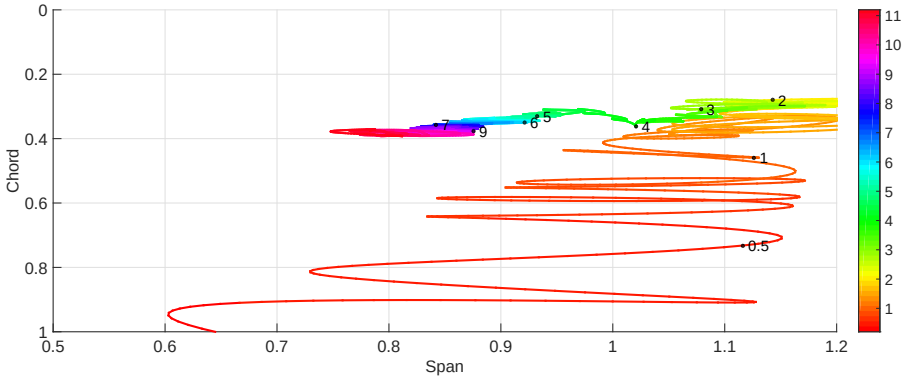

Figure B.20: Center of Pressure location for entire motion for $\hat{x}_0$ = 0.5, k = 0.1. The colorbar signifies the progressing of time in t^*, with t^* = 0.5,1,2,3,4,5,6,7, and 9 indicated with black dots.

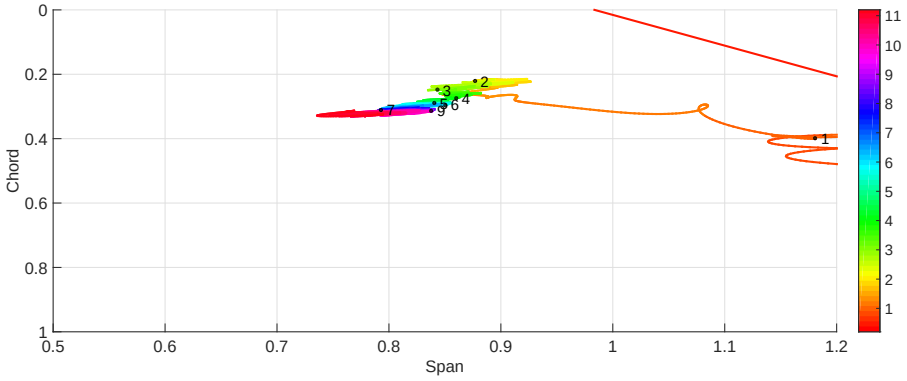

Figure B.21: Center of Pressure location for entire motion for $\hat{x}_0$ = 0.75, k = 0.39. The colorbar signifies the progressing of time in t^*, with t^* = 0.5,1,2,3,4,5,6,7, and 9 indicated with black dots.

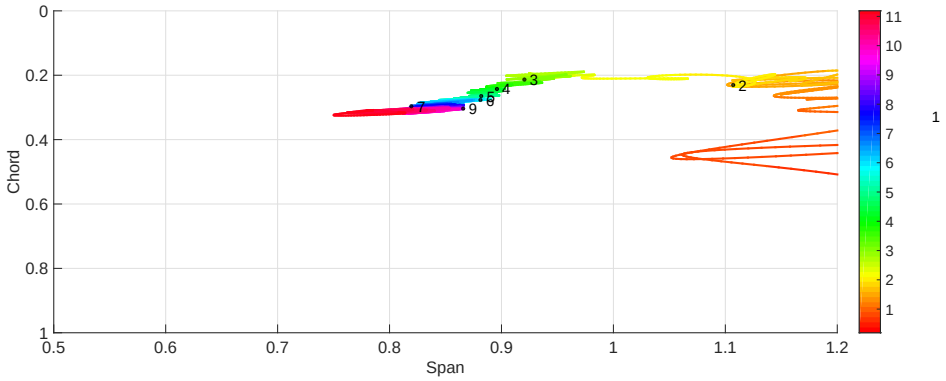

Figure B.22: Center of Pressure location for entire motion for $\hat{x}_0$ = 0.75, k = 0.2. The colorbar signifies the progressing of time in t*, with t* = 0.5,1,2,3,4,5,6,7, and 9 indicated with black dots.

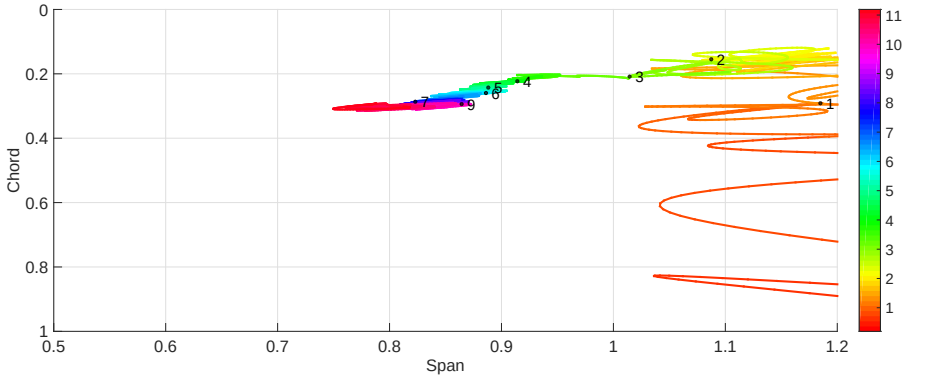

Figure B.23: Center of Pressure location for entire motion for $\hat{x}_0$ = 0.75, k = 0.13. The colorbar signifies the progressing of time in t*, with t* = 0.5,1,2,3,4,5,6,7, and 9 indicated with black dots.

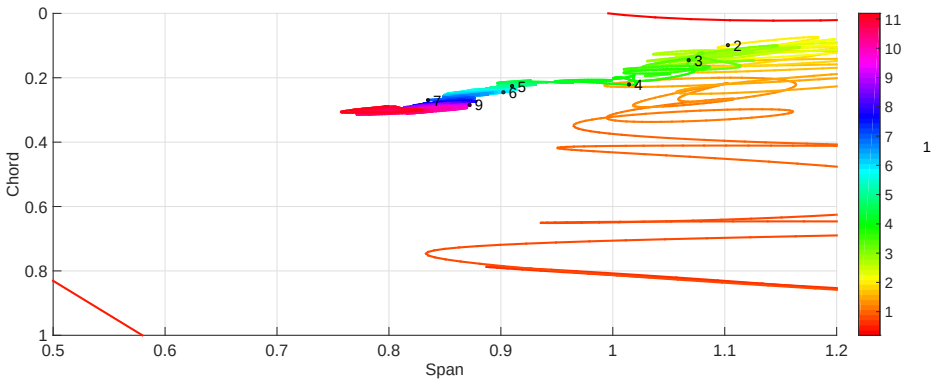

Figure B.24: Center of Pressure location for entire motion for $\hat{x}_0$ = 0.75, k = 0.1. The colorbar signifies the progressing of time in t*, with t* = 0.5,1,2,3,4,5,6,7, and 9 indicated with black dots.

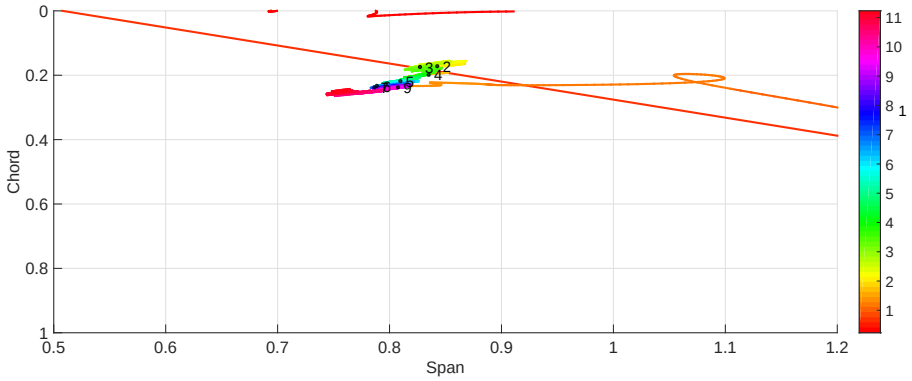

Figure B.25: Center of Pressure location for entire motion for $\hat{x}_0$ = 0.88, k = 0.39. The colorbar signifies the progressing of time in t*, with t* = 0.5,1,2,3,4,5,6,7, and 9 indicated with black dots.

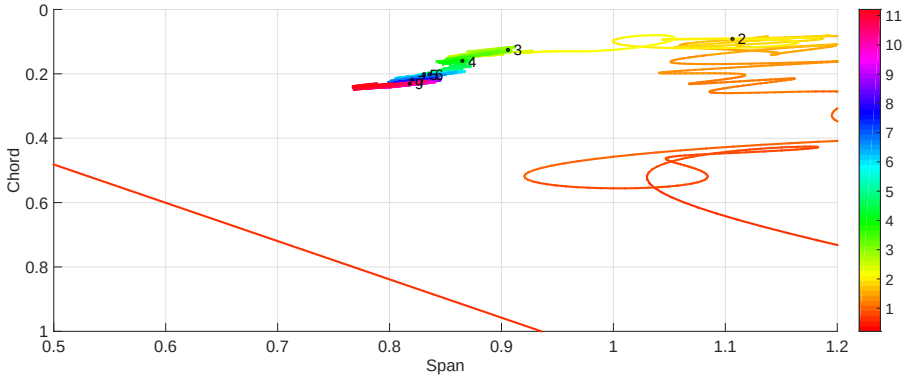

Figure B.26: Center of Pressure location for entire motion for $\hat{x}_0$ = 0.88, k = 0.2. The colorbar signifies the progressing of time in t*, with t* = 0.5,1,2,3,4,5,6,7, and 9 indicated with black dots.

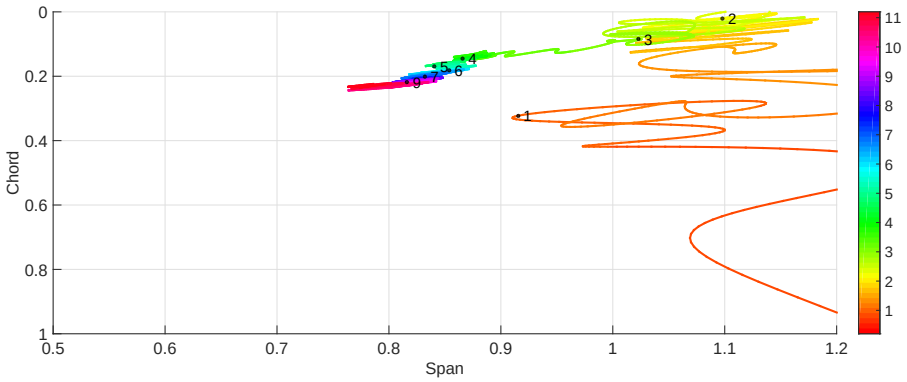

Figure B.27: Center of Pressure location for entire motion for $\hat{x}_0$ = 0.88, k = 0.13. The colorbar signifies the progressing of time in t*, with t* = 0.5,1,2,3,4,5,6,7, and 9 indicated with black dots.

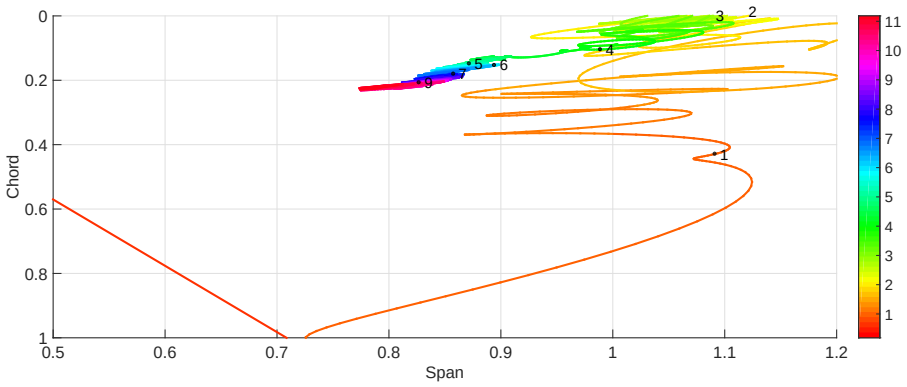

Figure B.28: Center of Pressure location for entire motion for $\hat{x}_0$ = 0.88, k = 0.1. The colorbar signifies the progressing of time in t*, with t* = 0.5,1,2,3,4,5,6,7, and 9 indicated with black dots.

Bibliography

[1] Richard BH Ahlfeld. *Deconvolution Filters for Dynamic Rocket Thrust Measurements*. PhD thesis, TU Delft, Delft University of Technology, 2014.

[2] John David Anderson. *Fundamentals of aerodynamics*. McGraw-Hill series in aeronautical and aerospace engineering. McGraw-Hill, Singapore, Boston, Burr Ridge, 2011. ISBN 978-007-128908-5.

[3] Hikaru Aono, Wei Shyy, and Hao Liu. Near wake vortex dynamics of a hovering hawkmoth. *Acta Mechanica Sinica*, 25(1):23–36, 2009.

[4] ATI Industrial Automation. F/t sensor: Nano17, 2015. URL `http://www.ati-ia.com/products/ft/ft_models.aspx?id=Nano17`.

[5] Nathan Beals and Anya R Jones. Lift production by a passively flexible rotating wing. *AIAA Journal*, 2015.

[6] James M Birch and Michael H Dickinson. Spanwise flow and the attachment of the leading-edge vortex on insect wings. *Nature*, 412(6848):729–733, 2001.

[7] James M Birch and Michael H Dickinson. The influence of wing–wake interactions on the production of aerodynamic forces in flapping flight. *Journal of Experimental Biology*, 206(13):2257–2272, 2003.

[8] James M Birch, William B Dickson, and Michael H Dickinson. Force production and flow structure of the leading edge vortex on flapping wings at high and low reynolds numbers. *Journal of Experimental Biology*, 207(7):1063–1072, 2004.

[9] Richard J Bomphrey, Nicholas J Lawson, Nicholas J Harding, Graham K Taylor, and Adrian LR Thomas. The aerodynamics of manduca sexta: digital particle image velocimetry analysis of the leading-edge vortex. *Journal of Experimental Biology*, 208(6):1079–1094, 2005.

[10] Siddharth Sankar Bora, Yepuganti Karuna, Ravindra Dhuli, and Brejesh Lall. Iir deconvolution from noisy observations using kalman filtering. In *Signal and Image Processing (ICSIP), 2010 International Conference on*, pages 339–342. IEEE, 2010.

[11] Frank M Bos, Bas W van Oudheusden, and Hester Bijl. Wing performance and 3-d vortical structure formation in flapping flight. *Journal of Fluids and Structures*, 42:130–151, 2013.

[12] M Bross and D Rockwell. Flow structure on a simultaneously pitching and rotating wing. *Journal of Fluid Mechanics*, 756:354–383, 2014.

[13] M Bross, CA Ozen, and D Rockwell. Flow structure on a rotating wing: effect of steady incident flow. *Physics of Fluids (1994-present)*, 25(8):081901, 2013.

[14] ZR Carr, C Chen, and MJ Ringuette. Finite-span rotating wings: three-dimensional vortex formation and variations with aspect ratio. *Experiments in fluids*, 54(2):1–26, 2013.

[15] Bo Cheng, Sanjay P Sane, Giovanni Barbera, Daniel R Troolin, Tyson Strand, and Xinyan Deng. Three-dimensional flow visualization and vorticity dynamics in revolving wings. *Experiments in fluids*, 54(1):1–12, 2013.

[16] Laurent David, Thierry Jardin, Patrick Braud, and Alain Farcy. Time-resolved scanning tomography piv measurements around a flapping wing. *Experiments in fluids*, 52(4):857–864, 2012.

[17] Mark Denny. Dynamic soaring: aerodynamics for albatrosses. *European Journal of Physics*, 30 (1):75, 2008.

[18] M Dickinson. The effects of wing rotation on unsteady aerodynamic performance at low reynolds numbers. *The Journal of Experimental Biology*, 192(1):179–206, 1994.

[19] Michael H Dickinson, Fritz-Olaf Lehmann, and Sanjay P Sane. Wing rotation and the aerodynamic basis of insect flight. *Science*, 284(5422):1954–1960, 1999.

[20] William B Dickson and Michael H Dickinson. The effect of advance ratio on the aerodynamics of revolving wings. *Journal of Experimental Biology*, 207(24):4269–4281, 2004.

[21] J D Eldredge and C Wang. A computational study of a canonical pitch-up, pitch-down wing maneuver. In *39th AIAA Fluid Dynamics Conference (San Antonio, Texas)*, page 339. AIAA, 2009.

[22] Yossef Elimelech, Dmitry Kolomenskiy, Stuart B Dalziel, and HK Moffatt. Evolution of the leading-edge vortex over an accelerating rotating wing. *Procedia IUTAM*, 7:233–242, 2013.

[23] Charles P Ellington, Coen Van Den Berg, Alexander P Willmott, and Adrian LR Thomas. Leading-edge vortices in insect flight. *Nature*, 384:626–630, 1996.

[24] Karl Georg Götz, Bärbel Hengstenberg, and Roland Biesinger. Optomotor control of wing beat and body posture in drosophila. *Biological Cybernetics*, 35(2):101–112, 1979.

[25] Kenneth O Granlund, Michael V Ol, and Luis P Bernal. Unsteady pitching flat plates. *Journal of Fluid Mechanics*, 733:R5, 2013.

[26] Simon Haykin. *Kalman filtering and neural networks*, volume 47. John Wiley & Sons, 2004.

[27] Daniel J Inman and Ramesh Chandra Singh. *Engineering vibration*, volume 3. Prentice Hall Upper Saddle River, 2001.

[28] Thierry Jardin, Laurent David, and Alain Farcy. Characterization of vortical structures and loads based on time-resolved piv for asymmetric hovering flapping flight. In *Animal Locomotion*, pages 285–295. Springer, 2010.

[29] AR Jones and H Babinsky. Unsteady lift generation on rotating wings at low reynolds numbers. *Journal of Aircraft*, 47(3):1013–1021, 2010.

[30] AR Jones and H Babinsky. Reynolds number effects on leading edge vortex development on a waving wing. *Experiments in fluids*, 51(1):197–210, 2011.

[31] Rudolph Emil Kalman. A new approach to linear filtering and prediction problems. *Journal of Fluids Engineering*, 82(1):35–45, 1960.

[32] Gide Koekkoek, Florian T Muijres, L Christoffer Johansson, Melanie Stuiver, Bas W van Oudheusden, and Anders Hedenström. Stroke plane angle controls leading edge vortex in a bat-inspired flapper. *Comptes Rendus Mecanique*, 340(1):95–106, 2012.

[33] Von M Kramer. Die zunahme des maximalauftriebes von tragflugeln bei plotzlicher anstellwinkelvergrosserung (boeneffekt). *Z. Flugtech. Motorluftschiff*, 23:185–189, 1932.

[34] Ilan Kroo and Peter Kunz. Mesoscale flight and miniature rotorcraft development," in fixed and flapping wing aerodynamics for micro air vehicle applications. In *of Progress in Astronautics and Aeronautics*. Citeseer, 2001.

[35] Kenneth R Langley, Eric Hardester, Scott L Thomson, and Tadd T Truscott. Three-dimensional flow measurements on flapping wings using synthetic aperture piv. *Experiments in Fluids*, 55(10): 1–16, 2014.

[36] Fritz-Olaf Lehmann. The mechanisms of lift enhancement in insect flight. *Naturwissenschaften*, 91(3):101–122, 2004.

[37] Fritz-Olaf Lehmann and Simon Pick. The aerodynamic benefit of wing–wing interaction depends on stroke trajectory in flapping insect wings. *Journal of experimental biology*, 210(8):1362–1377, 2007.

[38] Fritz-Olaf Lehmann, Sanjay P Sane, and Michael Dickinson. The aerodynamic effects of wing–wing interaction in flapping insect wings. *Journal of Experimental Biology*, 208(16): 3075–3092, 2005.

[39] J Gordon Leishman. *Principles of Helicopter Aerodynamics with CD Extra*. Cambridge university press, 2006.

[40] David Lentink and Michael H Dickinson. Biofluiddynamic scaling of flapping, spinning and translating fins and wings. *Journal of Experimental Biology*, 212(16):2691–2704, 2009.

[41] David Lentink and Michael H Dickinson. Rotational accelerations stabilize leading edge vortices on revolving fly wings. *Journal of Experimental Biology*, 212(16):2705–2719, 2009.

[42] Lennart Ljung. Perspectives on system identification. *Annual Reviews in Control*, 34(1):1–12, 2010.

[43] Guoyu Luo and Mao Sun. The effects of corrugation and wing planform on the aerodynamic force production of sweeping model insect wings. *Acta Mechanica Sinica*, 21(6):531–541, 2005.

[44] Field Manar, Albert Medina, and Anya R Jones. Tip vortex structure and aerodynamic loading on rotating wings in confined spaces. *Experiments in Fluids*, 55(9):1–18, 2014.

[45] David J Mee. Dynamic calibration of force balances for impulse hypersonic facilities. *Shock Waves*, 12(6):443–455, 2003.

[46] Laura A Miller and Charles S Peskin. Flexible clap and fling in tiny insect flight. *Journal of Experimental Biology*, 212(19):3076–3090, 2009.

[47] Thomas J Mueller. Aerodynamic measurements at low raynolds numbers for fixed wing micro-air vehicles. Technical report, DTIC Document, 2000.

[48] CA Ozen and Donald Rockwell. Flow structure on a rotating plate. *Experiments in fluids*, 52(1): 207–223, 2012.

[49] M Percin and BW Van Oudheusden. Three-dimensional flow structures and unsteady forces on pitching and surging revolving flat plates. *Experiments in Fluids*, 56(2):1–19, 2015.

[50] M Percin, Y Hu, B van Oudheusden, B Remes, and F Scarano. Wing flexibility effects in clap-and-fling. *International Journal of Micro Air Vehicles*, 3(4):217–228, 2011.

[51] M Percin, L Ziegler, and BW Van Oudheusden. Flow around a suddenly accelerated rotating plate at low reynolds number. In *17th International symposium on applications of laser techniques to fluid mechanics*, 2014.

[52] Mustafa Percin and Bas van Oudheusden. Flow visualization and force measurements on accelerated revolving flat plates at low reynolds numbers. In *45th AIAA Fluid Dynamics Conference*, page 3074, 2015.

[53] Sedkl M Riad. The deconvolution problem: An overview. *Proceedings of the IEEE*, 74(1):82–85, 1986.

[54] Matthew J Ringuette, Michele Milano, and Morteza Gharib. Role of the tip vortex in the force generation of low-aspect-ratio normal flat plates. *Journal of Fluid Mechanics*, 581:453–468, 2007.

[55] George G Roussas. *A course in mathematical statistics*. Academic Press, 1997.

[56] Sanjay P Sane. The aerodynamics of insect flight. *The journal of experimental Biology*, 206(23): 4191–4208, 2003.

[57] Sanjay P Sane and Michael H Dickinson. The control of flight force by a flapping wing: lift and drag production. *Journal of experimental biology*, 204(15):2607–2626, 2001.

[58] Sanjay P Sane and Michael H Dickinson. The aerodynamic effects of wing rotation and a revised quasi-steady model of flapping flight. *Journal of Experimental Biology*, 205(8):1087–1096, 2002.

[59] Wei Shyy, Patrick Trizila, Chang-kwon Kang, and Hikaru Aono. Can tip vortices enhance lift of a flapping wing? *AIAA journal*, 47(2):289–293, 2009.

[60] Wei Shyy, Hikaru Aono, Satish Kumar Chimakurthi, P Trizila, C-K Kang, Carlos ES Cesnik, and Hao Liu. Recent progress in flapping wing aerodynamics and aeroelasticity. *Progress in Aerospace Sciences*, 46(7):284–327, 2010.

[61] RB Srygley and ALR Thomas. Unconventional lift-generating mechanisms in free-flying butterflies. *Nature*, 420(6916):660–664, 2002.

[62] Siddarth Kolluru Venkata and Anya R Jones. Leading-edge vortex structure over multiple revolutions of a rotating wing. *Journal of Aircraft*, 50(4):1312–1316, 2013.

[63] R Vester, M Percin, and B van Oudheusden. Deconvolution kalman filtering for force measurements of revolving wings. *Measurement Science and Technology*, 27(9):095302, 2016.

[64] Z Jane Wang, James M Birch, and Michael H Dickinson. Unsteady forces and flows in low reynolds number hovering flight: two-dimensional computations vs robotic wing experiments. *Journal of Experimental Biology*, 207(3):449–460, 2004.

[65] JZ Wu, AD Vakili, and JM Wu. Review of the physics of enhancing vortex lift by unsteady excitation. *Progress in Aerospace Sciences*, 28(2):73–131, 1991.

[66] Huai-Te Yu. *Unsteady Aerodynamics of Pitching Flat Plate Wings*. PhD thesis, Air Force Research laboratory, 2014.

[67] Huai-Te Yu and LP Bernal. Effect of pivot point on aerodynamic force and vortical structure of pitching flat plate wings. *AIAA Paper*, 792:2013, 2013.

[68] JM Zanker. The wing beat of drosophila melanogaster. i. kinematics. *Philosophical Transactions of the Royal Society of London B: Biological Sciences*, 327(1238):1–18, 1990.

[69] Liang Zhao, Qingfeng Huang, Xinyan Deng, and Sanjay P Sane. Aerodynamic effects of flexibility in flapping wings. *Journal of the Royal Society Interface*, 7(44):485–497, 2010.